

Optical and Magnetic Resonance Properties of II-VI Quantum Dots

Dissertation

Huijuan Zhou

JUSTUS-LIEBIG-



UNIVERSITÄT
GIESSEN

Optical and Magnetic Resonance Properties of II-VI Quantum Dots

Am Fachbereich Physik
der Justus-Liebig-Universität Gießen
eingereichte Dissertation zur Erlangung des Grades eines
Doktors der Naturwissenschaften (Dr. rer. Nat.)

vorgelegt von

Huijuan Zhou

geb. in Hubei, China

Tag der Einreichung: 21.11.2002
Tag der mündlichen Prüfung: 17.12.2002

I. Physikalisches Institut der Justus-Liebig-Universität Gießen
2002

Contents

1	Introduction	1
2	Preparation of ZnO (:Mn) and CdS(:Mn) nanocrystals by chemical routes	3
2.1	Synthesis of ZnO and ZnO:Mn nanocrystals	4
2.1.1	<i>introduction</i>	4
2.1.2	<i>principle and control of the particle size</i>	5
2.1.3	<i>experiment</i>	6
2.2	Synthesis of CdS and CdS:Mn nanocrystals	7
2.2.1	<i>colloids</i>	8
2.2.2	<i>microemulsion</i>	9
2.2.3	<i>experiment</i>	11
2.3	Summary	12
3	Characterization methods	13
3.1	X-ray diffraction and optical measurements	13
3.1.1	<i>X-ray diffraction (broadening and Scherrer formula)</i>	13
3.1.2	<i>absorption measurement (quantum size effect)</i>	15
3.1.3	<i>photoluminescence and Raman spectroscopy</i>	16
3.2	Magnetic resonance measurements	16
3.2.1	<i>EPR technique</i>	16
3.2.2	<i>ENDOR technique</i>	18
3.2.3	<i>experiment processing</i>	20
3.3	Other measurements (TEM, EDX)	20
4	Structural and optical properties of ZnO quantum dots	21
4.1	Introduction	21
4.2	Structural properties	21
4.3	Emission properties	25
4.4	Core-shell model	29
4.4.1	<i>ZnO/Zn(OH)₂ core-shell model</i>	29
4.4.2	<i>thickness of the shell</i>	30
4.5	Correlation of the optical properties with the structure	31
4.5.1	<i>the appearance of strong UV emission</i>	31
4.5.2	<i>the appearance and change of the visible bands</i>	32
5	Defects and doping in ZnO quantum dots and electronic properties (I)	33
5.1	Introduction	33
5.2	EPR studies at 9.5 GHz	34
5.3	EPR studies at 95 GHz)	36

5.4	Results discussion	39
5.5	Chemical nature of the donors (ENDOR studies)	41
5.5.1	<i>cause of the shallow donors</i>	41
5.5.2	<i>cause of the deep donors</i>	43
6	Defects and doping in ZnO quantum dots and electronic properties (II)	45
6.1	Introduction	45
6.2	Structure of $Zn_{1-x}Mn_xO$ quantum dots	46
6.3	EPR results of Mn in $Zn_{1-x}Mn_xO$ quantum dots	48
6.3.1	<i>EPR spectra of Mn in $Zn_{1-x}Mn_xO$ quantum dots</i>	48
6.3.2	<i>origins of the EPR signals</i>	53
6.4	PL of $Zn_{1-x}Mn_xO$ quantum dots	57
7	Characterization of CdS:Mn quantum dots	58
7.1	Background knowledge	58
7.2	Optical absorption and luminescence properties	59
7.3	EPR spectra of $Cd_{1-x}Mn_xS$ quantum dots	63
7.4	Correlation of Mn local structures and their luminescence	65
7.4.1	<i>origin of signal S_I</i>	65
7.4.2	<i>origin of signal S_{II}</i>	65
7.4.3	<i>contributions of S_I and S_{II} to Mn luminescence</i>	66
7.4.4	<i>evolution of S_I and S_{II}</i>	67
7.5	A glance at the Mn emission life time	69
7.6	Summary	70
8	Summary	71
9	Deutsche Zusammenfassung	73
	Appendix	79
A.1	Fundamental Physical Constants	79
A.2	EPR/ENDOR frequency of some common elements	80
A.3	List of Figures	81
A.4	List of Tables	84
	Bibliography	85
	List of publications	91
	Curriculum Vitae	93
	Acknowledgement	94

Chapter 1 Introduction

Since the pioneering work of Efros [1] and Brus [2] devoted to the size-quantization effect in semiconductor nanoparticles, the research on nanostructures has been a flourishing field in chemistry, physics and material science. Nanoparticles, or nanocrystals having sizes comparable with the bulk exciton Bohr radius (usually less than 20 nm) are often called quantum dots (QDs) or Q-particles. In this size regime, the dots have optical and/or electronic properties which are dramatically different from the bulk.

Structure determines properties. For example, in traditional semiconductor technology, the properties of bulk semiconductors are precisely tailored for particular application through the introduction of impurities (doping) or external fields (charging). The unique properties of semiconductor quantum dots indicate different structures in them.

Compared with bulk semiconductors, the quantum dot counterparts have more complicated defect structures. *On one hand*, for instance, due to the large surface-to-volume ratio, more atoms will locate on the surface with dangling bonds, which usually act as nonradiative traps [3], and/or may incorporate foreign atoms to form a core-shell structure [4-6]. *On the other hand*, the conventional doping by introducing impurity atoms is difficult, especially in colloidal nanocrystals. The main challenge is to introduce the impurity in the core of the particle. Since the impurity is always only a few lattice constants from the surface of the nanocrystal, it may tend to diffuse to the surface or into the surrounding matrix due to the thermodynamic driving forces. In addition, the electronically active doping with extra carriers remains another challenge. To date, most efforts have focused on equivalent valence charge doping, for example, transition metals Mn [7, 8], Cu [9], or rare earth elements such as Tb [10, 11] or Eu [12] in II-VI chalcogenide semiconductor nanocrystals. Typically, these impurities do not affect the band-to-band absorption spectrum, but strongly modify the luminescence properties because they do not introduce extra carriers, but rather provide impurity centers that interact with the quantum confined electron hole pair. Since these impurities can be paramagnetic, they also introduce a localized spin into the nanocrystal, and form the so called diluted magnetic semiconductors (DMS).

In this work, we intend to explore the structure behind II-VI semiconductor quantum dots, illustrated mainly by ZnO and briefly by CdS as representative examples. The doping with Mn is also studied.

Bulk zinc oxide has received much attention due to its many technological applications, particularly in optical devices. The green photoluminescence behavior of ZnO has been of interest for building flat panel displays [13]. Other applications include gas sensors [14], solar cells [15], catalysts [16], substrates or buffer layers [17, 18] for growth of GaN. In the recent years, great interest in ZnO has been stimulated by the increasing demand in developing short-wavelength lasers and room temperature green-blue diode lasers from wide bandgap semiconductors. The unique features that ZnO has, both, a wide bandgap (3.37 eV) and a large exciton binding energy (~ 60 meV), makes it the most promising candidate for room temperature ultraviolet (UV) laser [19, 20]. Furthermore, theory predicts [21] that Mn-doped ZnO may form a ferromagnet with a very high Curie temperature (> 300 K). Questions, whether ZnO quantum dots maintain similar optical and/or electrical properties or behave differently, rise up as our starting points of the present work.

It has been widely reported that UV emission is rather weak in ZnO quantum dots, while a few groups claim the observation of strong UV transition [22, 23]. Investigation of the luminescence properties of ZnO quantum dots is the first task. Then follows the studies on the electrical properties. With high resolution magnetic resonance, the nature of the donors in “undoped” ZnO quantum dots is revealed. The considerable lack of study on Mn doping in ZnO in the past makes the investigation of Mn impurities in ZnO another worthwhile endeavor.

In the past years, the debate whether Mn doped II-VI chalcogenide semiconductor nanocrystals form new luminescence materials [8] or not [24, 25] has been in heated disputation. In the last section of this work, we also present our understanding of the luminescence properties of Mn in CdS quantum dots. Both the local structure of Mn impurities in CdS quantum dots and the luminescence are intensively studied.

A brief outline of the contents of this thesis is as follows. Chapter 2 begins with the introduction of the preparation of (Zn, Mn)O and (Cd, Mn)S quantum dots by chemical routes. The characterization methods used in the present work are described in chapter 3. In chapter 4 the structure and luminescence properties (especially UV emission) of undoped ZnO quantum dots are investigated. By applying magnetic resonance experiments, the donor defects and doping impurities (Mn) in ZnO quantum dots are studied in chapter 5 and chapter 6, respectively. Chapter 7 deals with the Mn local structure and luminescence properties in CdS quantum dots. In the final chapter 8 the main results of the work are summarized and discussed. Appendix I and II show the physics constants that are used in this work.

Chapter 2

Preparation of (Zn, Mn)O and (Cd, Mn)S quantum dots by chemical routes

Chemical synthesis permits the manipulation of matter at the molecular level. Due to its versatility in synthesizing nanoparticles and the feasibility in controlling the particle size, shape, and size distribution, many methods have been developed for the synthesis of II-VI and their ternary diluted magnetic semiconductor clusters [1-5]. They can be prepared in the form of dispersed colloids or trapped and stabilized within micelles, polymers, zeolites, or glasses. Among the II-VI semiconductor clusters, CdS colloids with size small enough ($< 50 \text{ \AA}$) to have discrete energy levels were first prepared in homogeneous solution [1]. To stabilize a colloid in the small cluster size regime, it is necessary to find an agent that can bind to the cluster surface and thereby prevent the uncontrolled growth into larger particles.

A common approach to such colloids is the use of a polymeric surfactants/stabilizer, e.g., sodium polyphosphate (hexametaphosphate). The polymer attaches to the surface of the growing clusters, usually electrostatically, and prevents their further growth.

A similar approach is the use of deliberately added capping agents to solutions of growing clusters. The agents, typically anionic, are added to a semiconductor precipitation reaction and intercept the growing clusters, preventing further growth by covalently binding to the cluster surface. Thiolates are the most commonly used capping agents and this method also forms the basis of the synthesis of monodispersed clusters [6]. The use of micelle (also called microemulsion, reverse/inverted micelle/emulsion) is conceptually similar to the colloidal and capping approaches just described. In this case, however, a small region of physical space is defined by a micelle and the semiconductor is precipitated within this defined region. In contrast to the colloidal approach, the micellar reagent acts as a physical boundary rather than a surface capping agent. Both methods are the most commonly methods for synthesis of II-VI chalcogenide clusters.

The preparation of ZnO and CdS clusters in the present work, though different from each other, is no escape of the forehead described approaches. Because of the extensive reports and already mature preparation methods, we will, in this chapter, stress our improvements on the former work, while describe briefly the principles and the experiment procedures. The generation of ZnO quantum dots in alcohol solvents is illustrated in section 2.1 and CdS:Mn clusters in microemulsion in section 2.2.

However, there exist problems with the chemical synthesis methods. In most case, clusters prepared by these methods have poorly defined exterior surfaces and a relatively broad size distribution ($\sim 10\text{-}20\%$). Many of the chemical synthesis routes, while designed to produce the desired semiconductor clusters, often form unexpected by-products. Still another problem is that undesirable agglomeration at any stage of the synthesis process can change the properties.

2.1 Synthesis of ZnO and ZnO:Mn nanoparticles

2.1.1 Introduction

Since the first report on the preparation of ZnO colloids in alcoholic solution by Koch in 1985 [7], many techniques have been developed to prepare ZnO colloids, for example, controlled double-jet precipitation [8], sol-gel synthesis [9], and chemical precipitation [10]. Other chemical routes involve preparation of ZnO nanoparticles by an electrochemical bath route in constant current mode [11], and in porous media such as porous silica [12] and aluminum [13], by making use of the confinement of the pore size. In addition, physical routes are also used to synthesize ZnO nanocrystal thin films by epitaxy and deposition methods, such as microwave plasma-enhanced molecular beam epitaxy (MBE) [14], laser MBE [15], vapor phase deposition [16], radical beam epitaxy [17], and pulsed laser deposition [18].

Among the above methods, the first one benefits from the simple experimental conditions (e.g. laboratory ambient, and simple chemical reactions in flasks), compared with the physical routes, and smaller sizes ($2 \sim 10$ nm) in contrast to the other chemical routes. According to Koch [7], ZnO colloid with low concentration (~ 0.2 m·mol/L) in alcohol solvent can be obtained following the base hydrolysis of a dilute solution of zinc acetate using LiOH. It is indeed the most popular method for preparing ZnO nanoparticles, widely used in the literature. Based on this method, ZnO nanoparticles in different forms (e.g., concentrated colloids, crystals, powders, or thin films) have been synthesized [19, 20]. In this work we also use this method to prepare ZnO nanocrystal samples, however with some changes. For example, we use different zinc salt source, NaOH instead of LiOH, and most important, an annealing treatment. The reason for the changes can be seen below in section 2.2.3.

2.1.2 Principle and control of the particle size

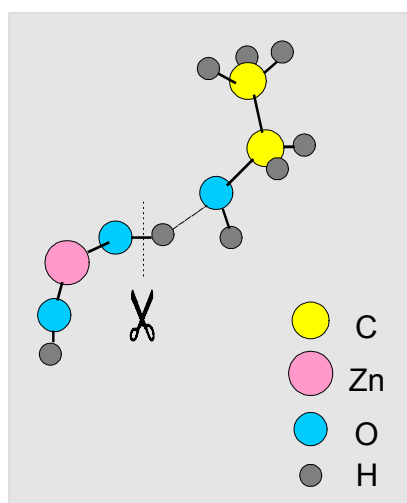


Figure 2.1 Scheme of the formation of ZnO clusters in alcoholic solution.

In general, the preparation of ZnO nanoparticles, by the reaction of Zn^{2+} with OH^- in alcoholic solution, is based on the dehydration property of alcohol [21]. Figure 2.1 shows the model of ethanol interacting with $\text{Zn}(\text{OH})_2$. Here each terminal oxygen of the ZnO cluster is replaced by a hydroxyl group. The coordination number is set to the practical numbers realized in the oxide crystals. The hydrogen of the hydroxyl group of $\text{Zn}(\text{OH})_2$ is deprived by ethanol, thus ZnO particle rather than $\text{Zn}(\text{OH})_2$ forms. This reaction produces a transparent colloid where the ZnO particle size increases slowly on standing.

The particle size r , is of course related to the concentration of Zn^{2+} and OH^- c , the aging temperature T , and the aging time t , and can be expressed as a function of the three as

$$r = r(c, T, t). \quad (2.1)$$

To study the growth kinetics of ZnO nanoparticles from colloidal suspensions, it is necessary to determine the particle size. The growth process is extensively investigated in Ref. [22], and is found to follow Ostwald ripening kinetics [23], i.e. for a system of highly dispersed particles the growth is controlled by diffusion. For species present at a solid/liquid interface, the local equilibrium concentration of the species in the liquid phase is dependent on the local curvature of the solid phase. Differences in the local equilibrium concentrations, due to variations in curvature, set up concentration gradients that lead to transport of species from the regions of high concentration (big curvature) to regions of low concentration (small

curvature). The capillary forces provide the driving force for the growth of larger particles at the expense of smaller ones. According to the mathematical approach of Lifshitz-Slyozov-Wagner (LSW) theory [24, 25] the average particle size \bar{r} is given by

$$\bar{r}^3 - r_0^3 = Kt \quad (2.2)$$

where r_0 is the initial particle radius. The rate constant K is given by

$$K = \frac{8\gamma DV_m^2 C_\infty}{9RT} \approx \frac{8\gamma DV_m^2 C_r}{9RT} \quad (2.3)$$

where γ is the interfacial energy, D the diffusion coefficient, V_m molar volume of the solid phase, R gas constant, and C_∞ is equilibrium concentration at a flat surface, approximately equal to C_r , the concentration of the species in liquid phase in equilibrium with a spherical solid particle with radius r . Both D and C_r are proportional to temperature. Therefore the particles grow with time and temperature.

In principle, to obtain small ZnO particles, one has to try to avoid the aging effect, which is unfortunately difficult in the colloid since the particles grow on standing. Though interesting for basic research on the growth kinetic, the instantly changing size and the similar surface structures of ZnO clusters in colloid system are not of too much practical application. We are more interested in changing the structure (including particle size and surface property) in a positive way rather than the “wait-and-see” method in the colloid. Therefore we introduce a post-synthesis annealing treatment in this work.

2.2.3 Experiment

In our experiments the preparation of the ZnO colloidal suspensions basically follows the method of Koch [7] and Spanhel [19] with the following variations. To exclude the possible surface effect from acetate (CH_3COO^-) groups (as sometimes claimed [26]), we use highly soluble $\text{Zn}(\text{NO}_3)_2$ instead of ZnAc (zinc acetate) so that to eliminate the effect from the reactant itself. NaOH is used instead of LiOH though the latter is better for obtaining a stable colloid, which is however not our aim of the work. For simple control of both the particle size and the surface conditions, annealing of the as-prepared samples is introduced. The advantage of the heat treatment will be seen clearly later in chapter 4.

The synthesis is as follows. 5m·mol $\text{Zn}(\text{NO}_3)_2$ (Aldrich, reagent grade) is dissolved in 250 ml absolute methanol (Aldrich, spectrophotometric grade), and then 10m·mol sodium

hexametaphosphate (Aldrich, reagent grade) is added. After vigorous magnetic stirring and ultrasonic bath, a semi-transparent solution is obtained, leaving most of the undissolved sodium hexametaphosphate at the bottom. The solution is then separated from the undissolved residue. 10m·mol NaOH (Aldrich, reagent grade) powder is added to another 250ml methanol, and placed into ultrasonic bath to destroy the weakly soluble powder. Normally this process takes one day before the NaOH is completely dissolved. Slowly mixing the two solutions gives first a transparent solution. With the addition of Zn^{2+} , the solution gradually becomes opalescent. By centrifugation, a white solid is separated from the solution. Washing the solid with the mixture of 70% methanol and 30% distilled water and then air drying leads to a white powder. The samples used in this work are obtained by annealing the powder in air at different temperatures from 150-500°C for 30 min. Absolute 2-propanol (Aldrich, spectrophotometric grade) is also used as an alternative alcohol source.

In comparison, highly purified bulk ZnO powder (Aldrich, reagent grade), $Zn(OH)_2$, and $Zn(OH)_2$ (150°C), i.e., $Zn(OH)_2$ sample annealed in air at 150°C for 30 min, are prepared as reference samples. $Zn(OH)_2$ precipitation is obtained by mixing $Zn(NO_3)_2$ and NaOH aqueous solution. It is known from textbook chemistry that $Zn(OH)_2$ prepared in this way is amorphous.

Doping is achieved by the addition of Mn^{2+} to the reaction. By changing amount of manganese salt ($Mn(NO_3)_2$, in our work) $Zn_{1-x}Mn_xO$ nanoparticles with different doping concentration x are realized. The color of the samples changes from brownish to dark brown when x increases. For comparison, bulk $Zn_{1-x}Mn_xO$ polycrystals are also prepared by admixing of ZnO and MnO powder and sintering in air at 900°C for 2h.

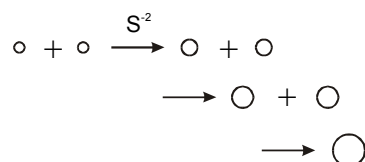
2.2 Synthesis of CdS and CdS:Mn nanoparticles

Compared with the preparation of ZnO, the reports on the synthesis of CdS nanoparticles are even overwhelming [1-4, 27-29]. The virtue of the syntheses lies in easier and better size control and dispersion stability by rational control of the chemical reaction process. In this section we will only introduce the two most commonly used method, briefly on surface capping in colloids, and mainly on microemulsion, which is the method that we use in this work. Preparation of Mn doped CdS nanoparticles is essentially the same as that of the undoped, and differs only in the addition of Mn salts to the reaction.

2.2.1 Colloids

This approach can be thought of as mimicking an organic polymerization reaction (initiation, propagation, and termination phases) and is graphically depicted for CdS clusters in figure 2.2. In this analogy, mixing the cadmium and sulfide ions initiates the polymerization. The growth of the CdS clusters is viewed as a propagation step and is sustained by the presence of additional cadmium and sulfide ions. The growth of the clusters can be terminated by providing a capping agent such as thiophenolate ions which intercept the growing clusters by binding to the cluster surface and competing in the reactions with Cd^{2+} [30]. The average size can then be conveniently controlled by simply adjusting the sulfide to thiophenolate ratio on the solution, just as the average molecular weight of a polymer is controlled by adjusting the monomer to terminator (chain capper) ratio. It is found that thiophenolate capped CdS clusters act somewhat like living polymers, i.e. they will continue to grow if fed more sulfide ions [31]. This living polymer property was used advantageously to produce monodisperse clusters. However, due to high poison of thiol, we don't recommend this method, rather prefer the following microemulsion method.

Chain propagation:



Chain termination:

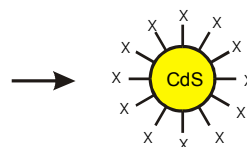


Figure 2.2 Schematic diagram for the synthesis of thiophenolate capped CdS clusters after Ref. [31] (X represents thiophenolate ion). The synthetic strategy mimics organic polymerization reactions. The size of the circle represents the size of the CdS clusters. The growth of the CdS clusters is analogous to the growth of a polymer chain as long as the surfaces are not covered by the terminating agent, X.

2.2.2 Microemulsion

2.2.2.1 Water-in-oil AOT microemulsion

Reverse emulsion droplets have been used essentially as chemical microreactors to produce nano-sized inorganic and polymer particles [32, 33]. The unique environment created in the small water pools of swollen reverse micelles allows for increase chemical reactivity. The increase in surface area with the decrease in size of the droplets also can significantly increase reactivity by allowing greater contact of immiscible reactants. Bis (2-ethylhexyl) sodium sulfosuccinate (Aerosol-OT, AOT) solubilizes a large quantity of water in various hydrophobic organic solvents and forms stable reversed microemulsions (water in oil) without the complication introduced by an additional cosurfactant. Such a cosurfactant (usually alcohol) is required by many other reverse microemulsion systems. This simplification makes the alkane/water/AOT system a model for studying reverse microemulsions. The water drops are encapsulated by the AOT surfactant so that virtually all of the AOT is located at the interface shell, as shown by the scheme in the inset of figure 2.3. It was found at low water content, the water is strongly bound to the AOT surfactant polar head groups and exhibits unique characteristics different from bulk water [34], while at higher water ratios, free water is predominant in the swollen reverse micellular solutions.

2.2.2.2 Control of particle size

The size of the water droplets can be conveniently altered by adjusting the molar ratios of water to surfactant designated as w ($[\text{H}_2\text{O}]/[\text{AOT}]$). Figure 2.3 shows the change of mean droplet size on w , measured with different methods. Apparently it can be seen that mean size increases with w (when < 60) almost in a linear fashion, though the sizes vary for different methods. Water pools with diameters ranging from 2 nm up to 20 nm can be formed. At approximately $w = 60$, the system undergoes a transition from a transparent microemulsion into an unstable turbid macroemulsion. This macroemulsion separates on standing into a clear upper phase and a turbid lower phase.

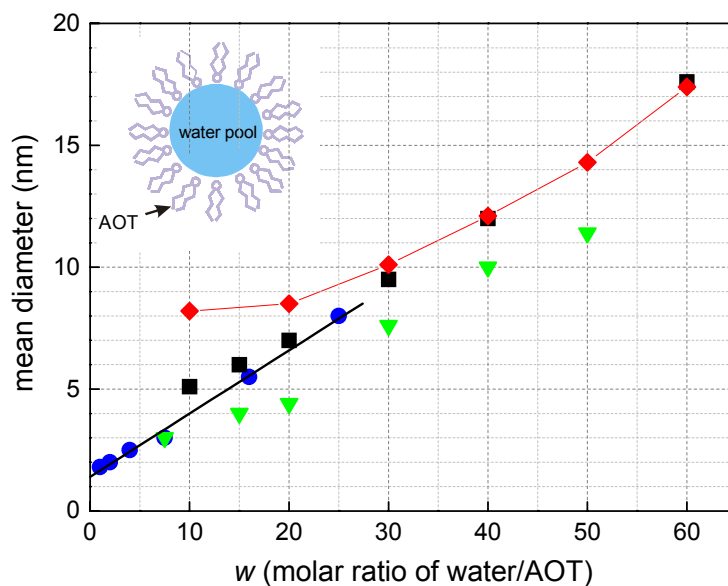


Figure 2.3 Comparison of mean droplet size of heptane/water/AOT microemulsion, measured by different groups: circle from Wines [35], triangle from Ref. [36], square from Ref. [37], and diamond from Ref. [38]. The inset shows the scheme of the forming of water pool encapsulated by the AOT surfactant in the microemulsion.

The dependence of the size measured by Wines [35] on w can be approximated by the following equation

$$d = 0.259w + 1.4 \quad (w < 30) \quad (2.4)$$

The increase in droplet size and phase boundary can be achieved by raising the temperature up to a critical temperature of 55°C [34], beyond which the microemulsion is no longer stable.

2.2.2.3 Effect of the addition of salts

The nature and structure of heptane/water/AOT microemulsion can be significantly influenced by the addition of salts in different ways. It has been observed by Ikushima [34], that lithium chloride extends the range of w in contrast with the narrowing of w to less than 12 by cesium iodide, while little affected by guanidine hydrochloride. This is maybe due to the change of the structured water molecules bound to head groups by the acidity/alkalinity of the added salts: probably enhanced by acidity, but released by basicity. Similar phenomenon is also observed in this work when adding cadmium nitrate and sodium sulfide to the microemulsion. Weak alkalic sodium sulfide narrows the range of R to less than 15 and

causes the one-phase emulsion system to become a two-phase system, while the system was rather stable when relatively acid neutral cadmium nitrate is added.

2.2.3 Experiment

The reverse microemulsion are prepared by first making a 0.1 molar AOT (Aldrich, reagent grade) in heptane (Aldrich, spectrophotometric grade) solution. Then distilled water is added in droplets with graduated Teflon syringe and shaken in rubber capped glass cone flasks and then bathed with ultrasonic for several minutes. The shaking action and the ultrasonic bath are required to overcome an energy barrier to distribute the water into the nanosized droplets, as it could not be achieved using a magnetic stirrer. A transparent solution from the heptane/water/AOT ternary system is finally obtained. In all cases, the reported w values are based on the added water and are not corrected for any residual water that may have been in the dried AOT or heptane solvent. Former analysis of the AOT-heptane solutions before the addition of water showed a w value of 0.4 [35]. This amount can be considered to be negligible. The process used for the synthesis of the CdS:Mn nanoparticles is schematically described in Figure 2.4. In a first step, the particles are synthesized by controlled precipitation in reverse micelles. Then pyridine is added to the microemulsion allowing the separation of the particles as a powder.

The controlled precipitation of the CdS:Mn nanoparticles is achieved in the reverse micells. In all experiments the water concentration is taken equal to $2.5 \text{ mol}\cdot\text{L}^{-1}$, where the concentration of AOT is varied for different w value up to 10 due to the limitation by the addition of sodium sulfide. The initial concentrations of Cd^{2+} , and S^{2-} dissolved in the water pools are taken equal to 0.2, and $0.4 \text{ mol}\cdot\text{L}^{-1}$, respectively. The Mn^{2+} concentration is changed so that different doping could be achieved.

A first solution is prepared, containing the cadmium nitrate and manganese nitrate dissolved in water droplets. This solution is then slowly added to the same volume of a similar solution containing sodium sulfide. After a few seconds, a transparent yellow color appears within the solution, attesting for the formation of the particles.

The addition of pyridine in dropwise to the solution leads to oil-like precipitation, for the pyridine molecule complexes the surface of the nanoparticles and therefore no more stable in the reverse micelles. After centrifugation the yellow precipitation at the bottom is separated from the colorless upper part solution. The deposits is then washed sufficiently with plenty of

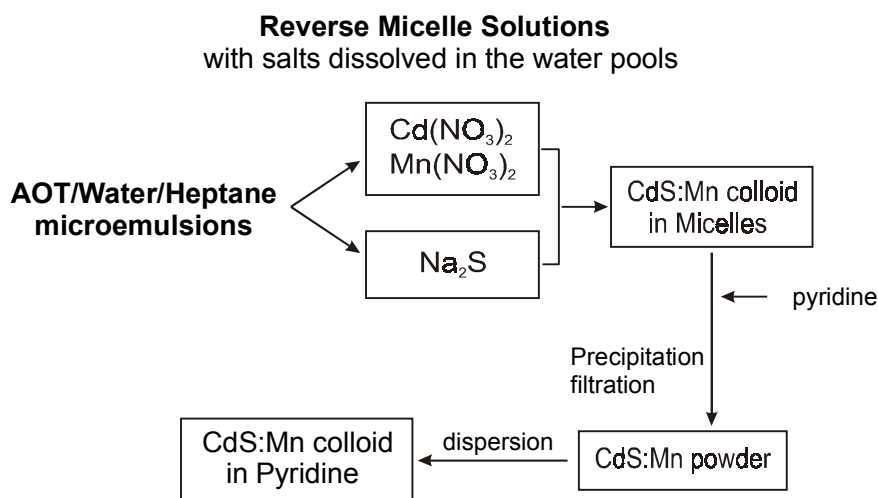


Figure 2.4 Schematic representation of the process used for the preparation of CdS:Mn nanocrystals.

petroleum ether to remove residual AOT. The nanocrystals can be finally dispersed in pure pyridine again, giving a transparent yellow-orange solution, or dried in air to obtain free standing nanocrystal powder. Using the sol-gel chemistry, a final material as bulk disks a few centimeters in diameter or as thin films deposited on various substrates have been obtained [39]. During the experiment we noticed that the production of the nanocrystals from the microemulsion is to large extent correlated with the amount of the added pyridine. When the amount of pyridine is not enough, the surface passivation is incomplete and inadequate, leaving some particles still soluble in the micells. The insufficient passivation also leads to poor solubility of the particles in pyridine again. In contract, when pyridine is added too much, the deposit is redissolved in pyridine before it could be separated from the solution, and gives a turbid mixture. In both cases no obvious precipitation is obtained. It is found the addition of 3~4 ml pyridine gives the optimum production.

2.3 Summary

In this chapter the preparation of (Zn, Mn)O and (Cd, Mn)S quantum dots is reported. ZnO and ZnO:Mn clusters can be generated in alcohol solution, with surface and the size changed by annealing process. CdS and CdS:Mn quantum dots can be synthesized in heptane/water/AOT microemulsion. By changing the water/AOT ratio, the size of the dots can be accurately controlled.

Chapter 3 Characterization methods

In this chapter we review the methods and techniques that are used in the present work to characterize the prepared ZnO(:Mn) and CdS(:Mn) quantum dots.

X-ray diffraction (XRD), as one of the most useful and convenient tool, is used for the structure characterization, e.g. the identification of phases and particle size evaluation. Optical absorption spectra are measured for monitoring the bandgap enlargement due to the quantum size effect, and for determining the particle size as well. For a direct measurement of the particle size, transmission electron microscopy (TEM) is used. To investigate the luminescence properties, the photoluminescence spectra of the quantum dots are measured. With Raman scattering detailed information on the lattice vibrations is obtained. The elemental composition of the dots can be determined by energy disperse spectroscopy (EDX). Magnetic resonance studies, e.g. electron paramagnetic resonance (EPR) and electron nuclear double resonance (ENDOR), offer unique advantages to explore the nature of the relevant impurities or dopants, which are normally the origin behind the characteristic physical properties, but could not be provided e.g., by the XRD and optical measurements.

In the following sections, we will neglect the conventional theory of XRD and the optical processes, but briefly introduce the quantum-size-related phenomena, for example, size broadening in diffraction and the quantum size effect. As special points of interest, we will emphasize the principles and techniques of EPR and ENDOR, which are not so commonly used as XRD and the optical measurements for the study of nanocrystals.

3.1 X-ray diffraction and optical measurements

3.1.1 X-ray diffraction (broadening and Scherrer formula)

When the x-ray beams with wavelength λ impinge on a crystal, the diffraction beams will be found in the condition that satisfies the Bragg law [1]

$$2d_{hkl} \sin \theta = n\lambda \quad (3.1)$$

where d_{hkl} is the spacing of the planes (hkl), 2θ the diffraction angle, and n is integer. reflections from parallel planes of atoms in the crystal will occur. For an unpolarized primary beam of intensity I_0 , the diffraction intensity I_p from a small single crystal is given by

$$I_p = I_e F^2 \frac{\sin^2[(\pi/\lambda)(\vec{s} - \vec{s}_0) \cdot N_1 \vec{a}_1]}{\sin^2[(\pi/\lambda)(\vec{s} - \vec{s}_0) \cdot \vec{a}_1]} \times \frac{\sin^2[(\pi/\lambda)(\vec{s} - \vec{s}_0) \cdot N_2 \vec{a}_2]}{\sin^2[(\pi/\lambda)(\vec{s} - \vec{s}_0) \cdot \vec{a}_2]} \times \frac{\sin^2[(\pi/\lambda)(\vec{s} - \vec{s}_0) \cdot N_3 \vec{a}_3]}{\sin^2[(\pi/\lambda)(\vec{s} - \vec{s}_0) \cdot \vec{a}_3]} \quad (3.2)$$

where

$$I_e = I_0 \frac{e^4}{m^2 c^4 R^2} \left(\frac{1 + \cos^2 2\theta}{2} \right), \text{ related to scattering factor } \frac{e^4}{m^2 c^4 R^2} \text{ and polarization factor } \cos^2 2\theta, \text{ structure factor } F = \sum_n f_n \exp(2\pi i / \lambda)(\vec{s} - \vec{s}_0) \cdot \vec{r}_n, \text{ and } F^2 = FF^*.$$

N_1, N_2, N_3 are the numbers of unit cells along the $\vec{a}_1, \vec{a}_2, \vec{a}_3$ directions, and \vec{s}_0 and \vec{s} are the unit vector of the primary and reflection beam respectively.

In general, the N_1, N_2, N_3 are such large numbers, that each of the three quotients differ from zero only if the Laue equations

$$\begin{aligned} (\vec{s} - \vec{s}_0) \cdot \vec{a}_1 &= h\lambda \\ (\vec{s} - \vec{s}_0) \cdot \vec{a}_2 &= k\lambda \\ (\vec{s} - \vec{s}_0) \cdot \vec{a}_3 &= l\lambda \end{aligned} \quad (3.3)$$

are closely satisfied, and hence the powder pattern reflections are narrow. For very small crystals where N_1, N_2, N_3 are small, the three quotients broaden, and the smaller the crystals the broader the powder pattern reflections. The peak width can be expressed in terms of the crystalline size, and hence a measurement of the peak width gives a simple method for determining crystal size in the size range up to about 1000 Å.

The first treatment of particle size broadening was done by Scherrer. By making some simplifications, e.g., taking a powder sample of a small cubic crystal, and assuming they are free from strains and faulting, so that the peak broadening is due only to the small size, the following Scherrer equation [1]

$$2R = \frac{0.89\lambda}{\beta \cos \theta} \quad (3.4)$$

was obtained, where $2R$ is the particle diameter, 2θ is the diffraction angle, and β is the half width of the widened diffraction line. From the width of the diffraction peak using the Scherrer equation, one can calculate the average cluster size.

The validity of Scherrer equation has been examined by using direct computer simulation of the Bragg diffraction [2]. The presence of size inhomogeneities and point defects does not

significantly affect the accuracy of the size determination from the width of the x-ray diffraction peaks.

Our X-ray diffraction spectra were measured on a Siemens D-5000 diffractometer with Cu k_α ($\lambda = 1.5406 \text{ \AA}$) radiation. All samples were analyzed at 40 kV and 30 mA in the range of $30^\circ \leq 2\theta \leq 74^\circ$. The crystal structure was analyzed by a θ - 2θ scan with a resolution of 0.005° at a speed $1^\circ/\text{min}$.

3.1.2 Absorption measurement (quantum size effect)

For semiconductor clusters, the increase of the bandgap with decreasing cluster size, known as quantum size effect, is well established in literature [3]. The physics behind the quantum size effect is the particle-in-box quantum model [4] due to the confinement of charge carriers (the electron and the hole) in the restricted volume of small particles. When the particle size is comparable to the Bohr radius of the exciton

$$a_B = \frac{\hbar^2 \varepsilon}{e^2} \left[\frac{1}{m_e} + \frac{1}{m_h} \right], \quad (3.5)$$

the electrons and the holes have to be treated in the quantum mechanical way, which leads to the quantum size effect. Here ε is the relative dielectric constant, and m_e and m_h are the effective masses of the electron and hole, respectively.

By assuming the energy band to be parabolic near the bandgap (i.e., the effective mass approximation [5,6]), the size dependent shift in the exciton energy of a small cluster (cluster radius $R \sim a_B$) can be approximated by

$$\Delta E = E - E_g^{bulk} = \frac{\hbar^2 \pi^2}{2R^2} \left[\frac{1}{m_e} + \frac{1}{m_h} \right] - \frac{1.786e^2}{\varepsilon R} - \frac{0.248e^4}{2\varepsilon^2 \hbar^2} \left(\frac{1}{m_e} + \frac{1}{m_h} \right) \quad (3.6)$$

where E_g^{bulk} is the bulk bandgap. The first term is the particle-in-box quantum localization kinetic energy, the second is the Coulomb interaction between the electrons and the holes, and third is due to the spatial correlation effect, which is usually very small and can be neglected. Experimentally, the absorption edge shifts to higher energies. According to the effective mass model, the average particle size can be determined from the shift of the bandgap. However, one should be cautious when using this method to calculate the particle size since the model will be breakdown when the clusters are so small that the eigenvalues of the lowest excited states are located in a region of the energy band that is no longer parabolic [4]. Thus the

effective mass approximation will give particle sizes somewhat larger than those obtained by direct measurement such as TEM (or HRTEM) or x-ray line broadening. We should keep this in mind, and combine different methods to characterize particle sizes.

Absorption measurements were conducted at room temperature on photospectrometer in the range from 200 nm to 800 nm. The ZnO powder samples were dispersed in water with the help of an ultrasonic treatment for 3 minutes and then put into quartz cell tubes for measurements. CdS and CdMnS samples were measured in liquid form.

3.1.3 Photoluminescence and Raman spectroscopy

Photoluminescence was performed using a He-Cd laser with a wavelength of 325 nm as the excitation source. During the process, the laser light was first filtered with a 325 nm interference filter in order to eliminate the other laser line (425 nm). Then the light was modulated by a mechanical chopper before it entered the cryostat and hit the sample. The light emitted from the sample was dispersed by a monochromator and detected with a UV sensitive photomultiplier. The detected signal was first preamplified and then selectively amplified in a Lock-In, and finally processed by a computer using a D/A converter. Additionally, a 345 nm filter was used to eliminate the second harmonic of the laser line at 650 nm. For photoluminescence excitation (PLE) measurement, the first monochromator is coupled to the xenon lamp. The chopper was used to eliminate the strong excitation power of the laser, and at the same time it offers a possibility to estimate the decay time of the luminescence as we will see later in chapter 7.

The spatially resolved Raman experiments were carried out using a Dilor XY800 triple-grating spectrometer with a charge-coupled device (CCD) detector. The sample was excited parallel to the substrate surface using the 488 nm, 514.5 nm, and 568 nm lines of Ar⁺/ Kr⁺ mixed-gas laser. By passing the laser through a microscope objective the laser beam was focused on a point spot with a diameter of about 1 μ m. The scattered light was detected in backscattering geometry which corresponds to an $x(\cdot)\bar{x}$ configuration.

3.2 Magnetic resonance measurements

3.2.1 EPR technique

EPR measurements (also often referred to as electron spin resonance (ESR)) provide one of the few techniques capable of exploring the environment of a paramagnetic center in a solid.

The technique is specially useful for probing the symmetry and the local “electronic” structure (spin density) of the paramagnetic metal ions.

For a free paramagnetic electron the magnetic moment $\boldsymbol{\mu}$ is proportional to the angular moment $\hbar J$ (\hbar the Planck constant), and is expressed by

$$\boldsymbol{\mu} = -\gamma\hbar\mathbf{J} = -g\beta\mathbf{J}, \quad (3.7)$$

where γ is called the magnetogyric ratio of the electron, β the Bohr magneton, and g the Lande g factor. β is equal to $e\hbar/2mc$ with e , and m are respectively the charge, and mass of the electron, and c the velocity of light. For an electron spin $g = 2.0023$, usually taken as 2.00.

In the presence of steady magnetic field H , there is an interaction between the field and the electron magnetic moment, which may be represented in term of the Hamiltonian

$$\mathcal{H} = -\boldsymbol{\mu} \cdot \mathbf{H}. \quad (3.8)$$

The angular moment $\hbar J$ is restricted to those angles at which its components m_J in the magnetic field direction \mathbf{H} are given by the $2J+1$ values, $-J, -J+1 \dots J-1, J$. Thus the generated energy levels at zero field is then degenerated by the field with

$$E = m_J g \beta H. \quad (3.9)$$

This is the so-called Zeeman splitting. The splitting energy between two adjacent levels is

$$\Delta E = g \beta H. \quad (3.10)$$

For electrons in a field of 1 Tesla, the magnetic energy splitting $g\beta H$ is 0.116 meV, comparable with the energy of a microwave. Therefore application of an oscillating microwave field perpendicular to H will induce transitions between adjacent levels ($\Delta m_J = \pm 1$) when the frequency satisfies the resonance condition

$$h\nu = g\beta H. \quad (3.11)$$

The energy splitting for electrons with $S = 1/2$ and no orbit spin is illustrated as an example in Figure 3.1. In subsequent discussions we shall denote the state $m_S = +\frac{1}{2}$ by the symbol $|\alpha\rangle$ and $m_S = -\frac{1}{2}$ by $|\beta\rangle$.

Similarly, when the nucleus possess spin, the nuclear magnetic resonance (NMR) will also take place though the nuclear Zeeman energy splitting $g_N \beta_N H$ is only about one thousandth of that of the electron Zeeman splitting, and interactions with nuclear spins can then readily occur. In addition, a paramagnetic center in a solid will see the crystalline electric field

produced by the charge on the diamagnetic neighbors in the lattice. Such effects are to be included for a complete calculation of the splitting of the levels of an electron.

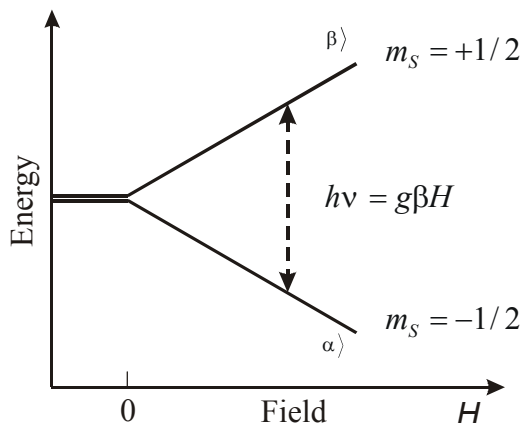


Figure 3.1 Splitting of electron levels ($S = \frac{1}{2}$) in a magnetic field.

To summarize, the complete effective Hamiltonian, usually referred as spin Hamiltonian, is

$$\mathcal{H} = \underbrace{g\beta H \cdot S - g_N \beta_N H \cdot I}_{\text{Zeeman-splitting}} + \underbrace{S \cdot D \cdot S}_{\text{Fine-structure}} + \underbrace{I \cdot Q \cdot I}_{\text{quadrupole}} + \underbrace{AI \cdot S + \sum_n I_n \cdot A_n \cdot S_n}_{\text{Hyperfine-coupling}}. \quad (3.12)$$

The terms in the first bracket are the Zeeman interaction between the electrons and the applied magnetic field, and the Zeeman interaction between the nucleus and the magnetic field, respectively. The third term represents the interaction with the crystalline electric field with the fine-structure parameter D . The fourth term describes the quadrupole interaction of the nuclear spin. The final hyperfine coupling terms represent the magnetic interaction between the paramagnetic electrons and their own nucleus of spin I , i.e. the hyperfine splitting (HFS), and the magnetic interaction between the electrons and nuclear moments I_n located at other lattice sites, the so-called super-hyperfine splitting (SHFS) or ligand hyperfine interaction.

3.2.2 ENDOR technique

Electron nuclear double resonance (ENDOR) experiment provides a powerful method for measuring small hyperfine interactions that are not resolved in EPR spectra. To do this it is necessary to saturate the electron resonance and sweep the frequency of the radiofrequency

(RF) pulses slowly through a suitable range and monitor the intensity of the electron resonance. When the nuclear Zeeman frequency fits

$$h\nu = \left| g_N \beta_N H \pm \frac{A}{2} \right| \quad (3.13)$$

the electron resonance signal rises sharply and slowly falls back again to its previous low value. To illustrate the principle of the experiment we take a radical where the unpaired electron ($S=\frac{1}{2}$, $m_s= \pm \frac{1}{2}$) has isotropic hyperfine interaction with a single proton ($I=\frac{1}{2}$, $M_I= \pm \frac{1}{2}$), see figure 3.2. Here the fine structure and the quadruple interaction are neglected. We shall further assume that the electron and nuclear spins relax through completely independent processes, so that saturation of the electron resonance does not alter the nuclear spin populations. Saturation of the hyperfine line which corresponds to the transition $\alpha_e \alpha_N \rightarrow \beta_e \alpha_N$ makes the populations $N_{\alpha\alpha}$ and $N_{\beta\alpha}$ equal. At the same time the electron resonance signal becomes very weak and broad because of saturation. Meanwhile the populations of the states $\alpha_e \beta_N$ and $\beta_e \beta_N$ have not changed. If we suddenly apply a strong RF pulse at the frequency

$$h\nu = \frac{A}{2} - g_N \beta_N H \quad (3.14)$$

which corresponds to the transition $\alpha_e \beta_N \rightarrow \alpha_e \alpha_N$ and

$$h\nu = \frac{A}{2} + g_N \beta_N H \quad (3.15)$$

which corresponds to the transition $\beta_e \alpha_N \rightarrow \beta_e \beta_N$, the immediate effect is that the states $\alpha_e \alpha_N$ and $\beta_e \alpha_N$ no longer have equal populations; the electron resonance suddenly ceases to be saturated and absorption rises simultaneously until a state of saturation is restored. Therefore each nucleus will give rise to two ENDOR transitions symmetrically placed around their nuclear Zeeman frequency $g_N \beta_N H_0 / h$ (where the quadrupole interaction is neglected).

The reason why the ENDOR spectrum is so much better resolved is that there is only one line for each distinct group of nuclei with a particular hyperfine splitting constant, while the EPR hyperfine structure has approximately 2^n lines for n nuclei, and shows a broad structureless line due to very badly overlap. The EPR/ENDOR frequency table of elements that present in this work and some other common elements is shown in Appendix II.

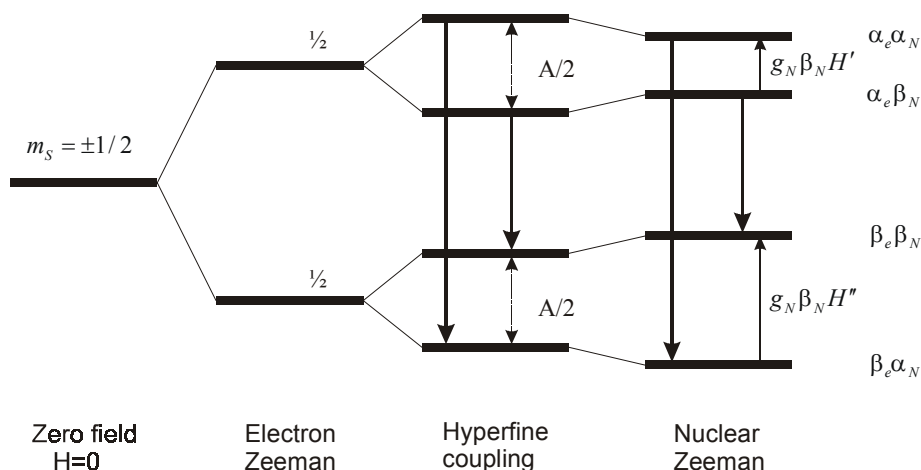


Figure 3.2 Splitting of energy levels of a radical with $m_s = \pm \frac{1}{2}$ and $M_I = \pm \frac{1}{2}$. The EPR and ENDOR transitions are indicated. Here the fine structure and the quadrupole interaction are neglected.

3.2.3 Experiment processing

The conventional EPR experiments were performed at X band microwave frequency (9.5 GHz) in a Bruker ESP300 spectrometer with microwave power of 0.02-200mW, at the modulation width 0.1 mT, and the modulation frequency 100 KHz. Temperature studies from 4.2 K to 300 K were carried out using an Oxford gas-flow cryostat. The applied magnetic field was calibrated by proton nuclear magnetic resonance field meter. High resolution EPR and ENDOR measurements were performed at 1.5 K at a pulsed 95 GHz EPR/ENDOR spectroscopy using a $\pi/2 - \tau - \pi/2 - T - \pi/2$ stimulated echo (SE) pulse sequence. The RF pulse is applied during the interval T . The spectrometer and its specific advantages have been described in detail [7].

3.3 Other measurements (TEM, EDX)

The TEM investigation were performed in a Philipps CM 30T, operated at 300 KV. Samples were prepared by first dispersing the powder into alcohol with ultrasonic bath, and then taking a drop of the suspension on a carbon coated 2.3 mm 400-mesh copper grid. The specimens were dried in air before the measurement. EDX was performed on Philipps XL 20 to identify the composition of the samples.

Chapter 4 Structural and optical properties of ZnO quantum dots

4.1 Introduction

ZnO has been known as a green luminescent material for a century and has been used in field-emission displays. In the recent years, the increasing interest in developing short-wavelength semiconductor lasers and the realization of room temperature green-blue diode lasers from wide bandgap semiconductors such as ZnSe (2.70 eV) and GaN (3.40 eV) [1-3] have stimulated great interest in ZnO (3.37 eV) as a possible option. The unique feature that ZnO has a large exciton binding energy (~ 60 meV), substantially larger than that of ZnSe (22 meV) and GaN (25 meV) which are comparable with the thermal energy at room temperature (26 meV), makes ZnO a promising candidate for room temperature ultraviolet (UV) laser. The room temperature UV lasing effect has been successfully observed in high quality ZnO epitaxial single crystal films [4, 5], ZnO nanowires synthesized with a vapor phase transport process [6], and nanocrystalline ZnO powder prepared at high pressure [7]. Questions arise related to whether the strong UV emission can take place in small size region (~ 10 nm) prepared by chemical routes.

Experiments so far showed that, the UV bandgap luminescence in as-prepared ZnO quantum dots via wet chemistry method is strongly quenched [8], and the broad oxygen-deficiency related [9, 10] green luminescent band is predominant. It was found that for such as-grown ZnO quantum dots, both the dots' size [11, 12] and the surface structure (existence of surface acetate group or OH group) [13, 14] have effect on the luminescence properties. By passivating the surface, a few authors were able to observe strong UV luminescence from ZnO quantum dots [15, 16]. A better understanding of the effects needs the clarification of the structure of the dots, i.e., the dot size and the surface conditions. From a practical point of view (e.g. nanolaser), investigations of the structural origin behind the weak excitonic recombination is instructive for exploring strong UV light from ZnO quantum dots. In chapter 2 we described the change of the structure by an annealing process. Here we report the effect of such changes on the luminescence properties.

4.2 Structural properties

Figure 4.1 shows the X-ray diffraction pattern of ZnO quantum dots and the reference samples. In the as-prepared unannealed sample (curve a) the diffraction peaks related to

wurtzite ZnO (curve g) are considerably broad. Upon annealing the diffraction peaks become more intense and narrower (see curves b, c, d), indicating increasing size. The average size of the particles can be estimated from the halfwidth of the diffraction peaks applying the Scherrer formula, and is approximately 4.3 nm in diameter for the unannealed sample, and are 4.8, 5.4, and 7.0 nm for the sample annealed at 150°C, 300°C, and 500°C, respectively. In addition to the ZnO diffraction pattern a peak at 59.5°, as indicated by the arrow in Fig. 4.1, is observed. It decreases upon annealing and vanishes above 300°C. A diffraction peak at the same angle is also present in the XRD spectrum of the freshly prepared Zn(OH)₂ (curve e), and this makes it very likely that it is related to Zn(OH)₂, keeping in mind that Zn(OH)₂ prepared in this work is almost amorphous, and Zn(OH)₂ in its pure orthorhombic form has the maximum XRD intensity at 60.5°. In the Zn(OH)₂ (150°C) sample (curve f) the 59.5° diffraction peak decreases, and sharp ZnO peaks appear. The line width gives evidence that in this case rather large ZnO particles (≈ 24 nm) are formed.

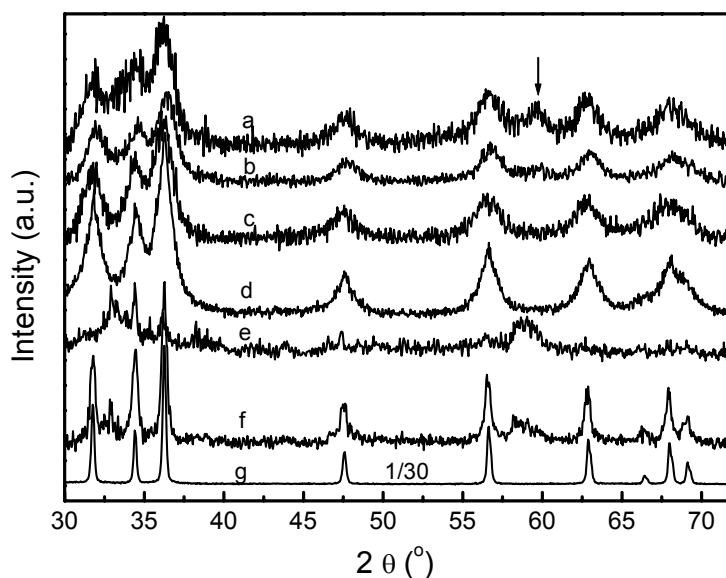


Figure 4.1 X-ray diffraction pattern of ZnO quantum dots (a-d) and reference samples (e-g): fresh unannealed (a); annealed at 150°C (b); 300°C (c); 500°C (d); Zn(OH)₂ (150°C) (e); Zn(OH)₂ (f); bulk ZnO (g).

The growth of ZnO QDs is also shown by the optical absorption spectra (figure 4.2). The unannealed dots exhibit quantum size absorption with the band-to-band absorption at 3.82 eV, at an energy substantially higher than that of the ZnO bulk reference sample (dotted line in

Fig. 4.2) which shows excitonic absorption at 3.29 eV. Upon annealing, the absorption peak shifts to lower energies, indicating the growth of the size.

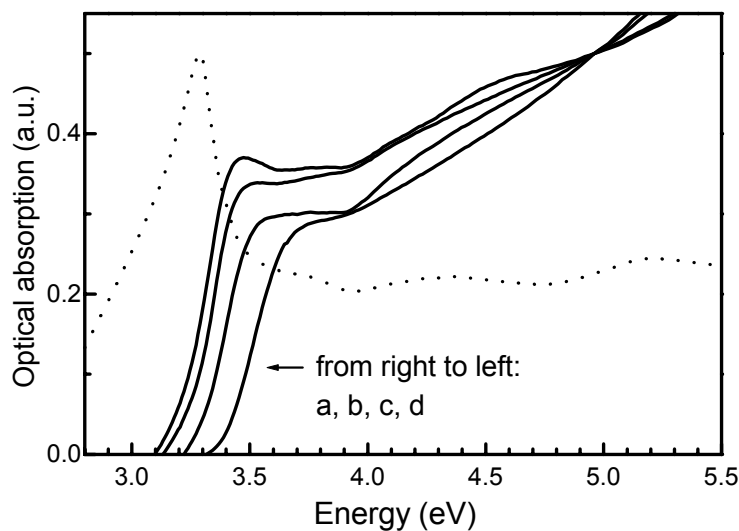


Figure 4.2 Optical absorption of ZnO quantum dots (a-d) and reference bulk ZnO (dotted line): unannealed (a); annealed at 150°C (b); 300°C (c); 500°C (d). The spectra of the dots have been normalized at 4.96 eV (250 nm).

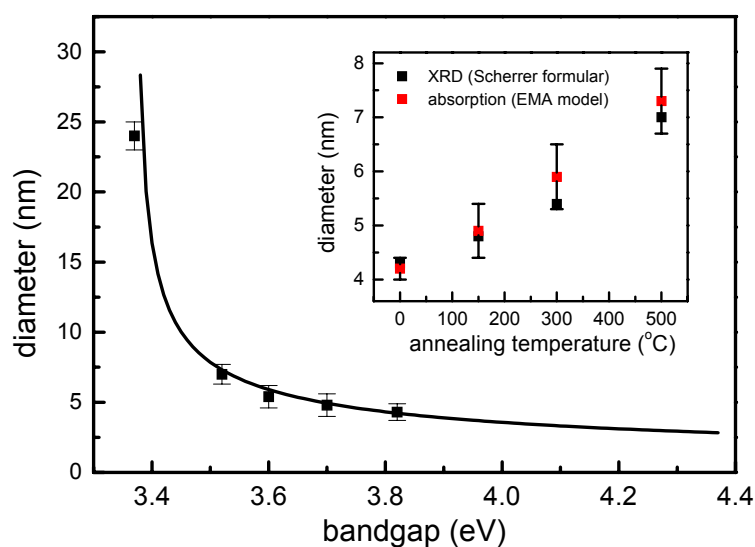


Figure 4.3 Plot of the particle size of ZnO quantum dots as a function of the bandgap. Comparison between the particle sizes calculated from XRD data and from absorption measurements is shown in the inset. The error bars show the size distribution.

According to the effective mass approximation, we can use the energy position to estimate the average particle size. With $E_g^{bulk} = 3.37 \text{ eV}$, $m_e = 0.28 m_o$, $m_h = 0.59 m_o$, and $\epsilon = 3.7$ taken from Ref. [17], the EMA model as expressed by equation (3.6) can be simplified as

$$\Delta E(\text{eV}) \cong \frac{2.007}{R^2(\text{nm})} \quad (4.1)$$

for ZnO QDs. Figure 4.3 shows a plot of the particle size as a function of the bandgap. We obtain 4.2 nm for the as-prepared dots and for the dots annealed at 150°C, 300°C and 500°C the average diameters of 4.9, 5.9, and 7.3 nm, respectively. These results are in very good agreement with the diameters obtained from the XRD data (see the inset of fig. 4.3 for a comparison). The size distribution which can be estimated from the width of the absorption peaks is about $\pm 10\%$.

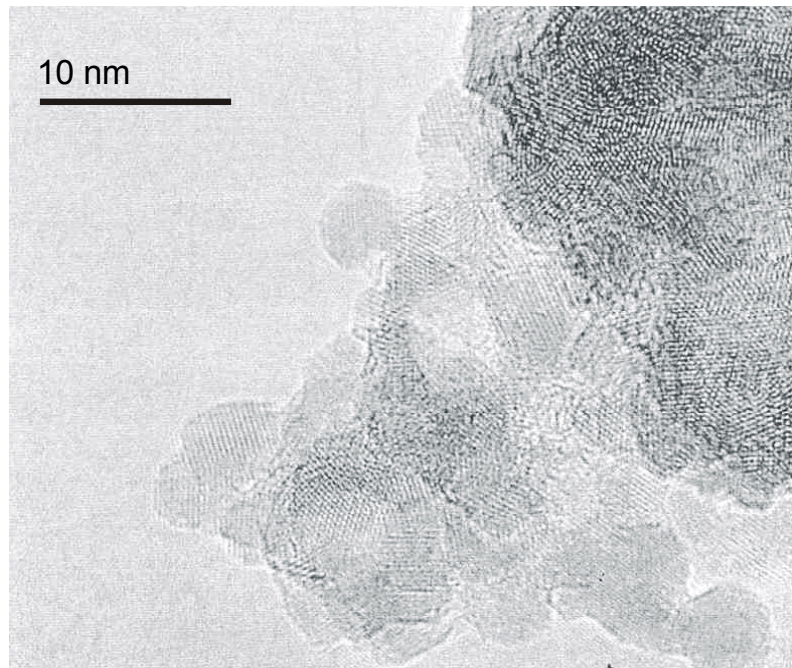


Figure 4.4 TEM image of as-grown ZnO quantum dots.

Figure 4.4 shows TEM image of as-grown unannealed ZnO quantum dots. The particle sizes are in the range of $4.2 \pm 0.4 \text{ nm}$, consistent with the calculated results from XRD and absorption measurements.

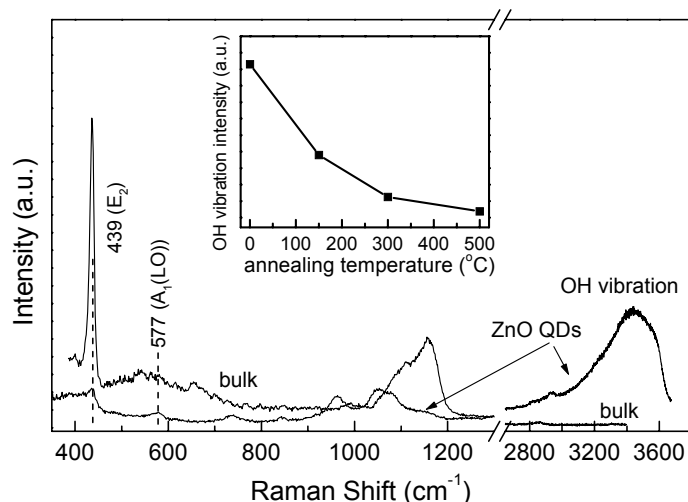


Figure 4.5 Raman spectra of ZnO quantum dots and bulk ZnO. The inset shows the change of the OH vibration at 3400 cm^{-1} upon annealing temperature.

The existence of $\text{Zn}(\text{OH})_2$ in ZnO quantum dots, or at least that of OH groups, is demonstrated by Raman spectroscopy (figure 4.5). In the range from 3200 cm^{-1} to 3600 cm^{-1} , where the OH stretching mode should appear, we observe a strong broad and unstructured band in the as-prepared quantum dots, while no signal is seen in the reference bulk ZnO. Upon annealing the intensity of this band rapidly decreases (see inset in Fig. 4.5). At lower energies we find the modes of the lattice vibrations of wurtzite ZnO (E_2 at 439 cm^{-1} , $A_1(\text{LO})$ at 577 cm^{-1} , and combination modes of LO-, TO-modes at higher energies). The important point here is that there exists $\text{Zn}(\text{OH})_2$ in the as-prepared ZnO quantum dots and upon annealing it is gradually released while the dot sizes increase.

4.3 Emission properties

Figure 4.6 shows the room temperature PL spectra of the ZnO QDs and the reference samples. The spectra in the visible region are fitted by Gaussian bands, as shown by the dotted lines in Fig. 4.6. For the as-prepared unannealed ZnO dots (curve a), the green luminescence band with a maximum at 2.34 eV is very strong, while the UV peak around 3.32 eV is much weaker. The intensity ratio is around 0.09. Upon annealing at 150°C , the UV band increases in intensity to a ratio around 0.35 and red shifts to 3.28 eV , while the green band shifts to 2.25 eV and a weak new blue band at 2.71 eV appears (curve b). For the sample annealed at 300°C , the UV band continues to increase and evolves into an prominent sharp

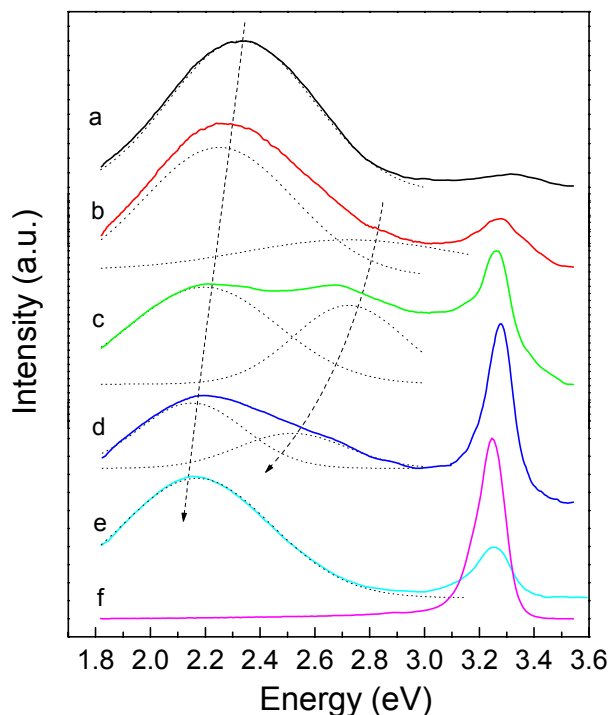


Figure 4.6 PL spectra of the corresponding ZnO quantum dots (a-d) as in fig. 2 and reference samples (e, f) at room temperature: Zn(OH)₂ (150°C) (e); ZnO bulk (f). The dotted lines are the fitted Gaussian bands. The dashed curves with arrows are guided for eyes.

peak at 3.25 eV (curve c). The green band red shifts to 2.20 eV, and the blue band reaches maximum intensity. With a further increase in the annealing temperature, the ratio of the UV to the green band continuously increases (curve d). The spectrum is reproduced by two transitions centered at 2.15 eV and 2.52 eV. No PL from 3.3 eV down to 1.8 eV was detected for Zn(OH)₂ powder. For the Zn(OH)₂ (150°C) sample, the weak UV band and the strong visible band at 2.16 eV (curve e) should then come from ZnO with large particle sizes. Only the UV emission at 3.21 eV is observed for the bulk OH-group free ZnO (curve f). It thus seems that, for ZnO quantum dots, the appearance of strong UV emission is closely related to the annealing process. In addition to the strong increase of the UV emission, the annealing treatment also introduces new emission bands in the visible region and causes a red shift of all visible bands, as shown by the dashed curves with arrows.

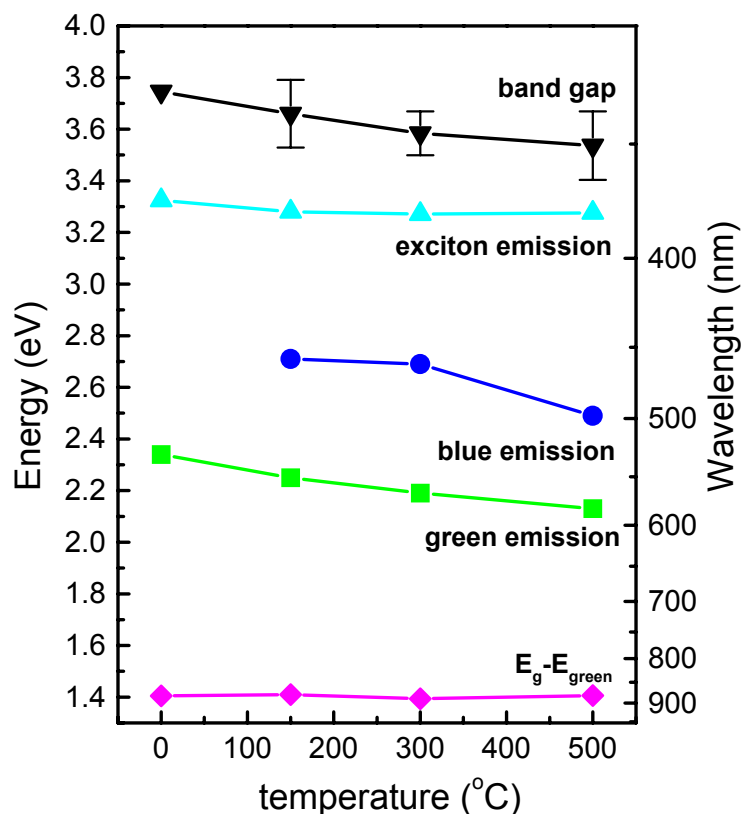


Figure 4.7 The change of the bandgap of ZnO quantum dots, and the luminescence bands vs. the annealing temperature.

The change of the bandgap of ZnO quantum dots, and the luminescence bands vs. the annealing temperature is illustrated in figure 4.7. With increasing annealing temperature, the bandgap, obtained from the absorption data, decreases with a variation of about 200 meV, while exciton emission energy keeps relatively stable with a slight decrease of 50 meV. Both the green and blue bands shift to lower energy. The green band closely follows the bandgap, indicating that these two are related. The energy difference between the bandgap and the green emission energy ($E_g - E_{green}$) is 1.4 eV, independent of the particle size. Similar results were observed by Anderson *et al* [13]. They concluded that the visible luminescence depends on the presence of the surface acetate group. As we didn't introduce any acetate group, the similarity of the results points to a common origin of the effects.

To investigate the origin of the green and the blue luminescence bands, photoluminescence excitation (PLE) spectra in the visible region are measured. Figure 4.8 (a) shows, as an example, PLE spectra monitored at five energy wavelength (615 nm, 580 nm, 520 nm, 474

nm, and 440 nm) in the PL spectrum of ZnO quantum dots annealed at 300°C, as indicated by the arrows in Fig. 4.8 (b). We find that, for the luminescence around the green band (615 nm and 580 nm), the excitation energies are in the region of 3.3-3.5 eV, at the onset of the absorption (see curve c in Fig. 4.2 for comparison). Essentially, the excitation spectra should be similar to those of absorption. The somewhat redshift of the excitation spectra is to great extent due to the strong absorption of the lower wavelength incident lights by the outmost layers of the sample, leaving mainly the longer wavelength around the absorption onset to penetrate into the sample to excite the luminescence. Accordingly the excitation shifts to lower energy, and the excitation spectrum has a sharp peak around the onset wavelength. The green emission is, therefore, a result of the band-to-band excitation, and is ascribed to the radiative recombination of defects trapped electron and holes, created by the bandgap absorption.

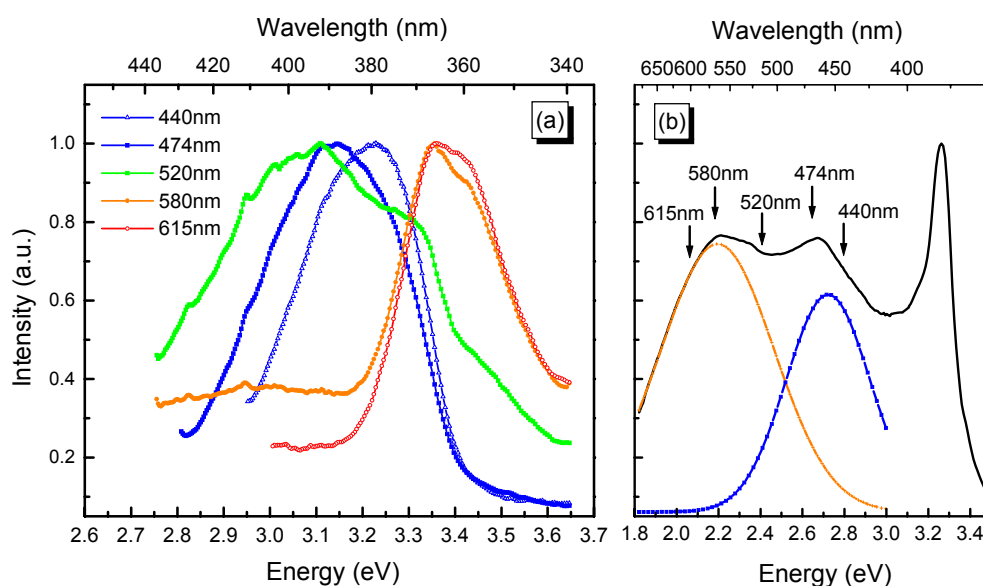


Figure 4.8 PLE spectra (a) of ZnO quantum dots annealed at 300°C monitored at $E_M = 440$ nm, 474 nm, 520 nm, 580 nm, and 615 nm, as indicated by the arrows in the PL spectrum (b). The PLE spectra have been normalized at maximum intensity.

However, the excitation of the luminescence around the blue band (440 nm and 474 nm) is different, surprisingly located at lower energy (3.0-3.3 eV), indicating they are excited directly from midgap states. Due to the strong overlap, the excitation of the intermediate 520 nm band has the hybrid character of the lower and higher energy luminescence. The different PLE spectra show clearly that the green and the blue band have different mechanisms.

4.4 Core-shell model

4.4.1 ZnO/Zn(OH)₂ core-shell model

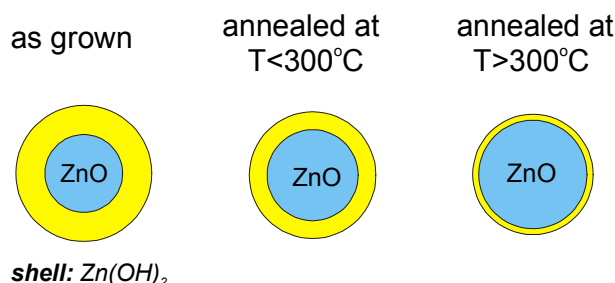


Figure 4.9 A model proposed for the structure of ZnO quantum dots. Upon annealing, the core ZnO grows and the shell becomes thinner due to the thermolysis, as shown schematically from left to right.

Considering the presence of Zn(OH)₂ in ZnO quantum dots, it is reasonable to propose that Zn(OH)₂ forms a thin layer on the surface of ZnO quantum dots, thus forms a ZnO/Zn(OH)₂ core-shell structure. A corresponding model is proposed in figure 4.9. Upon annealing, the core ZnO grows and the shell becomes thinner due to the thermolysis.

One might argue for the existence of independent Zn(OH)₂ nanoparticles. The probability is very low because of the preparation method, i.e., the dehydration properties of the alcohol. Since ZnO is extremely sensitive to H₂O environment [18], the situation in ZnO QDs should be even more severe.

To investigate the properties of the surface, we exposed the dots to two different ambience for 1 month: one was dry N₂, the other was humid air. It was found that the dots stored in dry N₂ maintain the same properties as the fresh ones. For those exposed to humid air, compared with the original states, even weaker and broader XRD patterns are obtained (see curves a' and b' in figure 4.10 (I)), indicating decreasing crystallinity and size. In addition, the Zn(OH)₂-related diffraction, as shown by the arrow, increases upon exposure, indicating the appearance of more Zn(OH)₂. This study therefore confirms that the surfaces of the dots are covered by Zn(OH)₂.

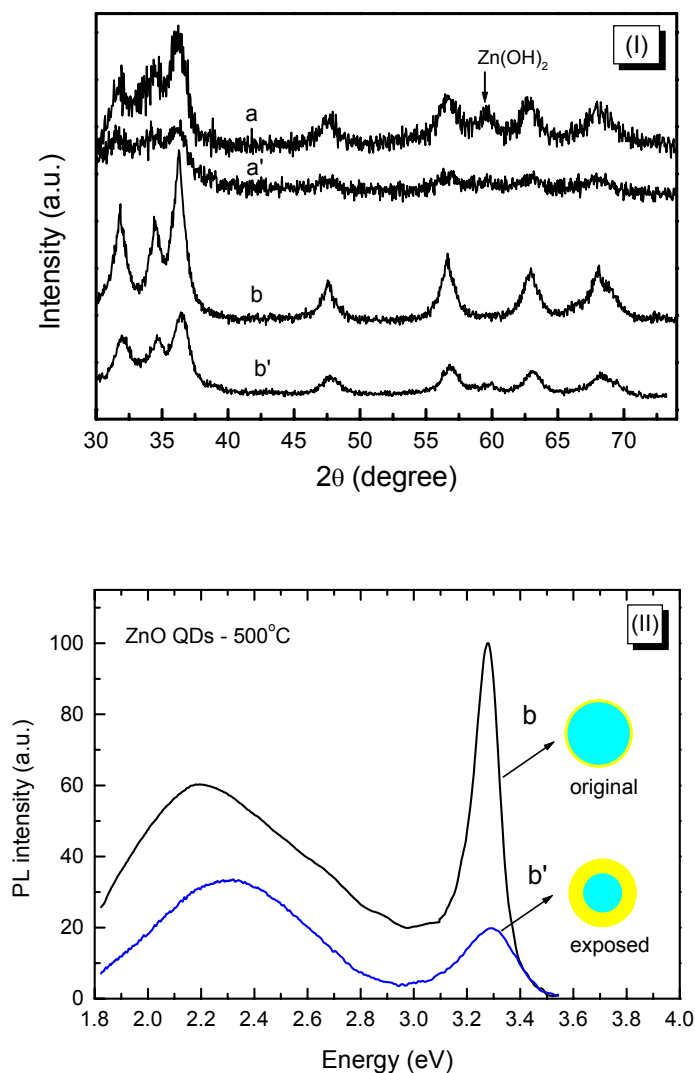


Figure 4.10 XRD pattern (I) and PL spectrum (II) of ZnO quantum dots before (a, b) and after exposed to humid air (a', b'): fresh unannealed (a); annealed at 500°C (b); (a) exposed to humid air for one month (a'); (b) exposed to air for one month (b'). The inset in (II) shows the schematic structure of the corresponding sample.

4.4.2 Thickness of the shell

The most direct way to evaluate the thickness of the shell should be the TEM observation. However since Zn(OH)_2 is amorphous, the contrast between the shell and the carbon foil support is not well defined, and this makes such an observation is very difficult. However, we can give a rough but simple estimation by comparing the size changes of ZnO quantum dots

before and after annealing because the core grows on the consumption of the shell, as indicated by XRD experiments. The thickness is in the range of 0.5 ~ 1.3 nm.

4.5 Correlation of the optical properties with the structure

4.5.1 The appearance of strong UV emission

We now discuss the appearance of the strong UV emission in ZnO quantum dots. As the dot size grows with annealing, it might be concluded that the strong UV emission is related to bigger particle size. If this would be the case, even stronger UV emission should have been observed for the reference Zn(OH)₂ (150°C) sample, i.e., ZnO dots with much bigger size (24 nm in diameter). This is however in contradiction with the observation (see curve e in Fig. 4.7). In addition, earlier work showed that the UV band increases very slightly with increasing particle size and the green band remains dominant. It is therefore not sufficient to correlate the strong UV emission in this work only with the growth of the particles.

Based on the core-shell structure, we suggest that the weak excitonic transition of ZnO quantum dots is strongly correlated with the presence of the surface shell of Zn(OH)₂. When the Zn(OH)₂ shell is present, the excitonic emission from ZnO QDs is suppressed. This is perhaps the reason why strong UV emission was not observed before in the as-prepared unannealed and not intentionally surface capped ZnO quantum dots by other groups with the similar method.

Figure 4.10 (II) shows the PL spectra of the original (curve b) 500°C annealed ZnO quantum dots and exposed to humid air for one month (curve b'). The original almost Zn(OH)₂ free sample shows a strong UV peak, while a quenched UV emission when exposed to humid air, which contains a thicker Zn(OH)₂ shell, as shown by the inset schematic diagram (see also the corresponding XRD pattern, curve b' in Fig. 4.10 (I)). Upon exposing to air, the visible luminescence blue shifts. The observations of strong UV luminescence from surface capped OH free ZnO quantum dots [15, 16] give additional convincing support to our model. The weak UV emission in the Zn(OH)₂ (150°C) sample is then also due to the presence of large amount of Zn(OH)₂ on the surface of the big ZnO particles. However, the details of the bonding of the Zn(OH)₂ shell to the ZnO core, leading to the quenching of the ZnO excitonic emission in ZnO are not clear yet.

4.5.2 The appearance and change of the visible bands

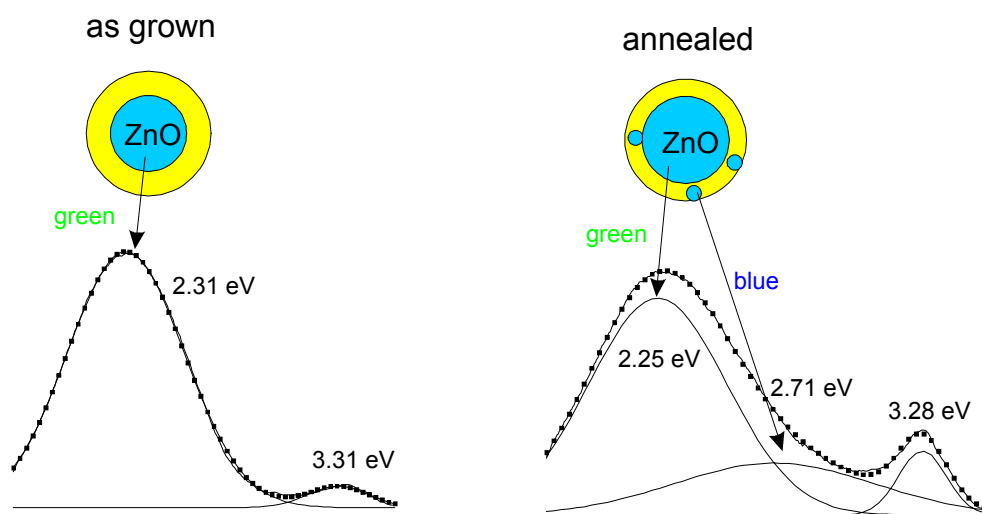


Figure 4.11 Scheme of the origin of the visible emission bands based on the core-shell model.

With the core-shell model, we can now explain the appearance of the blue band. It is attributed to the decomposition of the surface Zn(OH)_2 (when the temperature is higher than 125°C), which nucleates to new small ZnO clusters and grows upon annealing, as demonstrated in figure 4.11. The new dots are so small that even the crystal structures are maybe not well developed, and therefore lack of band-to-band excitation (look back fig. 4.8). The bigger dots have, obviously, better crystal quality, and are responsible for the green emission.

The red shift of this new band and the original green band can be well explained according to the size-dependent luminescence [19-21], i.e., the emission energy of a quantum dot strongly depends on its size, the smaller the size, the higher the energy.

In summary, we have investigated the effect of different processing conditions on the luminescence properties of ZnO quantum dots. We provide strong evidence that the as-prepared dots consist of a ZnO/Zn(OH)_2 core-shell structure. When Zn(OH)_2 is present, the excitonic transition of ZnO QDs is quenched. This is probably the main reason behind the commonly reported weak excitonic emission of ZnO QDs where the surface is capped by Zn(OH)_2 . Strong UV emission is observed for dots annealed at high temperatures, when the outer shell of Zn(OH)_2 is released.

Chapter 5

Defects and doping in ZnO quantum dots and electronic properties (I)

5.1 Introduction

Doping of semiconductor nanocrystals have received special attention as one expects novel physical properties and functionalities from such system [1] due to the quantum confinement of the extra carriers introduced by doping. However, the electronically active doping remains a main challenge for most of the semiconductor nanocrystals prepared by colloid chemical methods. From this point of view, the inherent n-type doping of ZnO may offer great interest and special advantages for the nanoscale regime.

In the recent years knowledge about the nature of the residual donors causing the inherent n-type conductivity of nominally undoped bulk ZnO has been greatly improved. Traditionally, residual impurities such as halogen atoms (Cl) or group-III elements (Al, Ga) were considered as well as intrinsic defects like the oxygen vacancies or Zn interstitials [2]. However this long-time favored mechanism has been recently strongly questioned by a first-principle investigation [3] that none of the native defects exhibits characteristics consistent with a high-concentration shallow donor: zinc vacancies behave as deep acceptors and oxygen vacancies as deep donors. The prevailing n-type conductivity can therefore not be attributed to any native defects. The study further predicted that hydrogen might cause shallow donor in ZnO. The prediction was supported by our recent magnetic resonance studies [4] on the undoped ZnO single crystal, and revealed that H is a responsible shallow donor with binding energy of 35 ± 5 meV and g values of $g_{//c} = 1.9569 \pm 0.00005$, $g_{\perp c} = 1.9552 \pm 0.00005$ (g parallel and perpendicular to the crystal c-axis).

An open question about the donors in nominally “undoped” ZnO quantum dots is naturally put forward. In this chapter we attempt to answer this question by magnetic resonance studies. The electronic properties of the defects in ZnO quantum dots are investigated by conventional electron paramagnetic resonance (EPR) performed at X band (9.5 GHz) and high resolution EPR performed at 95 GHz, and electron nuclear double resonance (ENDOR). Intentional doping with Mn in ZnO quantum dots will be discussed separately in part II, chapter 6.

5.2 EPR studies at 9.5 GHz

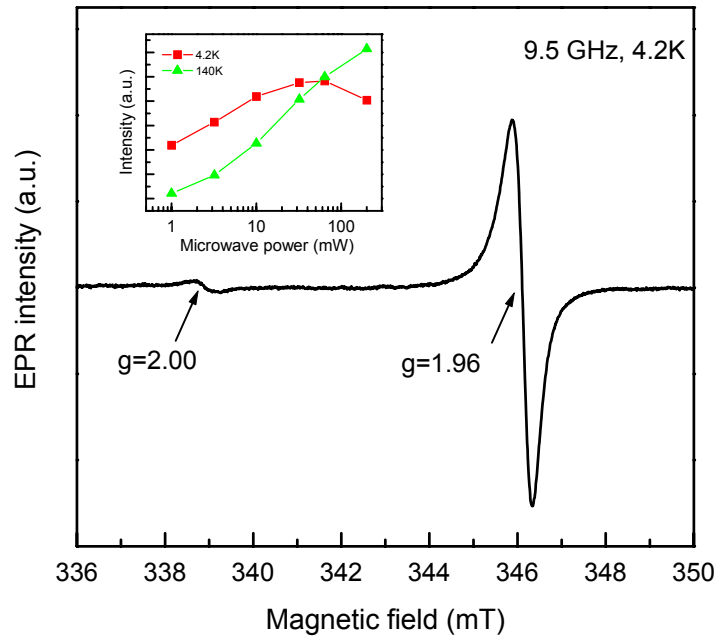


Figure 5.1 A typical EPR spectrum of ZnO quantum dots measured at 4.2 K. The inset shows the power dependent intensity.

A typical EPR spectrum of ZnO quantum dots is shown in figure 5.1. Two resonance signals can be seen, with one at around 338 mT, and the other at around 346 mT. The resonance position of the latter corresponds to a g -value of 1.96, which is close to that of the shallow donor in bulk single crystals. The resonance position gives already a first indication that the signal arises from shallow donors. The free-electron like g -value of the other signal ($g \sim 2.00$) indicates that the resonance should originate from deep defects. Due to the random orientation of the quantum dots, the anisotropy of the g -values of the shallow donor in the single crystals is not observed here. The inset shows the intensity of the $g \sim 1.96$ EPR signal measured at different microwave power. At low temperatures ($< 140\text{K}$) the EPR signal saturates at microwave powers higher than 30 mW, while at higher temperatures there is no saturation. In the following experiments we show the EPR spectra measured at an unsaturated power of 10 mW. Since only shallow donors contribute to the conductivity, we will focus on the shallow donors in this chapter. The deep defects will be briefly discussed in the last section.

For shallow donors in bulk single crystals we expect that at low temperatures the electron is bound in the ground state hydrogenlike orbit of the impurity center, thus the unpaired extra electron is in the paramagnetic D^0 state. The occupation of the neutral shallow donor depends on temperature. The number of unionized neutral donors (i.e. the paramagnetic centers) is

$$N = \sum_i N_{0i} (1 - e^{-E_{Bi}/k_B T}) \quad (5.1)$$

here N_{0i} is the total number of the i th neutral donor, E_{Bi} the activation energy of the i th donor, and k_B is the Boltzmann constant. When the temperature is increased the donor electron are released to the conduction band, leaving the donor in the positive diamagnetic charge state D^+ , thus causing a decrease of the EPR signal.

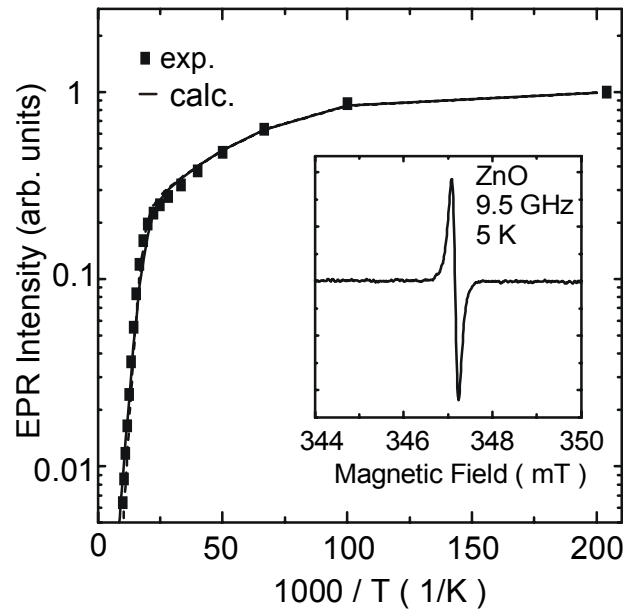


Figure 5.2 EPR spectrum of ZnO single crystal (inset) and the change of the EPR intensity with temperature. The solid line shows the result of the calculation according to Eq. (5.1).

In the 9.5 GHz EPR experiments the signal of the shallow donor typically vanishes at temperatures higher than 150 K (see fig. 5.2). Above this temperature the single crystals become conducting due to the thermal release of the donor electrons to the conduction band. The conducting electrons shield the microwave field and make it impossible to detect the EPR signals. The temperature dependence can be well described by an activation energy of ~ 40 meV or by two donors with 35 meV and 60 meV binding energies [4]. The latter is consistent with the Hall analysis of the sample (see below).

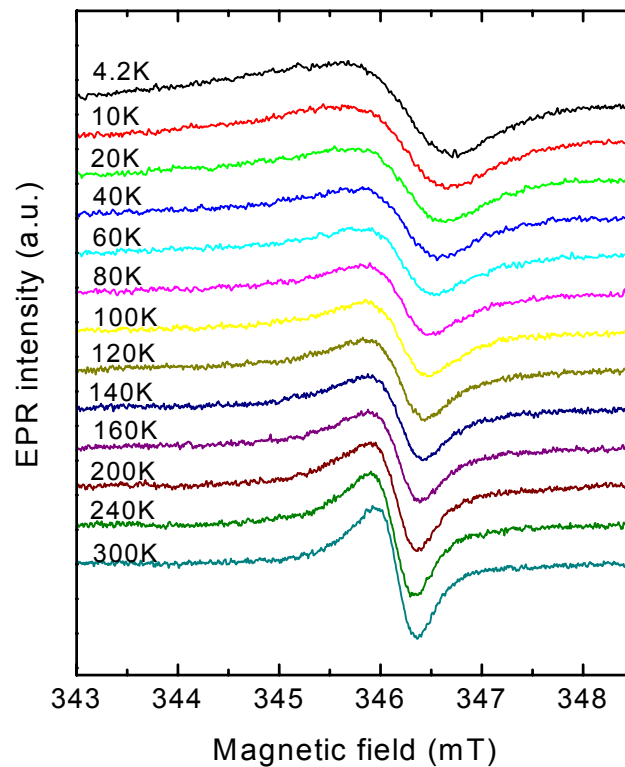


Figure 5.3 Temperature dependence of EPR spectra of ZnO-7nm (ZnO-500°C) quantum dots.

Figure 5.3 shows the temperature dependence of EPR spectra of ZnO-7nm (ZnO-500°C) quantum dots measured from 4.2 K to room temperature (RT = 300K). Remarkable is that the resonance is measurable up to RT. For the temperature range used in our experiments the electrons in the quantum dots are always localized within the dots, which prevents any macroscopic conduction and allows to detect the EPR signals even at elevated temperature.

5.3 EPR studies at 95 GHz

Hall measurements on ZnO single crystals yield that two donors are present in the material with binding energies of about 35 meV and 60 meV, while the 9.5 GHz EPR shows only one donor resonance. It might be caused by the limited resolution of this experiment, i.e. the donors have very similar g -values. To enhance the spectral resolution, 95 GHz EPR can be used. We apply this measurement also to the nanocrystals to compare the results.

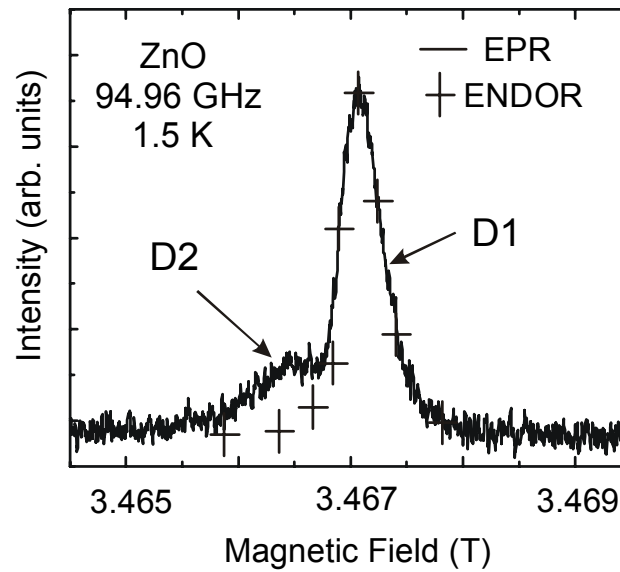


Figure 5.4 95 GHz EPR spectrum of ZnO single crystal. The symbols (crosses) give the intensity dependence of the ^1H ENDOR lines on the magnetic field.

Figure 5.4 shows the EPR spectrum of ZnO single crystals measured at 95 GHz and at 1.5 K. Owing to the high resolution, the resonances of two donors, D1 and D2, are distinctly resolved. With increasing binding energy the deviation of the g values from that of the free electron value (2.0023) should become smaller, according to

$$g - 2.0023 = \lambda / \Delta E \quad (5.2)$$

with λ the spin-orbit coupling and ΔE the energy separation to the next state. Therefore, D1 with smaller g -value is a comparatively shallower donor and D2 a deeper one with larger binding energy.

Similar EPR spectra of the two shallow donors are also observed in ZnO nanocrystals and ZnO bulk powder, see figure 5.5. Both the resonance positions of D1 and D2 shift to higher field (corresponding to smaller g -values) when the size of the ZnO particles increases. When illuminated with light, the resonance intensity dramatically increases due to the higher concentration of the paramagnetic centers created by the light.

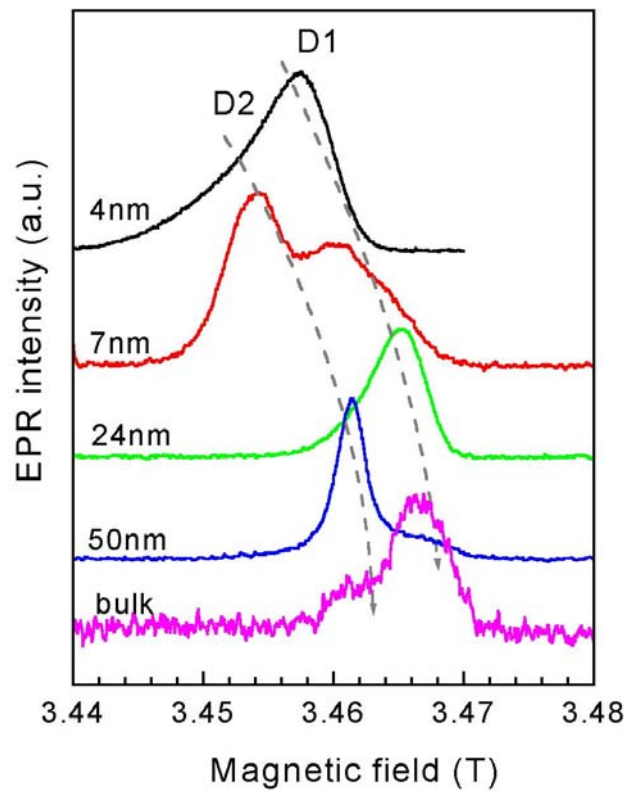


Figure 5.5 High resolution EPR spectra of shallow donors in different ZnO samples measured at 95 GHz and 1.5 K. Two donors, D1 and D2, are distinctly separated. Both the resonance of D1 and D2 shifts to higher magnetic field with increasing particle size, as indicated by the dashed curves with arrows.

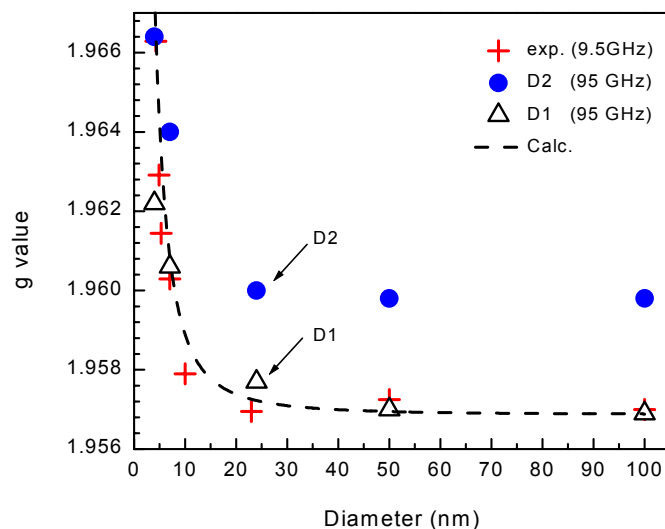


Figure 5.6 Change of the g-values of D1 and D2 (measured at 95 GHz) with particle size, compared with the experimental data measured at 9.5GHz (sign crosses) and the calculation (dashed curve). A discussion will be presented in section 5.4.

Shown in figure 5.6 is the variation of the g-values of D1 and D2 with particle size, together with the g-values of the shallow donors measured by conventional EPR. It can be seen clearly that the 9.5 GHz EPR experiments measure the g-values of D1. Its g-value decreases from 1.966 for 4.2 nm to 1.957 for big size nanocrystals. With increasing particle size, the g-value of D2 also decreases, however about 0.003 larger than that of D1. Here the size of the bulk ZnO is taken as 100 nm for convenience.

5.4 Results discussion

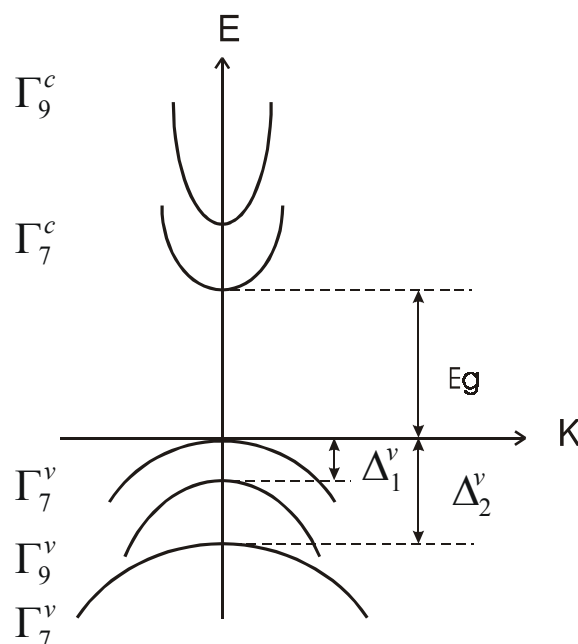


Figure 5.7 Schematics of the band structure near $k = 0$ in wurtzite semiconductors which concludes a five-band calculation.

In this section we discuss the change of the g-values of the shallow donors. The result can be understood within the frame of $\vec{K} \cdot \vec{P}$ theory, which was developed to predict electronic properties such as the effective mass (m^*) and the Landé g-factor (g^*) in the vicinity of the extremal points of semiconductors band structure from the experimentally determined parameters as, e.g. bandgap and spin-orbit splitting. The value of g^* is different from the free electron Landé factor due to the presence of the spin-orbit interaction. Taking the spin-orbit interaction of the valence band and its influence on the properties of the lowest conduction band electrons, a three-band model was developed [5], and g^* is expressed as

$$g^* = 2 - \frac{2P^2 \Delta_1^v}{3E_g (E_g + \Delta_1^v)} \quad (5.3)$$

where E_g is the bandgap, Δ_1^v is the spin-orbit splitting of the highest lying valence band, and P is interband-matrix-element describing the coupling between the conduction band and the valence band. The schematics of the band structure near $k = 0$ in wurtzite semiconductors involving five-band calculation is shown in figure 5.7. For ZnO $P^2 = 20$ eV and $\Delta_1^v = 6$ meV [6]. Eq. (5.3) predicts that with decreasing bandgap energy the deviation of g^* from the free electron g value becomes larger. Now the question is whether this theory is able to describe the size dependence for ZnO.

We showed in chapter 3 that according to the effective mass approximation, the enlargement of the bandgap with decreasing particle size (when it is in the order of the Bohr radius) due to quantum size confinement effect can be expressed by

$$E_g = E_{g_0} + \frac{\hbar^2 \pi^2}{2R^2} \left[\frac{1}{m_e} + \frac{1}{m_h} \right] - \frac{1.786e^2}{\epsilon R} \quad (5.4)$$

where E_{g_0} is the bandgap of the corresponding bulk material. Introducing the larger bandgap energies into Eq. (5.3) predicts a decreasing g^* value with increasing size.

The size dependent g -value of ZnO nanocrystal is plotted by the dashed line in fig. 5.6. One can see that the variation of the experiment g -value of D1 donor is well described. The g -value shifts towards $g = 2$ in the nanocrystals with reduced diameter. For nanocrystals with diameters below 10 nm one has to take the quantum size effect into consideration. The Bohr radius r_D of the shallow donor wave function in ZnO bulk crystals can be obtained from effective mass theory as $r_D = (\epsilon/\epsilon_0)/(m^*/m_0) \times r_B = 1.5$ nm, with $\epsilon = 8.65$ the dielectric constant, $m^* = 0.3 m_0$ the effective mass, and $r_B = 0.053$ nm the Bohr radius of hydrogen atom. Thus the carriers in nanocrystals with diameters in the order of 2~3 times of this radius are confined in the spheres of the nanocrystal potential which leads to remarkable increase of the bandgap energy. We have seen this effect in absorption measurements (Fig. 4.2). With increasing bandgap energies the influence of the valence band on the g -value becomes smaller which explains its increase towards the free electron g -value. Bigger size nanocrystals exhibit almost no quantum size effect, and therefore the g -values are close to that of the bulk (1.957). The result implies that the EPR signal originates from shallow donor centers with an extended wave function, which can be described by the $\vec{K} \cdot \vec{P}$ approach. As for the g -value of D2, we

probably need to take the influences of more bands (or details of the donor structure) into account.

5.5 Chemical nature of the donors (ENDOR studies)

Obviously, the EPR results do not provide information on the chemical nature of the shallow donor species present since no resolved hyperfine structure is observed. We therefore performed ENDOR spectroscopy at 95 GHz and at 1.5 K using a method which is based on the stimulated echo (SE) pulse sequence [6].

5.5.1 Cause of the shallow donors

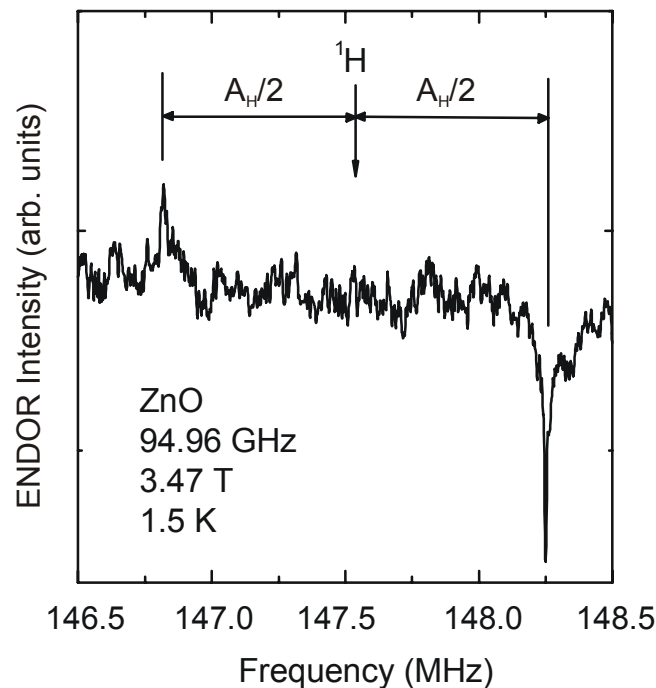


Figure 5.8 The ENDOR spectrum of H as the D1 donor in ZnO single crystals.

Our measurement on ZnO single crystals showed one of the two shallow donors is H. In figure 5.8 we observe two ENDOR lines symmetrically placed around the nuclear Zeeman frequency of ^1H . The 1.4 MHz separation of the two lines corresponds to a hyperfine interaction of $A_H = 1.4 \text{ MHz}$ ($4.66 \times 10^{-5} \text{ cm}^{-1}$). Thus H is located within the electron wave function of the shallow donor. When we satisfy the ^1H ENDOR resonance condition, and then measure the EPR spectrum, we find that the ^1H ENDOR is only correlated with the D1 EPR signal (see the sign cross in figure 5.4). Therefore H is the cause of D1 in single crystals.

To check whether H is also present as a relevant shallow donor in ZnO nanocrystals, we performed ENDOR experiments in the magnetic field around 3.46 T (see fig. 5.9). At the nuclear Zeemann frequency of ^1H (147.2 MHz) a strong ENDOR signal is observed as a dip, which immediately tells the existence of H in the sample. However, no hyperfine splitting is observed. It tells that the H nuclei are distant to the electron wave function of the shallow donors, i.e. most likely localized in the $\text{Zn}(\text{OH})_2$ shell of the nanocrystals. This result is rather surprising, since during the preparation of the nanocrystals plenty of hydrogen is present. A distinct difference from the bulk growth of ZnO is that the nanocrystals are synthesized at room temperature, while the bulk crystals growth proceeds at 1200°C , which implies that the incorporation of hydrogen into the lattice of ZnO requires thermal activation. So far we are unable to detect ENDOR signal on D2 in nanocrystals, as well as in the bulk materials.

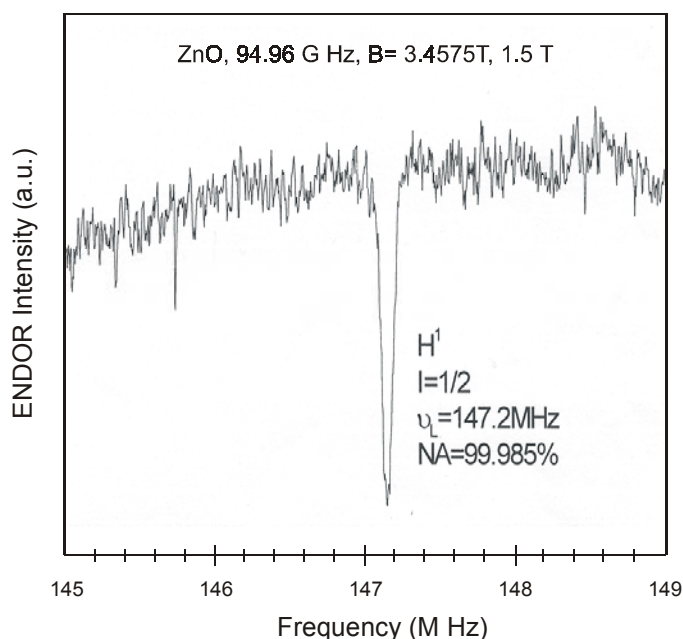


Figure 5.9 The ENDOR spectrum of H^1 nuclei observed in ZnO nanocrystals.

5.5.2 Cause of the deep donor

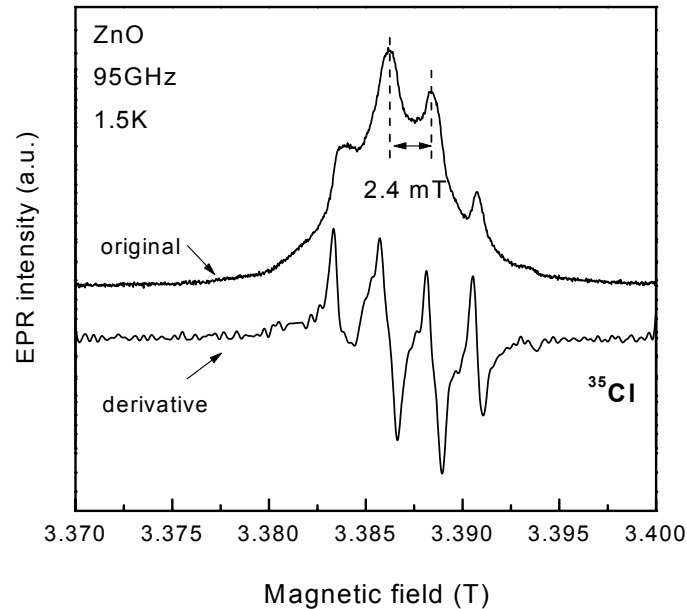


Figure 5.10 High resolution EPR of ZnO quantum dots measured at 95 GHz, 1.5 K. A well structured signal with four hyperfine splittings of 2.4 mT from ^{35}Cl is identified.

Investigating the $g \sim 2.00$ signals in the quantum dots in more details we find that the spectra show a well structured signal with four hyperfine lines with 2.4 mT distance. Figure 5.10 shows the resonance of ZnO quantum dots in magnetic field around 3.385 T. The pattern of four lines suggests an interaction with a nucleus of spin $I = 3/2$. The intensities indicate this isotope must have high abundance.

To obtain information on the chemical nature, we performed ENDOR experiments on the common residual impurities (Na, Cl, Cu, and Ga). All these isotopes have nuclear spin of $3/2$ and high abundance (see Appendix II). However the ENDOR result is that Cl is the responsible element. Similar to the case of hydrogen we expect the ENDOR transitions to be

at the frequencies $\nu_{\text{ENDOR}} = \nu_N \pm \frac{A}{2}$, as what we have seen in figure 5.8. For the two Cl

isotopes, Cl^{35} and Cl^{37} , the nuclear Zeeman frequencies ν_N are 14.2 MHz and 11.8 MHz, respectively. The hyperfine interaction we know from the EPR experiments is 2.4 mT (= 67.2 MHz). Thus the expected position of the ENDOR lines are 45.4 MHz for the Cl^{37} ($\nu_N + A/2$), and 47.8 MHz for the Cl^{35} isotope. This is indeed observed in the experiment (see figure

5.11). The two isotopes, ^{35}Cl (abundance 75.77%) and ^{37}Cl (abundance 24.23%), are identified. The $(\nu_N - A/2)$ transitions are not shown due to their lower signal to noise ratio.

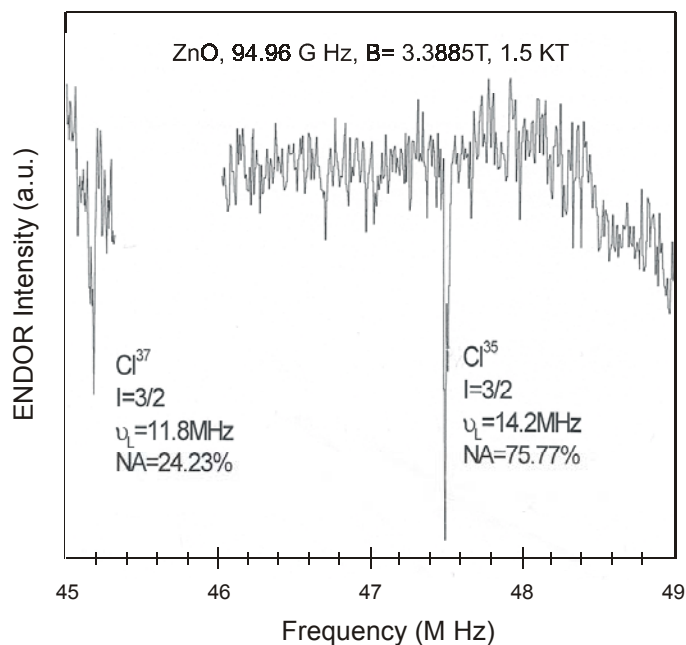


Figure 5.16 The ENDOR spectrum of Cl^{35} and Cl^{37} nucleus in ZnO nanocrystals.

In summary, we observed three kinds of donor impurities in the nanocrystals. Cl is a deep donor ($g \sim 2.00$), and H and the other are shallow donors ($g \sim 1.96$), whose nature is at the moment yet unknown. To identify the chemical nature of the shallow donor, further experiments are needed.

Chapter 6

Defects and doping in ZnO quantum dots and electronic properties (II)

6.1 Introduction

In this chapter we investigate doping in ZnO quantum dots with the transition metal Mn. Semiconductors doped with magnetic ions (usually transition metal or rare earth element), so called diluted magnetic semiconductors (DMS), and their nanostructures have been of great interest in the last decades, due to the combined magnetic properties from the magnetic elements and the transport properties from the carriers of the host [1-3]. In spite of the tremendous studies on Mn doped II-VI chalcogenide semiconductors [1, 2] and III-V DMS [3], ZnO:Mn system, however, has been surprisingly ignored.

The work of Mn-doped ZnO ($\text{Zn}_{1-x}\text{Mn}_x\text{O}$, x : Mn concentration) is stimulated by the following facts:

- (i) ZnO has a large electron mass, $\sim 0.3 m_0$, being expected to exhibit a strong magnetic interaction between mobile carriers and localized magnetic ions;
- (ii) ZnO is transparent in the visible regime due to the large band gap (3.37 eV), making transparent magnets feasible;
- (iii) ZnO is a promising candidate for ultraviolet laser devices due to the large exciton binding energy (60 meV), making room temperature magnetic and optical hybrid devices possible based on a single compound;
- (iv) High solubility of Mn in ZnO matrix because of the similar size: the ionic radii of Mn^{2+} and Zn^{2+} are 0.80 Å and 0.74 Å respectively.

In addition, Mn-doped ZnO is predicted [4] to be ferromagnetic with a very high Curie temperature ($T_c > 300$ K) if it can be doped p -type. From the practical point of view, this system is more attractive than the III-V based DMS (i.e. (In,Mn)As [5], (Ga,Mn)As [6]) whose potential applications are obstructed because of the too low T_c (normally as low as 100K) and low solubility of Mn in them.

The recent experimental breakthrough of the preparation of p -type ZnO [7-9] from the theoretical predication [10], and the successful synthesis of ZnO:Mn epitaxial thin films [11] will probably lead to a “Renaissance” of ZnO. The contributions to the latest international conference on spintronics in semiconductors underline the increase of the importance of the

ZnMnO system [12]. Obviously, there is an urgent need to understand the basic atomic structure of Mn in ZnO for future applications.

However, we notice that except the very early work by Dorain [13] information about the symmetry and electronic structure of Mn in ZnO is lack of report, and till now there is no work reported on ZnO:Mn nanocrystals. To probe the symmetry and electronic structure of the ground state Mn^{2+} in ZnO nanocrystals, we have conducted electron paramagnetic resonance (EPR) measurements.

In this chapter we deep our investigation from the macrostructure of ZnO:Mn quantum dots into the microstructure around Mn^{2+} ions in the dots. EPR spectra of ZnO:Mn quantum dots with different Mn concentration and different size and structure (changed by the annealing process, as illustrated forehead in chapters 2 and 4) are studied at temperatures from 4.2 K to RT. Three distinct EPR spectra can be distinguished. The first reveals Mn ions in hexagonal structure. The second reveals sites in disordered environment. The third is correlated to the Mn-Mn cluster interaction.

6.2 Structure of $Zn_{1-x}Mn_xO$ quantum dots

In our study, the Mn concentration x , determined by EDX falls in the range from 0.01 to 0.11 for the nanoparticles and 0.05 to 0.21 for the polycrystals. Figure 6.1 shows EDX spectra of $Zn_{1-x}Mn_xO$ quantum dots with $x = 0.01, 0.036, 0.05, \text{ and } 0.11$. The two characteristic signals identifying Mn, $MnK\alpha$ and $MnK\beta$, can be barely observed for $Zn_{0.99}Mn_{0.01}O$ quantum dots, while they rise up sharply when x increases. The strong Au signals come from the Au film which was sputtered onto the surface of the quantum dots powder for the EDX measurements in vacuum. The x value determined by EDX, which we call final x value, is almost half of the experimental stoichiometry, experimental x value (see Table 6.1), indicating about 50% Mn is missing during the preparation process with the wet chemical method. We should mention here that in our work Mn is deliberately “heavily” doped in ZnO quantum dots because too low Mn concentration is not for practical application, but merely for research interest.

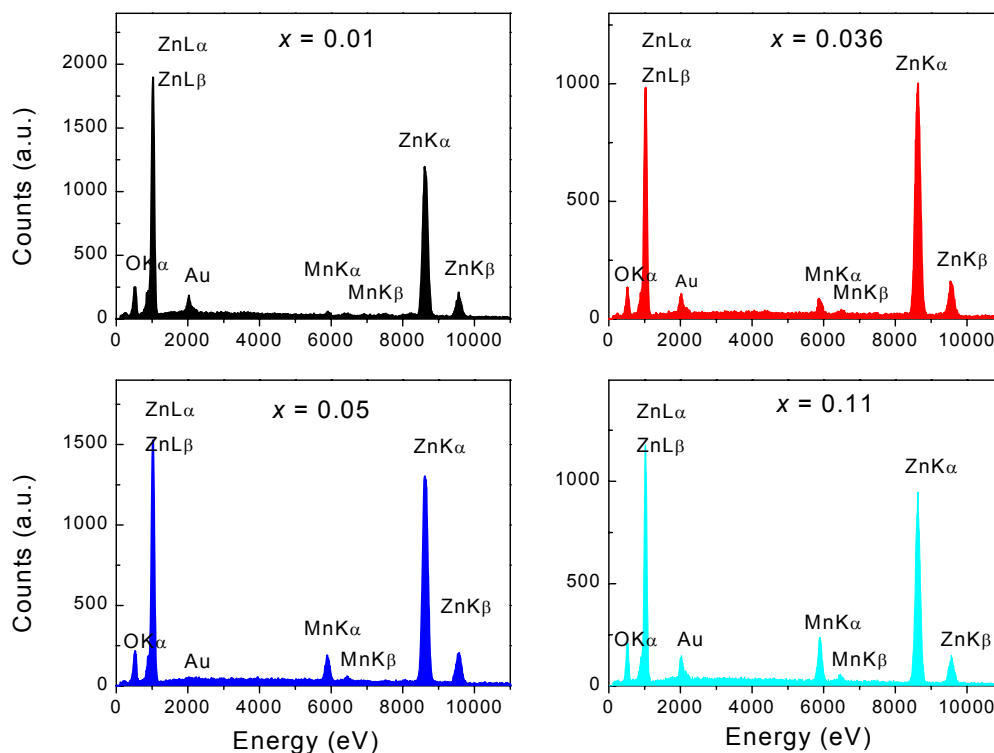


Figure 6.1 EDX spectra of Zn_{1-x}Mn_xO quantum dots with $x=0.01$, 0.036, 0.05, and 0.11.

Table 6.1 Comparison of the experimental and final x values of Zn_{1-x}Mn_xO quantum dots.

Experimental x value	0.167	0.07	0.10	0.20
Final x value	0.01	0.036	0.05	0.11

To investigate whether there is a MnO phase segregation, X-ray diffraction was performed. Figure 6.2 shows XRD pattern of Zn_{0.89}Mn_{0.11}O quantum dots. It can be seen that only the diffraction peaks related to wurtzite ZnO are present. At the positions where the three most intensive diffraction of MnO from facets (111), (200), and (220) should appear, as shown by the arrows in fig. 6.2, no diffraction peaks show up, indicating there is no MnO phase segregation, but a solid solution of ZnMnO is formed. This is in good agreement with the Zn_{1-x}Mn_xO phase diagram [14] which shows complete solubility of Mn in ZnO up to $x=0.2$ at 900°C.

Similar to that of the undoped ZnO quantum dots, upon annealing the dots coarse with better crystallinity, as indicated by the more intense and narrower diffraction peaks. Again the average particle sizes can be estimated from the halfwidth of the diffraction peaks by applying

Scherrer formula. It turns out that the size of Mn doped quantum dots are somewhat bigger, varying from the as-grown 5 nm in diameter to 10 nm in the sample annealed at 500°C. The enlargement is to some extent perhaps due to the larger size of Mn than Zn.

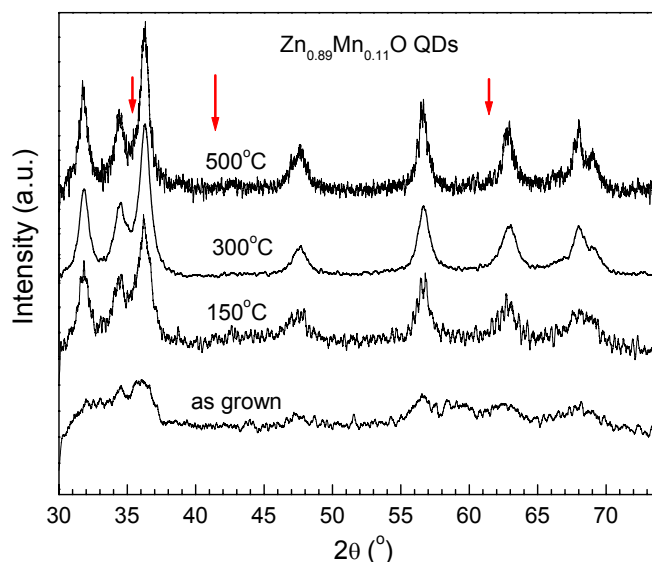


Figure 6.2 X-ray diffraction pattern of Zn_{0.89}Mn_{0.11}O as-grown quantum dots and dots annealed at 150°C, 300°C, and 500°C. The arrows show the positions of the three most intensive diffraction of MnO with the length indicating the relative intensity.

We have shown that undoped ZnO nanocrystals consist of ZnO/Zn(OH)₂ core-shell structure, and upon annealing the Zn(OH)₂ shell decreases due to thermal decomposition. Considering the same preparation procedure of both the doped and undoped samples, it is reasonable to assume that Zn_{1-x}Mn_xO quantum dots possess the same structure as their counterpart undoped ZnO quantum dots, i.e. the as-grown dots consist of a ZnO(:Mn)/Zn(OH)₂(:Mn) core-shell structure, and upon annealing the core grows and the shell disappears. However since at the moment we are uncertain where Mn is present, either in the core or in the shell, or both, we use the sign bracket to show the possible positions of Mn. The veil is to be discovered by the following EPR measurements.

6.3 EPR results of Mn in Zn_{1-x}Mn_xO quantum dots

6.3.1 EPR spectra of Mn in Zn_{1-x}Mn_xO quantum dots

Mn has been extensively studied as an impurity in solid hosts. The 2+ charge state Mn²⁺ ion has a half-filled *d* shell (3d⁵) in which the spins of all the electrons are aligned with spin

momentum $S = 5/2$ and angular $L = 0$, a state usually called S state or orbital singlet. Because of the relatively weak interaction of S state and the lattice, the spin-lattice relaxation time of S state will be comparatively long. Therefore the resonance of Mn^{2+} is easily observed even at RT. A distinct feature of Mn EPR is its hyperfine splitting arising from the central 100% abundant ^{55}Mn nucleus spin $I = 5/2$. The spin Hamiltonian for a Mn^{2+} ion in nanocrystals is given by

$$H = g\beta H \cdot S + \frac{1}{6}a(S_x^4 + S_y^4 + S_z^4) + D[S_z^2 - \frac{1}{3}S(S+1)] + AS \cdot I. \quad (6.1)$$

The first term describes the Zeeman interaction with g isotropic in the present case. The following terms describe the zero-magnetic-field of cubic symmetry and axial symmetries, respectively. The latter refers to the fine-structure splitting, which is nonzero only in environments with symmetries lower than cubic. The last term describes the hyperfine interaction between the d-electrons and the ^{55}Mn nucleus which results in a splitting into sextet lines due to the transitions at $\Delta M_I = 0$ and $\Delta m_S = \pm 1$.

In a magnetic field, the degeneracy of the spins of Mn^{2+} will be lifted up by the Zeeman splitting which will lead to five allowed transitions between $\pm \frac{5}{2} \leftrightarrow \pm \frac{3}{2}$, $\pm \frac{3}{2} \leftrightarrow \pm \frac{1}{2}$, and $+\frac{1}{2} \leftrightarrow -\frac{1}{2}$. Due to the hyperfine splitting each of the transitions will be splitted into six lines, and therefore thirty lines in all are expected to be observed. Such a nice complete spectrum was obtained by Dorain [13] in very slightly doped ZnO single crystal with Mn content to be approximately 0.1%. However, in a powder sample, the anisotropic contributions from the $\pm \frac{5}{2} \leftrightarrow \pm \frac{3}{2}$ and $\pm \frac{3}{2} \leftrightarrow \pm \frac{1}{2}$ transitions will shrink due to the random orientations, leaving mainly the contribution from $+\frac{1}{2} \leftrightarrow -\frac{1}{2}$ transition.

Figure 6.3 shows a representative room temperature EPR spectrum of Mn in ZnO quantum dots measured in wide magnetic field range. It is seen that the $+\frac{1}{2} \leftrightarrow -\frac{1}{2}$ transition in the field range $\sim 300-370$ mT is very strong. In the outer regime, some trace of weak signals are also observed though most of them are washed away by the random orientations of the quantum dots. The resonance positions are shown by the sign cross. These signals are from $-\frac{3}{2} \leftrightarrow -\frac{1}{2}$ and $\frac{3}{2} \leftrightarrow \frac{1}{2}$ transitions respectively. In the following we only show the $+\frac{1}{2} \leftrightarrow -\frac{1}{2}$ transition EPR signals.

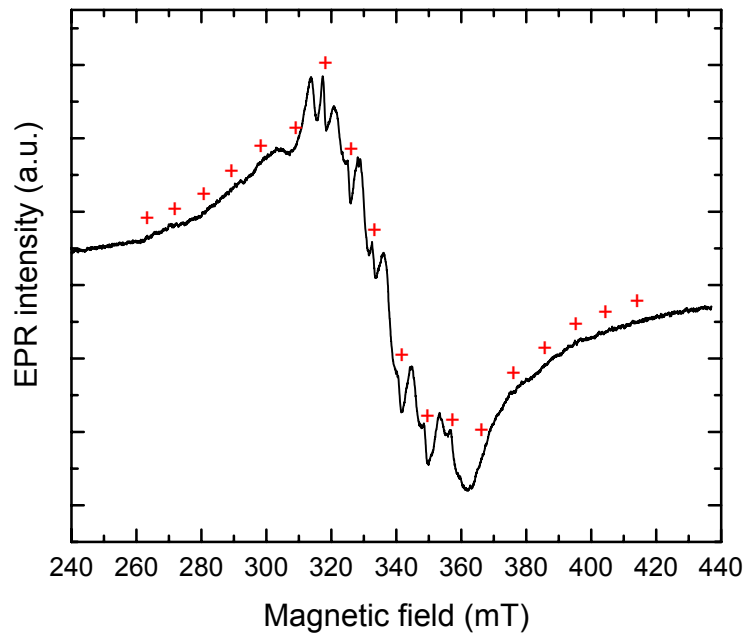


Figure 6.3 A representative room temperature EPR spectrum of Mn in ZnO quantum dots measured in wide magnetic field range. The sign cross shows the positions of the resonance.

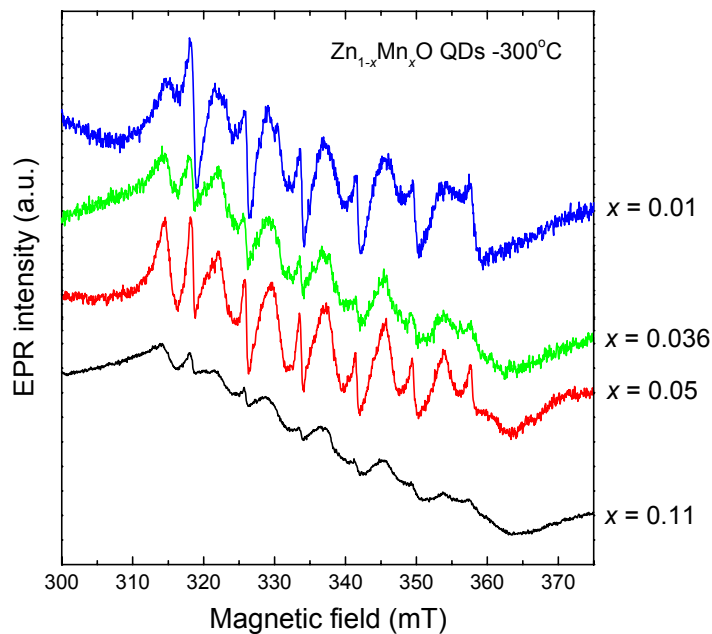


Figure 6.4 EPR spectra of $Zn_{1-x}Mn_xO$ quantum dots annealed at 300°C with different x .

For all the quantum dot samples the EPR signals are not saturated at RT at the maximum microwave power of 200 mW, and even not readily saturated at low temperature up to 20

mW. The EPR spectra that will be shown in the following were all measured at a moderate power of 2.0 mW. It was found that the spectra are nearly independent of the x in our experimental Mn concentration range, but rather changeable with different annealing treatment.

Figure 6.4 shows the EPR spectra of $\text{Zn}_{1-x}\text{Mn}_x\text{O}$ quantum dots annealed at 300°C with different x . The spectra look almost identical except that the spectrum of the most heavily doped sample with $x = 0.11$ is somewhat unstructured due to the strong background signal. As a candidate, the results of $\text{Zn}_{0.95}\text{Mn}_{0.05}\text{O}$ quantum dots are presented and discussed in detail.

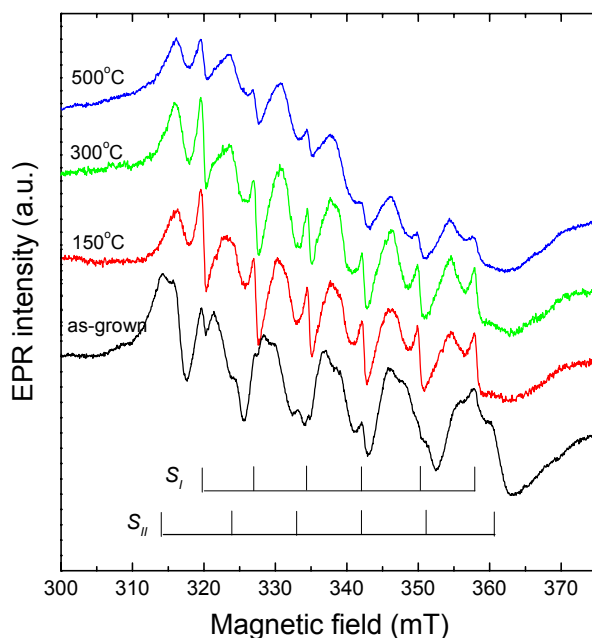


Figure 6.5 Room temperature EPR spectra of $\text{Zn}_{0.95}\text{Mn}_{0.05}\text{O}$ quantum dots annealed at different temperatures. Signal S_I is present in each spectrum while S_{II} only exists in the as-grown unannealed sample.

Figure 6.5 shows the room temperature EPR spectra of $\text{Zn}_{0.95}\text{Mn}_{0.05}\text{O}$ quantum dots annealed at different temperatures. It can be seen that the spectra of the annealed quantum dots are similar to each other, but different from that of the unannealed as-grown sample. Six sharp lines with 8.0 mT hyperfine splitting, labeled as S_I , superposed on a broad background are observed in the annealed samples. In between the six lines, there exists some broad structures, which we call asymmetry bands at the moment. With increasing annealing temperature, the background signal increases and the intensity ratio of the sextet lines to the asymmetry bands

decreases. The as-grown unannealed quantum dots, however, besides the S_I signal and the broad background, contain more structures as one can see from the new signals spreading over a wider field range. After careful comparison with the spectra of the annealed samples, another sextet signal is distinguished, labeled as S_{II} . It diminishes upon annealing and almost disappears at temperatures higher than 150°C.

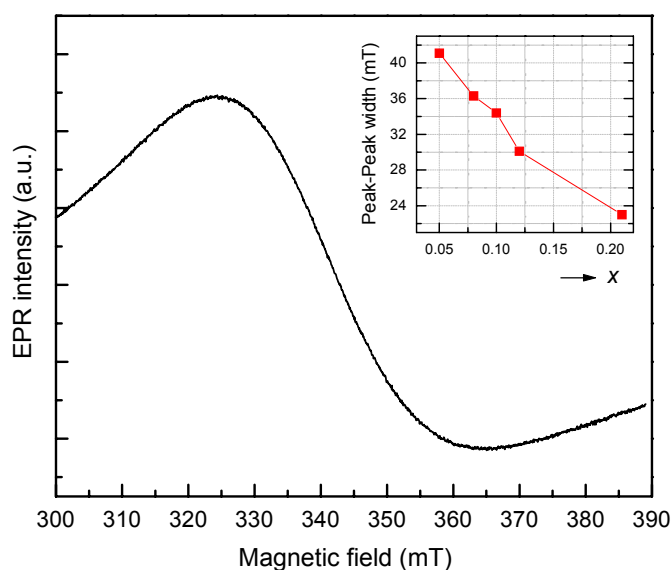


Figure 6.6 EPR spectrum of bulk $Zn_{1-x}Mn_xO$. The inset shows the dependence of peak-to-peak linewidth of bulk $Zn_{1-x}Mn_xO$ EPR spectra on x value.

For the bulk sample only a broad signal lack of the six-line structure resolution is observed, as shown in figure 6.6. This is typical for Mn clusters or dipole-dipole interactions between Mn impurities [15]. It indicates that Mn ions are not homogeneously dispersed in bulk $Zn_{1-x}Mn_xO$, and Mn-Mn clusters are easy to be formed. The peak-to-peak linewidth of the signal decreases from about 41 mT to 27 mT when x increases from 0.05 to 0.21, as shown in the inset. Such changes are not surprising. With increasing Mn content, Mn-Mn interaction become stronger due to shorter distance, therefore the signal becomes narrower.

The spectra of the quantum dots are nearly independent of temperature down to 10 K (except of becoming more intense). However when measured at 4.1 K, the S_I signal can be saturated, while signal S_{II} is not readily saturated (see figure 6.7).

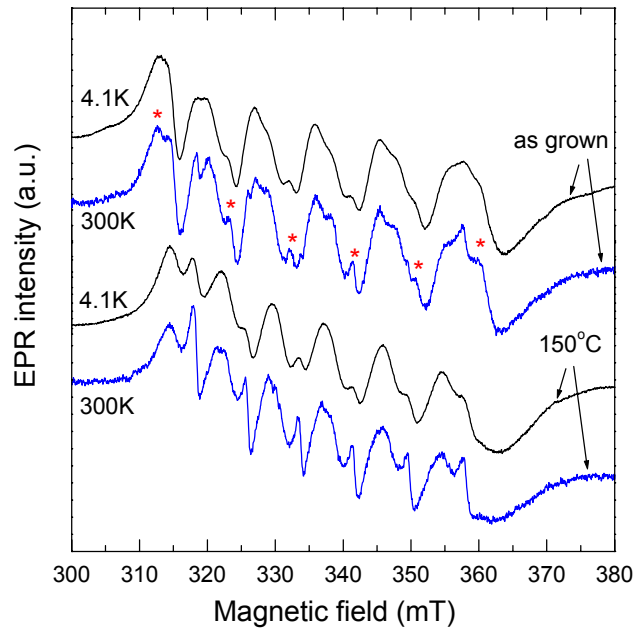


Figure 6.7 EPR spectra for as-grown and 150°C-annealed $\text{Zn}_{0.95}\text{Mn}_{0.05}\text{O}$ quantum dots taken at 4.1 K and at room temperature. In contrast to the not readily saturated signal S_{II} (indicated by the asterisks), signal S_I is of easy saturation.

6.3.2 Origins of the EPR signals

To understand the feature of each signal, we need separate them from each other. In principle, the deconvolution of the EPR spectra can be made using Bruker SIMFONIA and WINEPR software package, as being used for ZnS:Mn nanoparticles in Ref. [16]. However, the limitations of the software (e.g., lack of considering forbidden transitions) and the complexity of the spectra make such simulation complicated and difficult. Thinking that each spectrum may be composed of several common component signals which differs mainly in the relative intensity as might be changed by the annealing treatment or the measurement conditions, simple subtractions of the normalized data should allow to separate the spectra. This idea is to some extent comparable with that of Kennedy [17] for separating different signals from ZnS:Mn nanoparticles.

6.3.2.1 Origins of signal S_I and background signal

The analysis is shown in figure 6.8. The subtraction of the spectrum of 500°C annealed nanoparticles with that of the 150°C annealed gives immediately a well structured sextet signal imposed on a broad symmetry background, S_I and curve *a* (see bottom of fig. 6.8). The hyperfine splitting constant $|A|$ of S_I signal is $74.6 \times 10^{-4} \text{ cm}^{-1}$ (8.0 mT). The two weak peaks in between the hyperfine splitting lines are attributed to the forbidden transitions from $\Delta M_I = \pm 1$ and $\Delta m_s = \pm 1$ when the selection rule is relaxed in a hexagonal structure. The asymmetry bands in the original spectra are therefore now explainable and are indeed the overlap of these two forbidden transitions. A quite similar EPR signal without underlying broad background is also observed in extremely diluted Mn-doped CdS nanocrystals, as will be shown in chapter 7. *The S_I signal is therefore assigned to isolated Mn^{2+} ions substitutionally incorporated in wurtzite ZnO.*

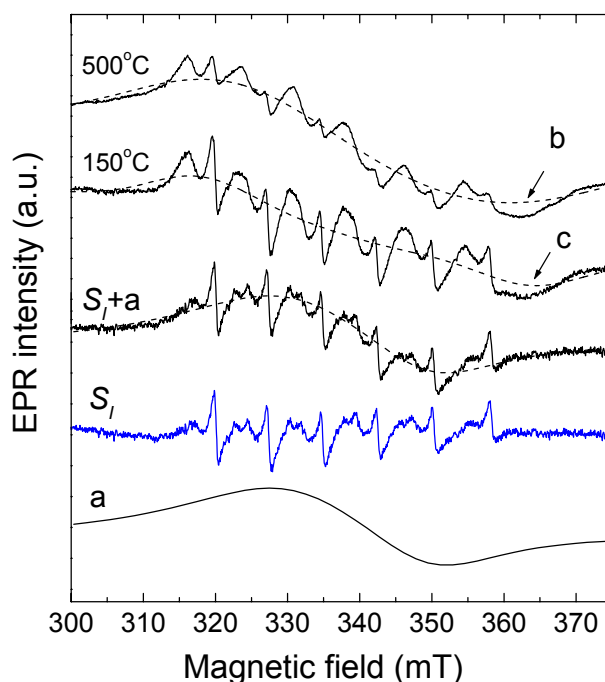


Figure 6.8 Separation of EPR spectra. S_I and curve *a* are obtained by subtract the EPR data of 500°C annealed $\text{Zn}_{1-x}\text{Mn}_x\text{O}$ nanoparticles with that of 150°C annealed. Curves *b* are *c* are obtained by first subtract the original EPR data with those of S_I and curve *a*, and then make Lorenz fitting.

The peak-to-peak width of curve *a* is about 24 mT, similar to that of the most heavily doped bulk sample ($x=0.21$). When we subtract S_I and curve *a* from the original data, we obtain an

even broader background, see curves *b* and *c* in the 500°C and 150°C annealed samples respectively. The peak-to-peak width is 42.8 mT for curve *b* and 48.1 mT for curve *c*. Compared with the dependence of the EPR signal width on the *x* value, as shown in the inset of fig. 6.6, it is clear that curve *a* with narrower width resembles the heavily Mn doped situation and is associated with shorter distant Mn ions or clusters. Vice versa, curves *b* and *c* with broader widths are associated with weaker Mn-Mn interaction, or longer distant Mn ions. In the case of quantum dots, the signal presented by curve *a* should most probably be originated from Mn clusters within one dot, i.e., the dots are doped with more than one Mn, while curves *b* and *c* present signals that are related to Mn clusters from different particles, which reflects the aggregation of the particles. The linewidth of curve *a* and curves (*b,c*) are comparable with those of the exchange coupled Mn clusters and Mn-Mn dipolar interactions observed in ZnS nanocrystal, respectively [16]. Therefore *the broad background signal is due to the Mn dipole-dipole interaction or Mn clusters*. Upon annealing, the dots grow on the consumption of more particles into one, therefore there are more Mn ions in one particle, which breaks S_I signal but rises the background. Similarly, the S_I signal loses the six-line structure when Mn content increases, as can be seen clearly in figure 6.4.

6.3.2.2 Origin of signal S_{II}

Due to the large surface of quantum dots, the origin of S_{II} might be roughly ascribed to Mn located in ZnO nanocrystal but near the surface, as in ZnS [16-18] or CdS [19, 20] nanocrystals. However, the assumption is unreasonable, since otherwise the signal will also appear in the annealed samples. The feature that signal S_{II} only shows up in the as-grown sample and quenches upon annealing give a strong indication that S_{II} should be attributed to Mn in the outer shell $Zn(OH)_2$, keeping in mind the existence of the surface $Zn(OH)_2$ shell in the undoped ZnO nanoparticles which disappears upon annealing.

To check whether it is really the case, we prepared Mn doped $Zn(OH)_2$ sample for comparison. Figure 6.9 shows the EPR spectra of 5% Mn doped as-grown ZnO quantum dots and $Zn(OH)_2$. A better resolved S_{II} signal is observed in the Mn doped $Zn(OH)_2$ sample, though there are still some traces of signal S_I . Therefore it is convincing that S_{II} is attributed to Mn in the outer shell $Zn(OH)_2$. Indeed the appearance of S_{II} in turn supports the correctness of our ZnO/ $Zn(OH)_2$ core-shell model.

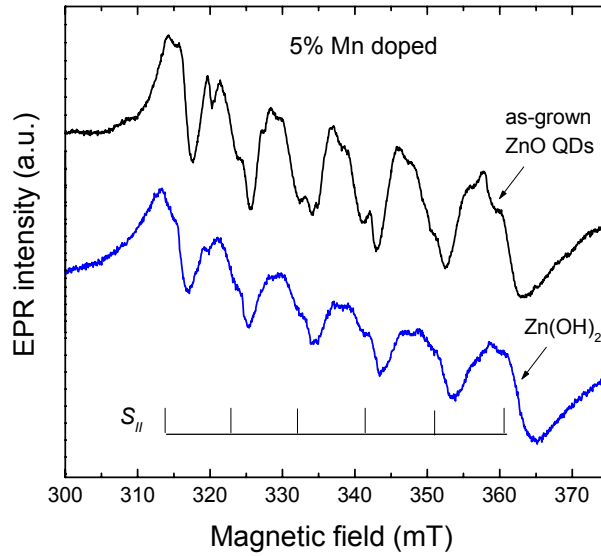


Figure 6.9 Comparison of EPR spectra of as-grown $\text{Zn}_{0.95}\text{Mn}_{0.05}\text{O}$ quantum dots and 5% Mn doped $\text{Zn}(\text{OH})_2$.

The g values and $|A|$ parameters of S_I and S_{II} , as also compared with those of Mn^{2+} in different materials, are shown in Table 6.2. The $|A|$ value of S_I is very close to that of diluted Mn-doped ZnO single crystal, while the g value is a bit larger. The g value is invariant with different quantum dots sizes, indicating a fail (or at least very poor) size confinement effect on Mn impurities. The similar $|A|$ value of S_{II} with that of Mn^{2+} in distorted sites near the surface of a nanocrystal or in disordered glasses further confirms that S_{II} is attributed to Mn in disordered environment ($\text{Zn}(\text{OH})_2$ in the present work). Compared with S_I , the relatively much larger $|A|$ value of signal S_{II} might be due to the less ionicity environment of $\text{Zn}(\text{OH})_2$.

Table 6.2 Electron paramagnetic resonance parameters of Mn^{2+} in different matrices.

host	symmetry	g value	$ A $ (10^{-4} cm^{-1})	Reference
ZnO (wurtzite)	hexagonal	2.0016	76.0	[13]
ZnO S_I (wurtzite)	hexagonal	2.0028	74.6	this work
ZnO S_{II}		2.0012	87.7	this work
ZnS S_{II}		2.001	89	[16]
ZnS NC2	axial	2.001	89	[17]
Borate glasses		2.0023	87	[21]

6.4 PL of $\text{Zn}_{1-x}\text{Mn}_x\text{O}$ quantum dots

The effect of Mn doping on the luminescence properties of $\text{Zn}_{0.95}\text{Mn}_{0.05}\text{O}$ quantum dots was investigated. Figure 6.10 shows the PL spectra of ZnO and $\text{Zn}_{0.95}\text{Mn}_{0.05}\text{O}$ quantum dots annealed at different temperatures. Compared with the undoped ZnO quantum dots, the introduction of Mn impurities leads to the slight redshift of the PL spectra, however the typical ${}^4\text{T}_1$ to ${}^6\text{A}_1$ transition of Mn, peaking at around 2.12 eV does not appear. The lack of Mn emission in ZnO is well established in the literatures [22, 23]. It has been argued that the absorption bands of Mn ions, which are located in the near ultraviolet, coincide with the continuous absorption of the lattice of ZnO. Therefore the energy transfer from the ZnO lattice to Mn is inefficient, and this may accounts for the absence of Mn luminescence.

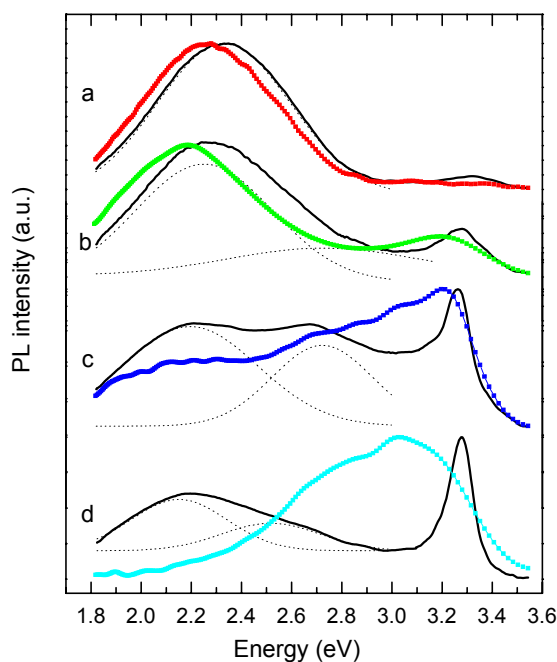


Figure 6.10 Room temperature PL spectra of ZnO (solid lines) and $\text{Zn}_{0.95}\text{Mn}_{0.05}\text{O}$ (lines with signs) quantum dots annealed at different temperatures: unannealed (a); annealed at 150°C (b); 300°C (c); 500°C (d). The dotted lines are the fitted Gaussian bands of undoped ZnO quantum dots.

In summary, our EPR results show that there are three distinct Mn locations in ZnO quantum dots. Mn ions at substitutional Zn sites in hexagonal ZnO have a g value equal to 2.0028 with a $74.6 \times 10^{-4} \text{ cm}^{-1}$ (8.0 mT) hyperfine interaction. The 2.0012 g -value and $87.7 \times 10^{-4} \text{ cm}^{-1}$ (9.4 mT) is related to Mn in the surface amorphous $\text{Zn}(\text{OH})_2$ shell. The third one is correlated to interacting Mn centers (dipole-dipole interaction) or Mn clusters.

Chapter 7 Characterization of (Cd, Mn)S quantum dots

7.1 Background knowledge

Despite of the extensively study on bulk $A^{II}MnB^{VI}$ chalcogenide diluted magnetic semiconductors (DMS) [1, 2], the research of Mn doped II-VI chalcogenide quantum dots received a bloom in the 1990's since the initial publication on the influence of quantum size effects on the luminescence of Mn^{2+} in ZnS nanocrystals by Bhargava *et al* [3, 4]. They reported for the first time that doped semiconductor nanocrystals can yield both high luminescence efficiencies and five orders of magnitude lifetime shortening (from ms as in the bulk material to ns) at the same time. These spectacular results suggested that doped semiconductor nanocrystals may form a new class of luminescent materials, with a wide range of application in, e.g., displays, sensors, and lasers. The short decay time, is especially important for applications in which saturation effects limit the light output of a luminescent material.

To account for the phenomena, Bhargava [3] suggested that with decreasing particle size a strong hybridization of the s-p states of the ZnS host and the d states of the Mn^{2+} impurity should occur. This hybridization results in a faster energy transfer between the ZnS host and Mn^{2+} impurity. Due to this fast energy transfer, the radiative recombination at the Mn^{2+} impurity, which competes with nonradiative decay at the ZnS surface, becomes more efficient. This results in an increase of quantum efficiency. Also, it was argued that through this hybridization the spin forbidden transition of the Mn^{2+} impurity becomes less spin forbidden, resulting in a shorter decay time.

The exciting results stimulated tremendous research work from different groups on the luminescence of various doped nanocrystals [5-11]. In recent textbooks in the field of luminescence spectroscopy the results were even discussed as being one of the most important discoveries in the field in the decade [12, 13].

However the work was severely questioned by many other groups represented by Bol and Meijerink [10]. First of all, they argued that a shift of the position of the Mn^{2+} emission band due to stronger hybridization of the s-p states of the ZnS and d states of the Mn^{2+} should be observed if it is the case. However, this was not observed. Second, the lifetime shortening of the Mn^{2+} emission due to quantum confinement effect reported by other groups do not coincide with each other even for the similar nanocrystal size. For example, Sooklal *et al* [7]

observed ns decay times in ZnS:Mn nanocrystals, while Ito *et al* [9] reported lifetime shortening to μs in ZnTe:Mn. Furthermore, all the publications do not describe experiments to verify the absence of a ms decay time in ZnS:Mn nanocrystals. From careful lifetime measurements and time resolved spectroscopy Bol and Meijerink found that the Mn^{2+} emission in ZnS nanocrystals does not show a spectacular shortening of the decay time upon decreasing particle size, but has a normal decay time of about 1.9 ms, like that in bulk ZnS. The nanosecond decay time reported for the Mn^{2+} emission is due to the tail of broad defect-related ZnS emission which overlaps with the Mn^{2+} emission at around 590 nm. Therefore they concluded that doped semiconductor nanocrystals do not form the new class of luminescent materials. Nearly the same radiative lifetime (1.7 ms) of the Mn^{2+} emission in CdS nanocrystals as in the bulk was observed [11]. A comparison of the energy level of Mn^{2+} in bulk and nanosized- ZnS showed the degree of the mixing between the s-p state of ZnS and the 3d state of Mn^{2+} does not change significantly with the reduction of the crystal size down to a few nanometers [14]. The assumption of the strong sp-d mixing in the nanocrystals as proposed by Bharvaga is therefore strongly doubted.

To understand the underlying physics of the Mn^{2+} emission in II-VI nanocrystals, the atomic structure and local symmetry of Mn have been studied by EPR [15-19] and EXAFS (extended x-ray absorption fine structure) [20, 21] measurements. However, though different Mn hyperfine interactions have been found, the assignment to different Mn locations lacks of confirmation, and the discussions of the correlation of Mn emission to the local structure is controversial (see below).

Since most of the above work is based on a few and different samples, a systematic study on more samples is therefore needed. Due to the virtue of comprehensive self-prepared samples with different size and doping concentrations, we are able to present a better understanding of the (Cd, Mn)S quantum dots. In this chapter we explore the local structure of Mn^{2+} in CdS quantum dots by EPR studies, and investigate the correlation of the luminescence properties with the Mn^{2+} local structure.

7.2 Optical absorption and luminescence properties

In the available Mn concentration range, from 0.01 to 0.23 in the present work, XRD shows only sphalerite CdS phase. From the phase diagram of CdS-MnS we know that, the solubility of Mn in CdS is rather high, up to 45% [22]. It is interesting to note that the CdS nanocrystals

synthesized using wet chemistry methods are always cubic zincblende structure, as also for ZnS nanocrystals [23, 24], though the most common form for the bulk is the hexagonal wurtzite structure.

Figure 7.1 shows optical absorption of fresh undoped CdS quantum dots with different water/AOT ratio, w . The position of the absorption peak blueshifts from 2.88 eV for $w = 10$ to 3.54 eV for $w = 2.5$. Compared with the bandgap of bulk CdS (2.5 eV, as indicated by the arrow), the bandgaps of the nanocrystals are greatly enlarged, as a consequence of quantum size effect. With increasing water/AOT ratio, the absorption peak become wider, indicating a broader size distribution of CdS quantum dots. From the dependence of the bandgap on the size (see the inset), given by effective mass approximation, we obtain 2.7 nm, 2.9 nm, 3.5 nm, and 4.2 nm for the bandgap at 3.54 eV, 3.44 eV, 3.11 eV and 2.88 eV, respectively. Therefore the particle size can be carefully controlled by varying the water/AOT ratio, which turns out to be a suitable parameter to prepare nanocrystals of various sizes. The Bohr radius a_B of CdS is 3.0 nm, calculated from Eq. (3.5) with $m_e / m_o = 0.19$, $m_h / m_o = 0.53$, and $\epsilon = 5.5$. The synthesized CdS nanocrystals are even smaller than the Bohr radius, and this is the reason why the quantum size effect is so pronounced.

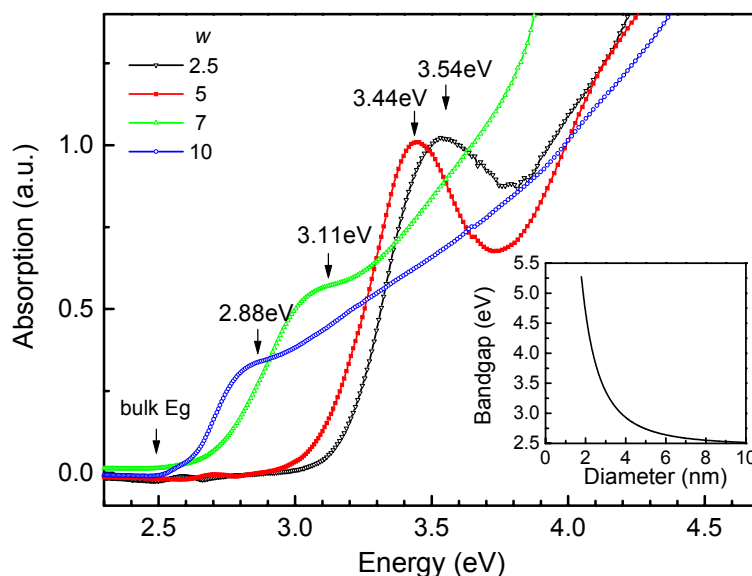


Figure 7.1 Optical absorption of fresh undoped CdS quantum dots with different water/AOT ratio, w . The arrow shows the position of bandgap of bulk CdS. The inset shows the dependence of bandgap of CdS quantum dots on the size.

When doped with Mn, the bandgap shifts. Figure 7.2 shows the shift of the bandgap of 2.9 nm ($w=5$) CdS quantum dots with different doping concentration x . With increasing x , the

absorption peak shifts to lower energy and becomes broader. The change of the bandgap is in accordance with the observation that the bandgap of bulk $\text{Cd}_{1-x}\text{Mn}_x\text{S}$ does not vary monotonously, but decreases at low Mn concentrations ($x < 0.1$) and then increases [25]. Broadening of the absorption lines with increasing x can partly be attributed to local energy fluctuation due to fluctuation of the Mn concentration.

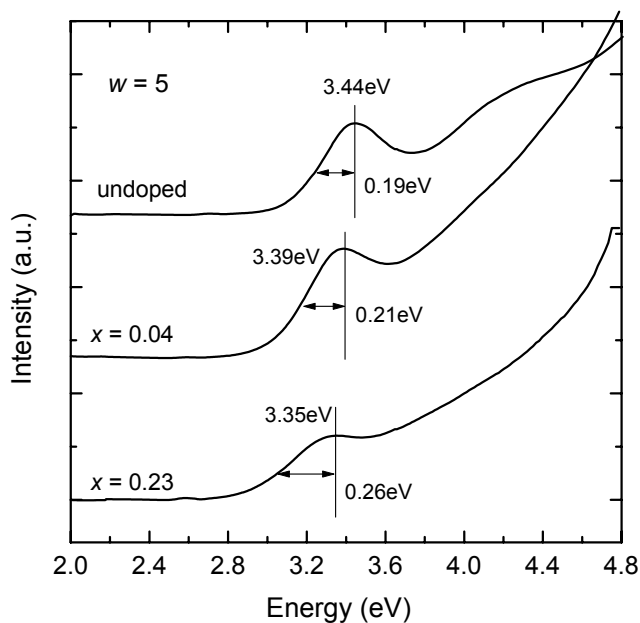


Figure 7.2 The shift of bandgap of CdS nanocrystals with different doping concentration x . The arrows show the corresponding half-widths of the absorption peaks.

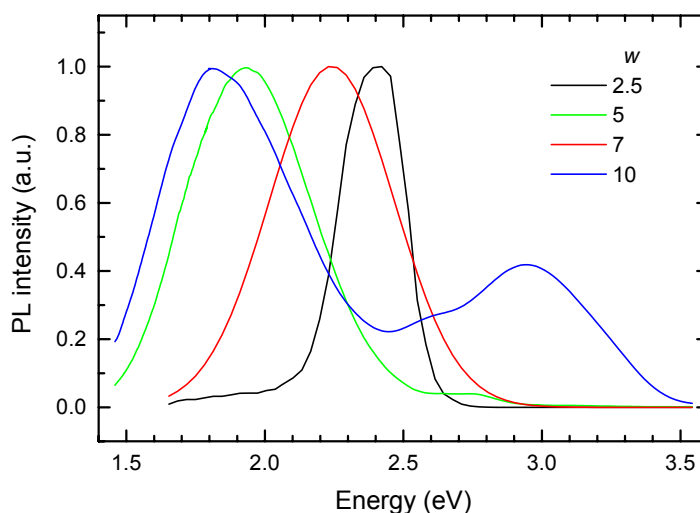


Figure 7.3 PL spectra of undoped CdS quantum dots with different water/AOT ratio, w .

Photoluminescence spectra of undoped CdS quantum dots with different water/AOT ratio are shown in Figure 7.3. We note that all luminescence spectra are Stokes-shifted from the absorption spectra, and there is almost no band-edge luminescence except the dots with the biggest size, indicating the luminescence are defect related. As the sizes of the dots decrease the luminescence peak moves to higher energy, showing size dependent luminescence properties. For the larger dots, the luminescence peak is located at ~ 1.81 eV. This luminescence band is commonly observed for CdS nanocrystals [26], and is usually attributed to sulfur anion vacancies, though the origin is not yet clear.

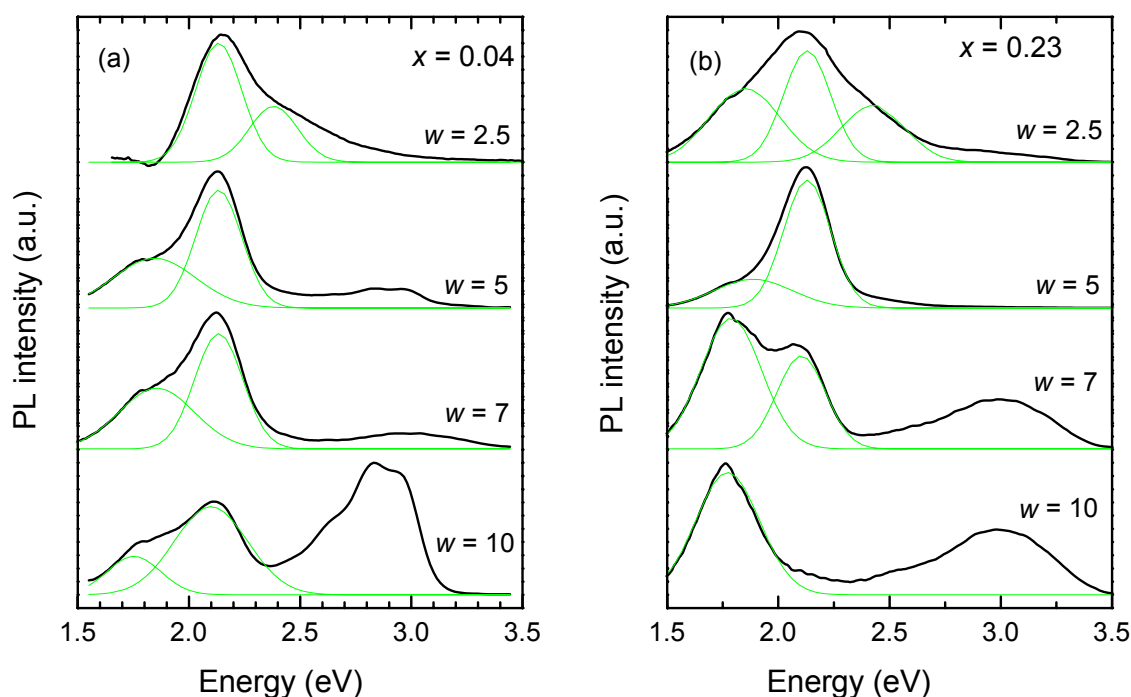


Figure 7.4 PL spectra of lightly (a) and heavily (b) doped CdS quantum dots with different water/AOT ratio, w .

Figure 7.4 shows the normalized PL spectra of Mn doped CdS quantum dots. For lightly doped samples (fig. 7.4 (a)), the spectra are dominated by the characteristic of Mn^{2+} internal ${}^4\text{T}_1$ to ${}^6\text{A}_1$ transition, a yellow band peaking at 2.12 eV. The defects related broad signals are superimposed and show up as weak bands. The real intensity of Mn luminescence decreases with increasing w , i.e., bigger particle size. The tail in high energy region is due to the near bandgap emission which is weak in smaller dots, and become so strong that it exceeds the Mn emission and can be observed by naked eyes in bigger dots. When heavily doped, Mn

luminescence bands further decrease, see fig. 7.4 (b). Mn luminescence dominates in comparatively smaller dots ($w = 2.5, 5$), however the signal lose its dominance in the dots with $w = 7$, and completely disappear in dots with $w = 10$.

7.3 EPR spectra of $\text{Cd}_{1-x}\text{Mn}_x\text{S}$ quantum dots

The change of PL spectra with Mn concentration and the dot size reflects change of Mn structures in the quantum dots. Figure 7.5 (a) and (b) show EPR spectra of the corresponding lightly and heavily doped nanocrystals of fig. 7.4, respectively. In figure 7.5 (a), the sample with the smallest size shows a well defined six lines with $g = 2.0025$ and hyperfine interaction constant $|A| = 64.4 \times 10^{-4} \text{ cm}^{-1}$ (6.9 mT), labeled as S_I , superimposed on a weak broad background. With increasing particle size, the background signal increases, and another sextet-line signal, S_{II} , with $g = 2.0014$ and $|A| = 74.6 \times 10^{-4} \text{ cm}^{-1}$ (8.0 mT) appears. For heavily doped (fig. 7.5 (b)), we can mainly see an overall strong background with a weak, however discernable S_{II} . Signal S_I , though could hardly be seen, exists as one can see the very small structures.

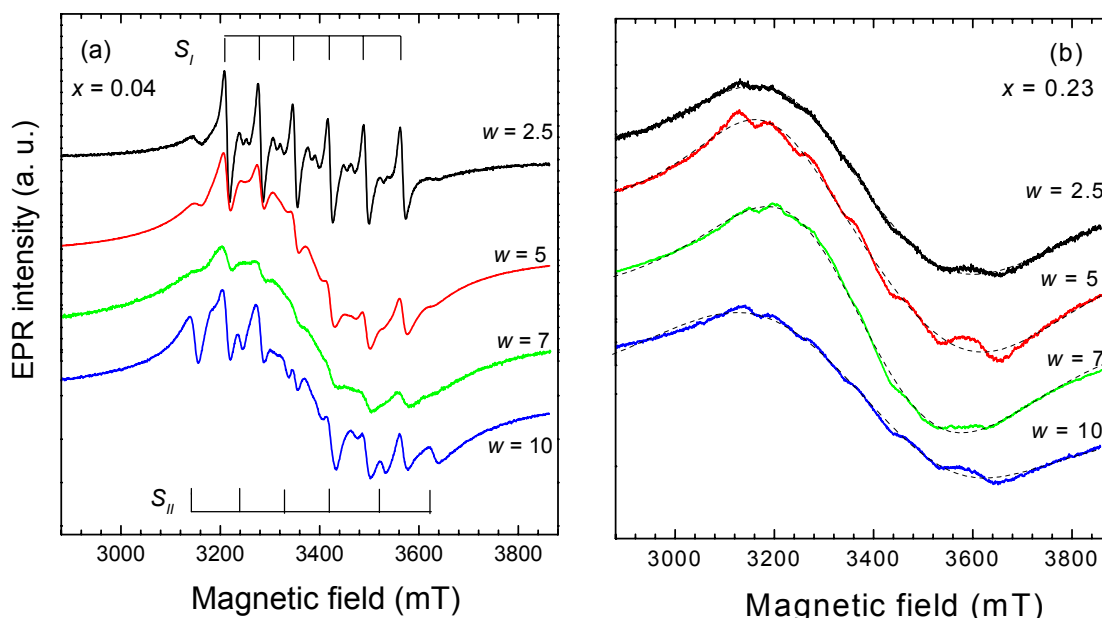


Figure 7.5 EPR spectra of the corresponding lightly (a) and heavily (b) doped nanocrystals in fig. 7.4.

Like S_I and S_{II} , two distinct EPR spectra with different g and $|A|$ values have been widely observed for Mn^{2+} in CdS and ZnS nanocrystals. Parameters are given in Table 7.1. The g and

$|A|$ values of S_I are very close to those of diluted Mn-doped CdS single crystal, and thus is attributed to Mn in substitutional Cd sites. However, the assignment of S_{II} to Mn^{2+} in distorted sites (i.e., near the surface of nanocrystals) is mostly based on deduction without experiment identification.

Table 7.1 Electron paramagnetic resonance parameters of Mn^{2+} in CdS and ZnS.

Host *	Symmetry **	g value	$ A $ (10^{-4} cm $^{-1}$)	Reference
CdS (bulk)	hexagonal (T_d)	2.0029	65.3	[27]
CdS	cubic (T_d)		64.5	[18]
CdS	cubic (O_h)		90	[18]
CdS S_I	cubic	2.0025	64.5	this work
CdS S_{II}		2.0013	89	this work
ZnS signal I	cubic (T_d)	2.0024	64.5	[16]
ZnS signal II	cubic (T_d)	2.0013	84	[16]
ZnS S_I	cubic (T_d)	2.001	63.9	[17]
ZnS S_{II}	cubic (O_h)	2.001	90	[17]
ZnS NC1	cubic (T_d)	2.003	64.5	[15]
ZnS NC2	axial	2.001	89	[15]

* If not noted all are nanocrystals. ** T_d , tetrahedral sites; O_h , octahedral sites.

Furthermore, the arguments on the contribution of S_I and S_{II} to Mn luminescence are controversial. While Borse [17] suggests only S_I may be responsible for Mn emission, and S_{II} results in quenching, Kennedy [15] and Gounio [18] argue S_{II} contribute to the luminescence. Compare Fig. 7.4 with Fig. 7.5, it seems that only S_I contributes to the emission, while S_{II} and the background signal quench Mn emission. In the following, the origins of S_I and S_{II} and their luminescence properties are to be clarified.

7.4 Correlation of Mn local structures and their luminescence

7.4.1 Origin of signal S_I

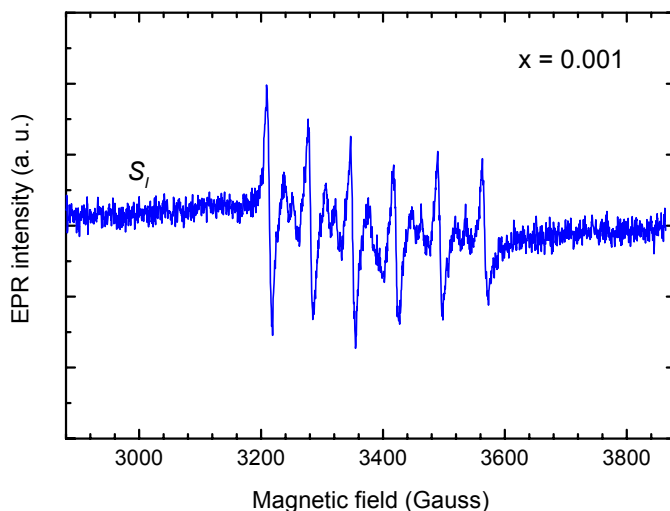


Figure 7.6 EPR spectrum of extremely lightly doped CdS:Mn with Mn concentration 0.001.

To avoid the effect of the background signal, which come from the Mn clustering or dipole interaction due to high Mn concentration, we prepared an extremely lightly doped sample for EPR measurement. The doping concentration is so low that it can not be determined by EDX, however from the preparation it is estimated to be about $x = 0.001$. A well structured signal S_I without any background signal is obtained (see figure 7.6). Therefore it is clear that S_I is from isolated Mn substitute Cd sites in cubic CdS quantum dots.

7.4.2 Origin of signal S_{II}

To investigate whether S_{II} is related to Mn on the surface, we doped the nanocrystals in two different ways: one is the commonly used method as described in chapter 2, i.e., first prepare Cd^{2+} and Mn^{2+} microemulsion, and then mix with the other part contains S^{2-} , this process is indicated by Cd+Mn+S; the other is Cd+S+Mn process, i.e., first prepare CdS microemulsion by mixing Cd^{2+} and S^{2-} , and then dope the dots with Mn^{2+} . We expect that in the latter process Mn will mainly be located on the surface. To decrease the diffusion of Mn from the surface to the core, PL spectra were soon measured after the mixing. Figure 7.7 (a) shows the EPR spectra of dots prepared the two different processes. For the Cd+Mn+S process, S_I dominates though the signal S_{II} can be also seen. However for the Cd+S+Mn process, S_I is strongly

suppressed, and S_{II} dominates. Therefore we are convinced that S_{II} is from Mn located at the surface.

7.4.3 Contributions of S_I and S_{II} to Mn luminescence

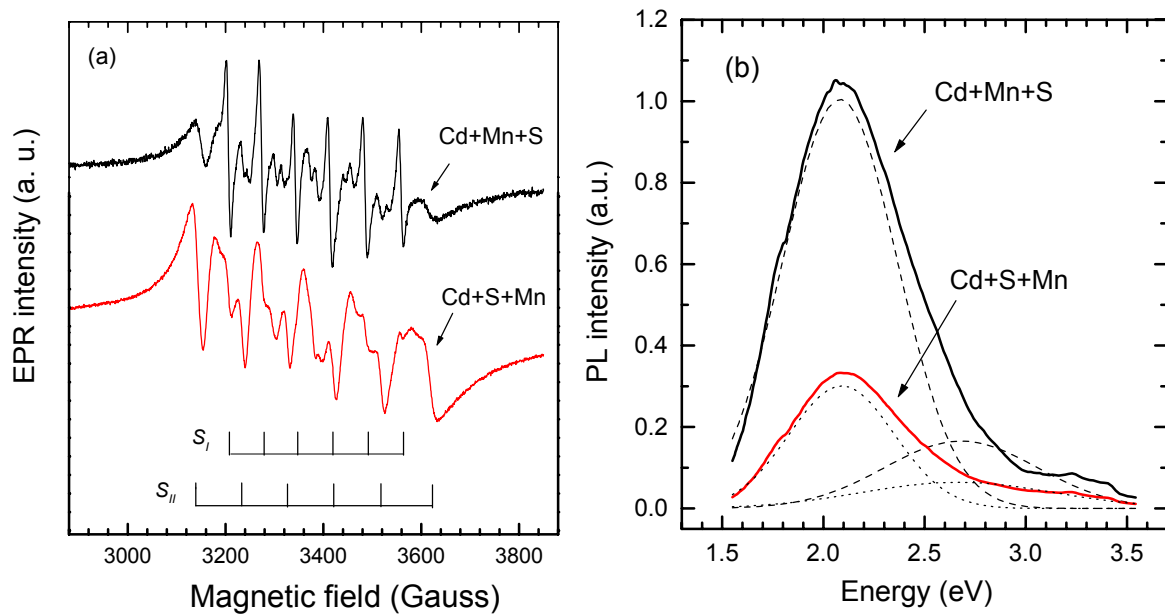


Figure 7.7 EPR (a) and PL (b) spectra of $\text{Cd}_{0.96}\text{Mn}_{0.04}\text{S}$ nanocrystal prepared via Cd+S+Mn and Cd+Mn+S processes.

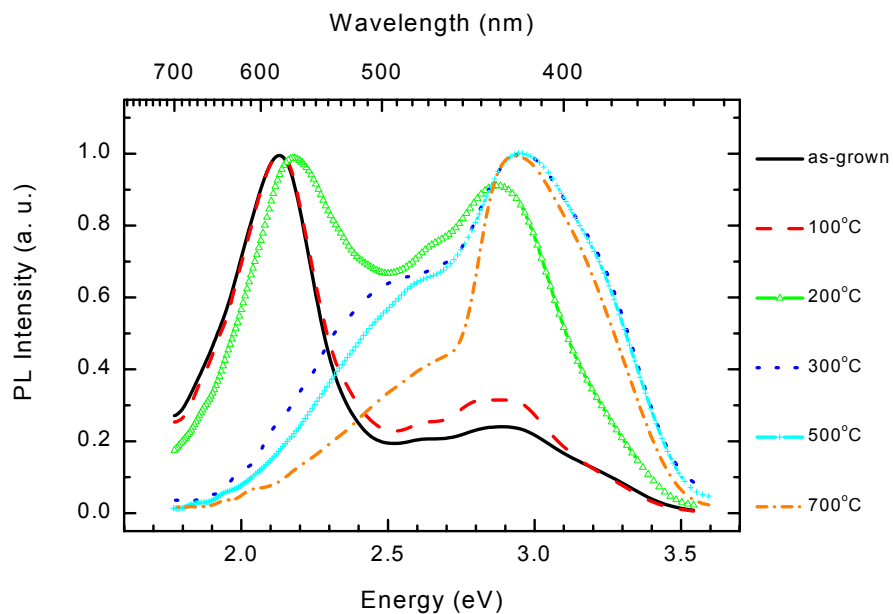


Figure 7.8 PL spectra of $\text{Cd}_{0.96}\text{Mn}_{0.04}\text{S}$ nanocrystal annealed at different temperatures.

Figure 7.7 (b) shows the corresponding PL spectra of the two processes. The dramatic decrease of Mn luminescence by S_{II} (process Cd+S+Mn) immediately demonstrates that when Mn is present at the surface (S_{II}), the Mn luminescence quenches.

The conclusion that S_{II} quenches the Mn emission is further confirmed by an annealing study, see figure 7.8. When annealed, the Mn luminescence band sharply decreases at temperatures higher than 200°C. Corresponding EPR spectra show a great decrease of S_I and increase of S_{II} and background signal. It indicates that Mn ions located in the core have lower energy state, while higher energy state when located on the surface. This may account for the appearance of S_{II} in ZnS nanocrystals upon aging [15].

7.4.4 Evolution of S_I and S_{II}

Obviously there is an evolution from S_I to S_{II} with increasing dot size and Mn concentration (look back fig. 7.5). For a quantitative analysis, we need to know how many Mn ions are in each dot with different average size. This can be obtained with a simple calculation. For simplicity, we assume each nanocrystal is spherical in shape, and the cell volume of nanocrystals is identical with the value of the bulk case. The primitive cell volume of sphalerite CdS, V_c , is $198.46 \times 10^{-3} \text{ nm}^3$. Therefore we have

$$\frac{4}{3}\pi R^3 = n \cdot V_c, \text{ i.e. } \frac{\pi}{6} D^3 = n \cdot V_c \quad (7.1)$$

where R and D are the radius and diameter of the nanocrystals, and n the cell number that each dots possess. The number of Mn, n_{Mn} , is therefore

$$n_{Mn} = x \cdot n = \frac{\pi}{6V_c} \cdot D^3 \cdot x = 2.636D^3 \cdot x \quad (7.2)$$

with x is the concentration of Mn. The number of Mn is proportional to concentration (x) and the cube of diameter (D). The bigger D , and the higher x , the larger n_{Mn} . Supposing the Mn ions are homogeneously dispersed in the dots, the longest distance between two neighbor Mn ions within one dot \bar{d} is $\bar{d} = D \sin(\pi / n_{Mn})$.

Table 7.2 shows the number of Mn in each dot (n_{Mn}) and the distance between two neighboring Mn ions (\bar{d}) with different dot size and Mn concentration. For lightly doped sample, the smallest dots have average 2 Mn ions per dot with 2.7 nm distance, a distance four times larger than the lattice parameter $a_0 = 0.583 \text{ nm}$. Therefore the Mn dipole interaction

is rather weak, and this may account for the well resolved EPR signal (fig. 7.5 (a)). With increasing dot size, more Mn is present within one dot while being closer, resulting in stronger Mn-Mn interactions (background), and diffusion to the surface (S_{II}). When heavily doped, there are so many Mn within one dot that the distance is even smaller than the lattice distance a_0 , indicating formation of Mn clusters. As a consequence mainly the broad background can be seen.

Table 7.2 Number of Mn in each dot (n_{Mn}) and the distance between two neighbor Mn ions (\bar{d}) with different dot size and concentration.

w	Diameter (nm)	n_{Mn} ($x=0.04$)	n_{Mn} ($x=0.23$)	\bar{d} (nm) ($x=0.04$)	\bar{d} (nm) ($x=0.23$)
2.5	2.7	2.07	11.93	2.7	0.69
5	2.9	2.56	14.78	2.51	0.71
7	3.5	4.52	25.99	2.45	0.43
10	4.2	7.81	44.85	1.61	0.29

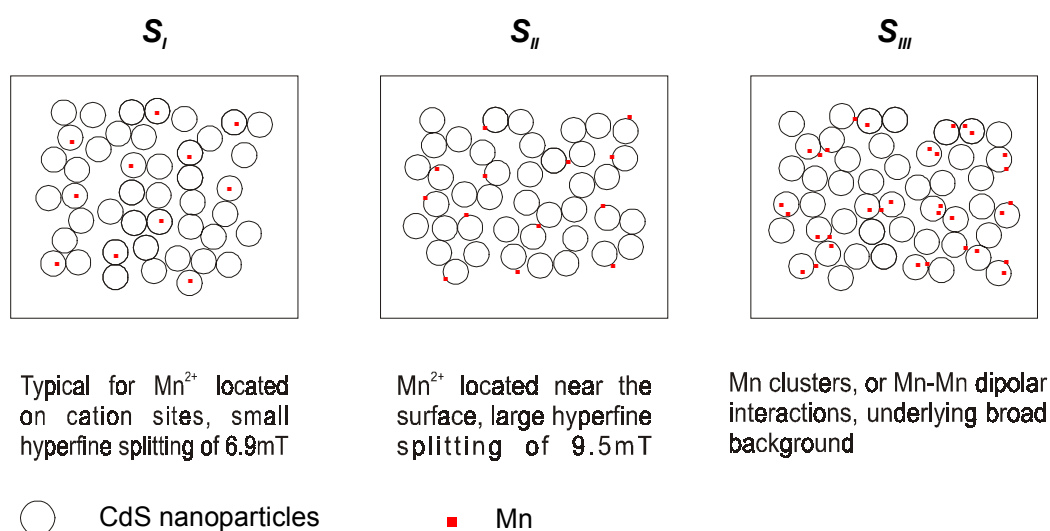


Figure 7.9 Schemes of different locations of Mn ions in CdS nanocrystals. S_I is related to Mn^{2+} located substitutionally on Cd sites; S_{II} to Mn^{2+} located near the surface; and S_{III} to Mn clusters or Mn-Mn pairs.

Schemes of different Mn locations in CdS quantum dots are shown in figure 7.9. S_I is related to Mn^{2+} located substitutionally on Cd sites; S_{II} to Mn^{2+} located near (or at) the surface; and S_{III} to Mn clusters or Mn-Mn pairs.

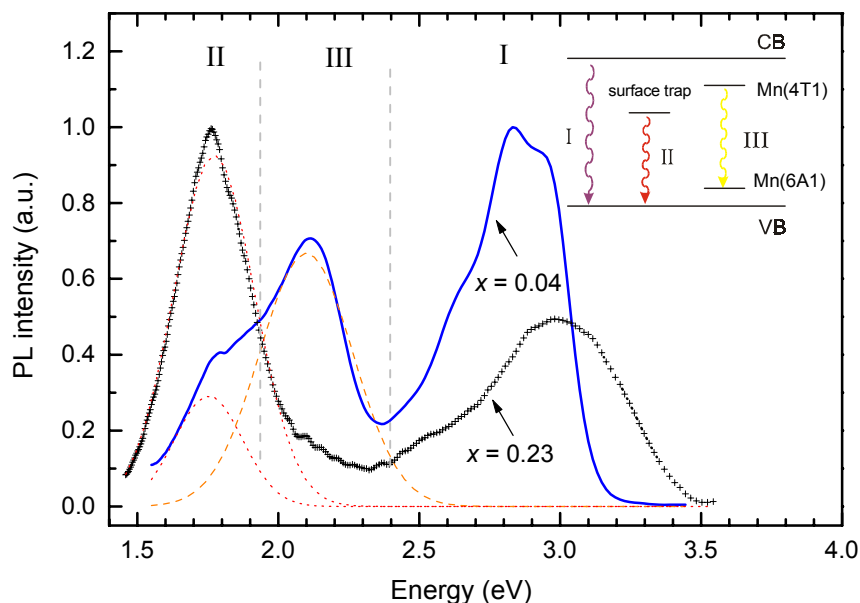


Figure 7.10 PL spectra of lightly ($x=0.04$) and heavily ($x=0.23$) Mn doped CdS quantum dots. The inset shows radiative recombination processes. Process I is bandgap emission; process II emission from surface traps; and process III $Mn\ ^4T_1$ to 6A_1 emission.

To summarize the results of this section, the PL spectra of lightly ($x=0.04$) and heavily ($x=0.23$) Mn doped CdS quantum dots are reproduced in figure 7.10. The luminescence concludes three recombination processes, as schematically depicted in the inset. While the bandgap (process I) and surface (process II) emissions are observed for both the lightly and heavily doped samples, the 4T_1 to 6A_1 emission of Mn ions (process III) is strongly correlated to their concentration, i.e. Mn local structures. Only when Mn is located in the dots, substitutionally on Cd sites, the emission can be observed.

7.5 A glance at the Mn emission life time

By changing the frequency of the chopper, we were capable of a “time resolved” PL measurement. The faster the frequency, the shorter decay time can be detected, and vice versa. With the slow frequency, the Mn luminescence shows up already, and when measured with

the fast time, a band at around 2.39 eV (see the dashed curve) appears, see figure 7.11. From fig. 7.3 we know this luminescence band is related to the trapping of CdS quantum dot itself. Due to the limit of the chopper frequency of our setup (10000Hz), the fastest decay can be detected is 0.1 ms. It is clear that Mn luminescence in nanocrystals is a normal slow one of the order of ms.

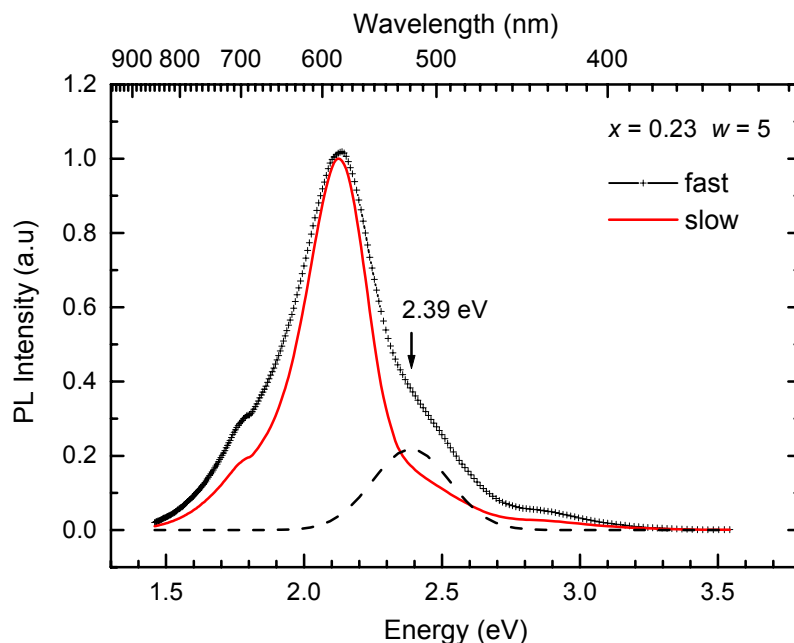


Figure 7.11 Time resolved PL spectra of $\text{Cd}_{0.96}\text{Mn}_{0.04}\text{S}$ nanocrystal.

7.6 Summary

The structure and luminescence properties of Mn^{2+} in CdS quantum dots are presented in this chapter. Our EPR results show that there are three distinct Mn locations in CdS quantum dots. Signal S_I is related to Mn ions at substitutional Zn sites in cubic CdS have a g value equal to 2.0025 with a $64.6 \times 10^{-4} \text{ cm}^{-1}$ (6.9 mT) hyperfine interaction. Signal S_{II} with $g = 2.0013$ and hyperfine splitting $89 \times 10^{-4} \text{ cm}^{-1}$ (9.5 mT) is related to Mn on the surface of the quantum dots. The broad background is correlated to the Mn dipole-dipole interaction or Mn clusters. Combined with the luminescence studies, we provide strong evidence that only the Mn ions located in the core of the dots are responsible for the ${}^4\text{T}_1$ to ${}^6\text{A}_1$ emission, which has a normal slow life time (ms).

Chapter 8 Summary

This dissertation deals with the structure and physical properties of undoped and Mn-doped ZnO, and Mn-doped CdS quantum dots, prepared by wet chemistry methods.

The interest in ZnO arises from its promising future for room temperature UV laser due to the wide bandgap (3.37 eV) and large exciton binding energy (60 meV). However the UV emission of ZnO quantum dots commonly reported is rather weak, which greatly limits the applications as nano-UV laser. The first endeavor of the thesis is to investigate the structural origin behind the weak excitonic recombination. The investigation of the effect of different annealing and aging (exposure to air) processing conditions on the luminescence properties of ZnO quantum dots reveals that, the surface of ZnO quantum dots is very sensitive and hospitable to H₂O environment to form an amorphous Zn(OH)₂ shell, and therefore the as-grown dots consist of a ZnO/Zn(OH)₂ core-shell structure. When Zn(OH)₂ is present, the excitonic transition of ZnO quantum dots is quenched. This is the main reason behind the weak UV emission of ZnO quantum dots where the surface is capped by Zn(OH)₂. Strong UV emission is obtained for dots annealed at high temperatures (> 300°C), when the outer shell of Zn(OH)₂ is released. Aging leads to decay of the UV emission, due to the re-generation of the surface Zn(OH)₂ shell. To put it in a nutshell, the UV emission exhibits an on/off “switch” feature upon annealing and aging treatments.

The core-shell model is further confirmed by EPR studies, which aim to explore the local structure of magnetic centers (i.e. Mn²⁺) in ZnO quantum dots. Three distinct different Mn centers could be distinguished. Mn ions at substitutional Zn sites in the core of hexagonal ZnO have a six-line resonance spectrum with g-value equal to 2.0028 and a hyperfine interaction of $74.6 \times 10^{-4} \text{ cm}^{-1}$ (8.0 mT). The sextet-line resonance of Mn located in Zn(OH)₂ surface shell is also observed, and has a g-value of 2.0012 and hyperfine constant of $87.7 \times 10^{-4} \text{ cm}^{-1}$ (9.4 mT). The related signal has the maximum intensity for the as-grown quantum dots, and rapidly decreases upon annealing. The resonance spectra of these two centers are called S_I and S_{II} , respectively. The third is correlated to the Mn dipole-dipole interaction or Mn clusters, which gives a structureless broad background signal. Similar EPR signals are also present in Mn doped CdS quantum dots. While the hyperfine constant of S_I is $64.5 \times 10^{-4} \text{ cm}^{-1}$ (6.9 mT), somewhat smaller than that in ZnO, S_{II} is essentially the same.

Comparing our EPR results of Mn in ZnO and CdS nanocrystals with the results in other II-VI nanocrystals, e.g. ZnS, we find that, despite the difference in preparation methods, the observations are quite similar. Typically, in all the compounds the three types of Mn related spectra are observed. The S_I signal is most likely related to nanocrystals with one Mn ion in the core. The appearance of the S_{II} signal seems to be general for Mn doped colloidal II-VI nanocrystals studied so far, independent of whether they are sulfur- or oxygen based. Our studies provide strong evidence that this spectrum arises from Mn^{2+} located in the outer shell covering the nanocrystal core. Such outer shell is natural for ZnO, but may also be formed upon aging in the other systems. This explains the appearance of S_{II} signal upon exposing Mn doped ZnS nanocrystal to air, and the drastic reduction upon covering the surface of the nanocrystals by an acrylic acid, as observed by other researchers. Therefore we suggest that the II-VI semiconductor nanocrystals prepared by wet chemistry method have a common core-shell structure, and that the S_{II} signal can be used as a quantity index for the judgement of Mn located on the surface. By changing Mn doping concentration, or adjusting the annealing or aging processing, the intensities of the three EPR signals (S_I , S_{II} , and background) can be changed. We show that a gentle annealing process will enhance S_I signal, while annealing at higher temperatures will destroy S_I , but enhance the background signal.

The understanding of the structure of the defects and impurities in nanocrystals is vital for monitoring the physical properties for optimum applications. Luminescence studies on Mn doped CdS nanocrystals indicate that only substitutional Mn ions located in the core of the nanocrystal contribute to the typical 4T_1 to 6A_1 (2.12 eV) emission, while Mn on the surface and Mn clusters quench the luminescence via nonradiative processes. The Mn luminescence does not exhibit lifetime shortening due to quantum size effect, but has the usual lifetime of 1.8 ms as in bulk materials. Due to ineffective energy transfer from the ZnO lattice to Mn, the Mn emission is not observed in ZnO.

Magnetic resonance studies on the undoped ZnO quantum dots reveal that there exist three kind impurities, Cl, H, and the other is at the moment yet unknown. All three appear as donors, while Cl is a deep donor ($g \sim 2.00$), and the other two are shallow donors ($g \sim 1.96$).

Chapter 9 Deutsche Zusammenfassung

Diese Arbeit befasst sich mit der Herstellung und Charakterisierung von undotierten und Mn dotierten, kolloidalen II-VI Nanokristallen (ZnO, CdS). Das physikalische Interesse an diesen Halbleitersystemen erwächst aus ihren großen Bandlücken (>3.37 eV für ZnO) und den großen Exzitonen-Bindungsenergien (60 meV, ZnO), die herausragende UV-Lasereigenschaften versprechen. Das Interesse an den Mn dotierten Systemen erwächst aus potentiellen Anwendungen in der Spintronik, man hofft mit ihnen in einzigartiger Weise magnetische und halbleitende Eigenschaften kombinieren zu können.

Die Herstellung der Materialien erfolgte nach bewährten, aus der Kolloidchemie bekannten Verfahren. Für ZnO erfolgte die Synthese der Nanoteilchen in alkoholischer Lösung ausgehend von Zinknitrat und Natriumhydroxid in der Anwesenheit von Natriumhexametaphosphat. Die Nanokristallgröße wurde über die Wachstumszeit, -Temperatur und Konzentration der reaktiven Substanzen variiert. Typische Durchmesser lagen im Bereich zwischen 2 nm und 20 nm. Durch Zugabe von Mn-Nitrat während der Reaktion wurde eine Dotierung der ZnO Nanoteilchen erzielt.

Die Synthese der CdS Nanoteilchen erfolgte in invertierten Mizellen. Hierbei dient eine AOT/Wasser/Heptan Mikroemulsion als Reaktionsmedium für das Cd-Nitrat und das Natriumsulfid. Der schematische Syntheseweg ist in Abb.1 dargestellt.

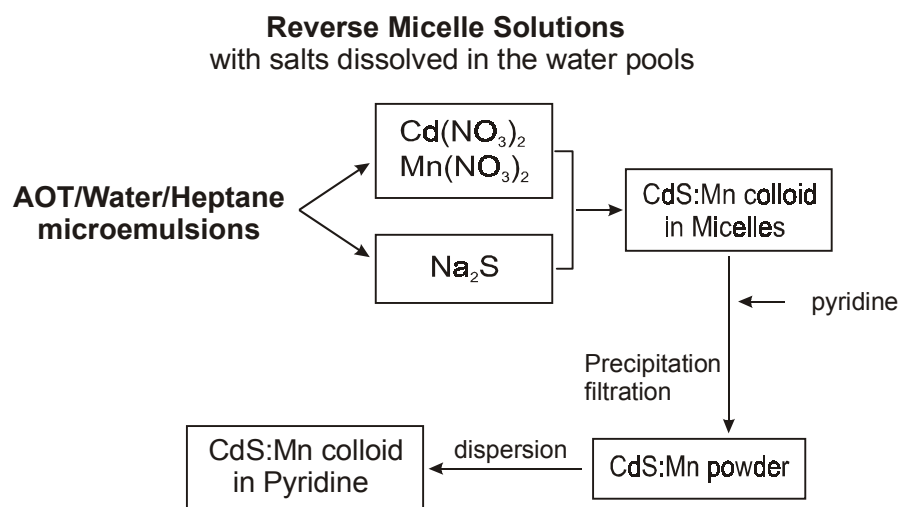


Abb. 1: Syntheseweg für CdS und CdS:Mn dotierte Nanokristalle.

Die Teilchengröße lässt sich hierbei noch über das AOT/Wasser Verhältnis in der Emulsion und damit über die „Wassertröpfchengröße“ verändern. Auch hier erfolgt die Dotierung der Nanokristalle über die Zugabe von Mn-Nitrat.

Die Charakterisierung der Nanoteilchen erfolgte durch verschiedenste Methoden. Durch Röntgenbeugungsexperimente lässt sich die Partikelgröße durch Anwendung der Scherrer-Gleichung aus den Halbwertsbreiten der Beugungslinien berechnen.

In Absorptionsexperimenten äußert sich die Teilchengröße durch eine Verschiebung der Bandlückenabsorption zu höheren Energien gegenüber den Volumenkristallen. Dies ist augenfällig in Abb. 2 dargestellt. Die exzitonische Absorption des Volumenkristalls (punktierte Linie) liegt energetisch unterhalb der Bandkantenabsorption der verschieden großen Nanoteilchen (durchgezogene Linien).

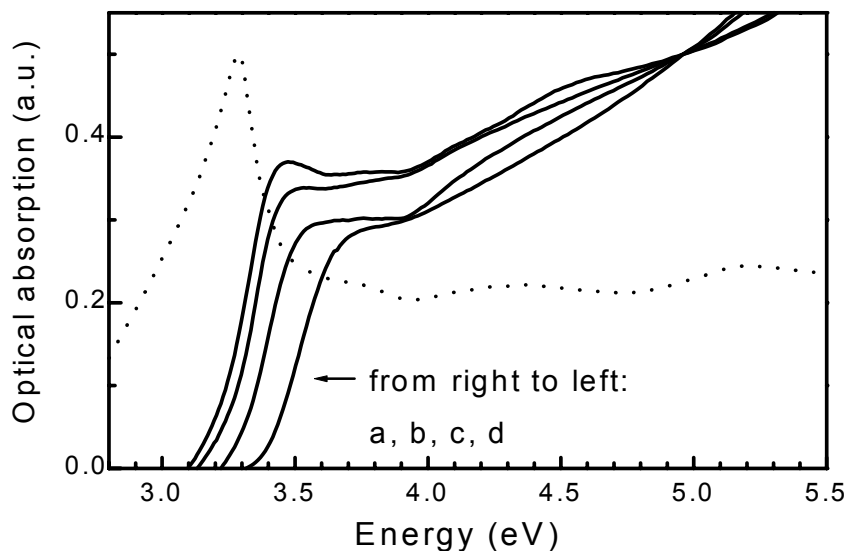


Abb.2: Verlauf der bandkantennahen Absorption für kleiner werdenden Teilchendurchmesser von ZnO Nanokristallen (a bis d). Punktiert der Verlauf der Absorption eines ZnO Volumenkristalls, die Linie bei 3.2 eV ist auf die Exzitonen Absorption zurückzuführen (nicht skaliert).

Letztendlich kann die Teilchengröße auch direkt durch die Transmissionselektronenmikroskopie bestimmt werden. Übereinstimmend zeigen diese Untersuchungen, dass sich die Größen der synthetisierten Nanokristalle im Bereich von 2 nm bis 20 nm bewegt.

Generell zeigt sich jedoch, dass die UV-Emission von Nanokristallen relativ schwach ausgeprägt ist. Ein Ziel dieser Arbeit war es, die Ursachen dafür aufzuklären. Untersuchungen zum Temperaturverhalten und der Behandlung der Nanokristalle in verschiedenen Atmosphären ergaben, dass die Nanokristalle durch eine amorphe $\text{Zn}(\text{OH})_2$ Schicht umgeben werden, diese reagiert empfindlich auf die Anwesenheit von Feuchtigkeit. Der kristalline ZnO Kern wird nur ungenügend passiviert, woraus die schwache UV Emission resultiert. Stärkere UV-Emission wurde an Nanokristallen beobachtet, die einer Temperaturbehandlung (> 300 °C) unterzogen wurden, an diesen Kristallen ist die $\text{Zn}(\text{OH})_2$ Schicht nicht mehr beobachtbar. Alterung oder feuchte Atmosphäre führt zu einer Regeneration der $\text{Zn}(\text{OH})_2$ Oberfläche, der Effekt ist reversibel. Dieser Sachverhalt ist exemplarisch in Abb.3 dargestellt. Die frisch präparierten Nanokristalle zeigen neben einer insgesamt höherer Lumineszenzintensität insbesondere eine stärkere Intensität der exzitonischen (UV) Rekombination bei 3.3 eV gegenüber der tiefen „grünen“ Bande im Bereich 2.5 eV. Die Aussagen zur $\text{Zn}(\text{OH})_2$ Oberfläche wurden durch die Raman-Spektroskopie an den OH-Schwingungsmoden möglich.

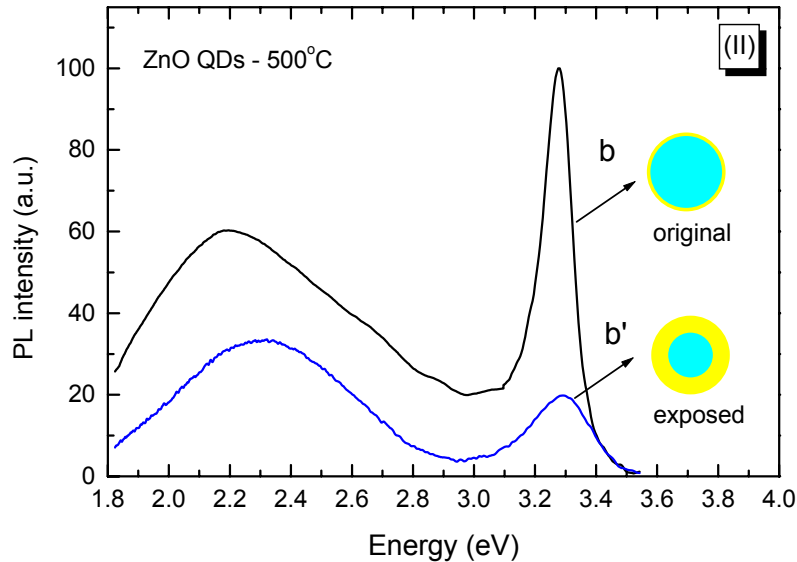


Abb. 3: Zwei Emissionsspektren frisch präparierter (b) ZnO Nanokristalle und Kristallen (b'), die feuchter Atmosphäre ausgesetzt worden sind. Raman-Experimente an den Proben zeigten, dass für die Probe (b) nur eine geringe $\text{Zn}(\text{OH})_2$ Oberflächenbedeckung zu beobachten ist, die für (b') deutlich ausgeprägter ist.

Eine solche Kern-Schalen Struktur („Zwiebel“-Struktur) zeigt sich auch für die Untersuchungen an Mn dotierten Nanokristallen durch die Elektronen-Spin-Resonanz. Es werden drei verschiedene Mn^{2+} Zentren gefunden. Das erste ist identisch zu Mn^{2+} in den entsprechenden II-VI Einkristallen, für ZnO zeigt dies 6-Linien Spektrum eine Hyperfeinaufspaltung von $74.6 \times 10^{-4} \text{ cm}^{-1}$ (S_I). Zusätzlich wird ein Mn^{2+} Spektrum mit größerer Hyperfeinaufspaltung beobachtet ($87.7 \times 10^{-4} \text{ cm}^{-1}$, S_{II}), es hat die stärkste Intensität in unbehandelten Nanokristallen (Abb.4). Hinzu kommt eine strukturlose, breite Resonanz von Dipol-Dipol wechselwirkenden Mn-Clustern. In CdS zeigt das S_I Spektrum, wie im Einkristall eine kleinerer Hyperfeinaufspaltung, das S_{II} Spektrum jedoch die gleiche Wechselwirkung wie in ZnO. Andere Untersuchungen fanden das S_{II} -Spektrum in ZnS. Es tritt daher offensichtlich recht generell in Mn dotierten II-VI Nanokristallen auf, unabhängig von den jeweiligen Synthesemethoden und ob es sich um Schwefel- oder Sauerstoff-basierende II-VI Verbindungen handelt. Die hier durchgeführten Untersuchungen zeigen, dass das S_{II} Spektrum von Mn^{2+} in der äußeren Hydroxid-Schale der Nanokristalle verursacht wird. Das S_I Spektrum hingegen ist typisch für ein Mn^{2+} -Ion im Kern der Nanokristalle.

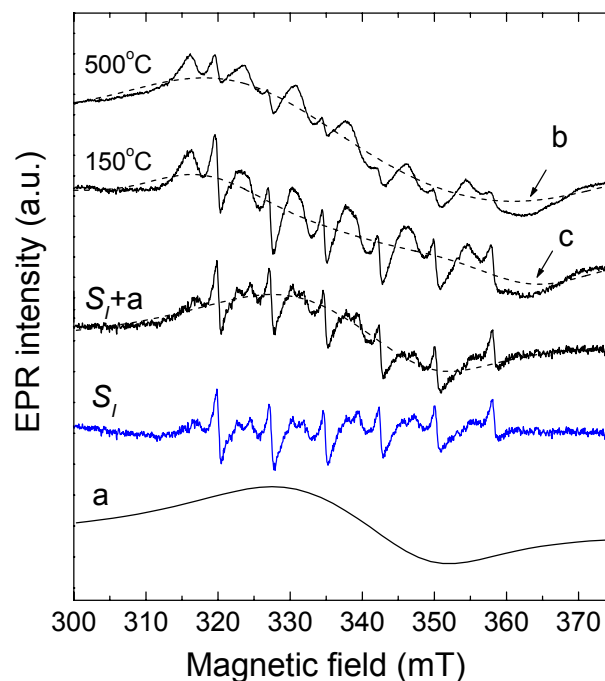


Abb.4: Elektronen-Spin-Resonanz Spektren von ZnO:Mn dotierten Nanokristallen behandelt durch eine Temperung bei 150 °C und 500°C. Sie zeigen die Überlagerung der drei dem Mn zuzuordnenden Spektren. S_I : Mn im Kern der Nanokristalle, S_{II} : Mn an der Oberfläche und Mn Cluster (a). Durch Differenzbildung lassen sich die Spektren separieren.

Die Temperaturbehandlungen führen zu einer Abnahme der S_{II} Intensität (Zerstörung der Hydroxid-Schicht), woraufhin die S_I Intensität erst zu nimmt (Diffusion von Mn in den Kern der Nanokristalle). Weitere Diffusion führt dann zur Dominanz des Mn-Cluster Signals. Eine Hydroxid-reiche Außenschicht kann sich offensichtlich auch nach Alterung oder Behandlung der Nanokristalle in einer entsprechenden Atmosphäre auf den CdS oder ZnS Nanokristallen bilden.

Für Aussagen zu den Eigenschaften flacher Donatoren und Fremdelementen in den Nanokristallen erwiesen sich magnetische Resonanzuntersuchungen im Hochfeld als besonders aussagekräftig, da sie eine höhere Auflösung gegenüber den konventionellen Experimenten zulassen. Die Hochfeld-ESR zeigt die Verschiebung des Elektronen-g-Wertes der flachen Donatoren mit abnehmender Teilchengröße. Dieser Effekt konnte erstmals für Halbleiter-Nanoteilchen durch die ESR systematisch beobachtet werden. Die Ausdehnung Elektronen-Wellenfunktion flacher Donatoren hat in ZnO einen Radius von etwa 1.5 nm (Effektive-Masse-Näherung), daher macht sich der Einfluß der Teilchengrößen (2-20 nm Durchmesser) nicht nur in der Verschiebung der Bandkante bemerkbar, sondern auch im g-Wert (in der Bezeichnungsweise aus der Atomphysik der Landè-Faktor, oder Elektronen-Zeeman-Faktor). Der flache Donator-Zustand, der hier als äquivalent zu den Leitungsbandzuständen betrachtet wird, setzt sich dominant aus den antibindenden s-Orbital-Zuständen der Zn- und O-Ionen zusammen. Der Einfluß des Valenzbandes bewirkt die Abweichung des g-Wertes vom s-Orbital Wert von $g = 2.0023$. Durch die Quantisierungseffekte aufgrund der reduzierten Dimensionalität vergrößert sich der energetische Abstand zwischen dem Valenz- und dem Leitungsband (Blauverschiebung der Absorptionskante, siehe Abb.2). Dementsprechend nimmt die Abweichung vom freien s-Orbital g-Wert ab. Dieses Verhalten zeigt Abb.5, die gestrichelte Kurve zeigt das berechnete Verhalten, die Kreuze die aus den konventionellen ESR (9 GHz) Untersuchungen gewonnenen Daten. Durch die höhere Auflösung der 95GHz Untersuchungen lassen sich noch zwei Donatoren unterscheiden, die jedoch ein sehr ähnliches Verhalten mit reduzierter Teilchengröße haben.

In Hinblick auf die chemische Natur der flachen Donatoren und damit auf das Vorhandensein von Fremdelementen in den Nanokristallen zeigte sich die Elektron-Kern-Doppelresonanz (ENDOR) als nützliches Instrument. Über die Beobachtung der Hyperfeinwechselwirkungen der Cl^{35} und Cl^{37} Isotope konnten Cl konnten eindeutig als Defekt erzeugendes Fremdelement in den ZnO Nanoteilchen identifiziert werden.

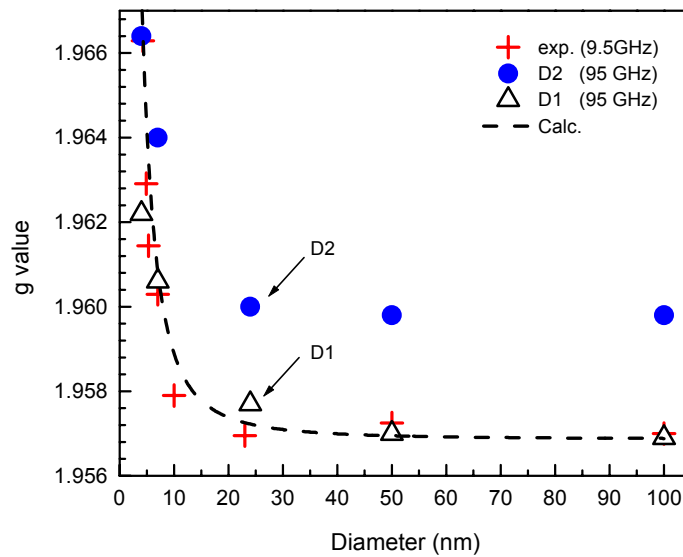


Abb.5: Variation des g-Wertes flacher Donatoren mit dem Durchmesser von ZnO-Nanoteilchen. Kreuze: 9G Hz ESR Experimente, Punkte und Dreiecke: 95 Ghz ESR, gestrichelte Linie Berechnung.

Wasserstoff scheint in den Nanokristallen eine andere Rolle zu spielen als in den Volumenkristallen. Im Volumenmaterial ist er die Ursache für einen flachen Donator Zustand, in den Nanokristallen ist dies nicht zu beobachten, hier ist er vornehmlich in der äußeren Zn(OH)_2 Schale lokalisiert.

A.1 Fundamental Physical Constants

General constants

Electron mass	$m = 9.10955 \times 10^{-31} \text{ kg}$
Electron charge	$e = 1.60219 \times 10^{-19} \text{ sA}$
Proton mass	$M = 1.67261 \times 10^{-27} \text{ kg}$
Proton/electron mass ratio	$M / m = 1836.12$
Bohr radius	$a_B = 5.29177 \times 10^{-11} \text{ m}$
Planck constant	$h = 6.6262 \times 10^{-34} \text{ Js}$ $\hbar = 1.0546 \times 10^{-34} \text{ Js}$
Boltzmann constant	$k_B = 1.3806 \times 10^{-23} \text{ JK}^{-1}$
Velocity of light	$c = 99792 \times 10^8 \text{ ms}^{-1}$

Magnetic constants

Bohr magneton	$\beta = 9.2741 \times 10^{-24} \text{ JT}^{-1}$
Nuclear magneton	$\beta_N = 5.0505 \times 10^{-27} \text{ JT}^{-1}$
Electron Lande factor	$g = 2.002322$
Proton Lande factor	$g_H = 5.588486$
Proton magnetogyric ratio	$\gamma_H = 2.6752 \times 10^8 \text{ kg}^{-1} \text{ sA}$

Energy conversion table

	Joule	eV	K	MHz	cm^{-1}
1 Joule	1	6.25×10^{18}	7.246×10^{22}	1.508×10^{27}	5.03×10^{22}
1 eV	1.6×10^{-19}	1	1.163×10^4	2.41×10^8	8.04×10^3
$k_B T$ at 1 K	1.38×10^{-23}	8.6×10^{-5}	1	2.08×10^4	0.69
1 MHz	6.63×10^{-28}	4.14×10^{-9}	4.8×10^{-5}	1	3.33×10^{-5}
1 cm^{-1}	1.989×10^{-23}	1.24×10^{-4}	1.44	3.0×10^4	1

A.2 EPR/ENDOR frequency of some common elements

Z	Isotope	Natural abundance percent	Spin	ENDOR frequency in MHz, for 0.35 T field	g_N	$\frac{g_N \beta_N}{g\beta}$
1	H ¹	99.985	1/2	14.90218	5.5856912	1.519278×10 ⁻³
	H ²	0.0148	1	2.287575	0.8574376	2.332185×10 ⁻⁴
6	C ¹³	1.11	1/2	3.74795	1.40482	3.82104×10 ⁻⁴
7	N ¹⁴	99.93	1	1.077201	0.4037607	1.098208×10 ⁻⁴
	N ¹⁵	0.366	1/2	1.511052	-0.5663784	1.540519×10 ⁻⁴
8	O ¹⁷	0.038	5/2	2.02099	-0.757516	2.06040×10 ⁻⁴
9	F ¹⁹	100.00	1/2	14.02721	5.257732	1.430075×10 ⁻³
11	Na ²³	100.00	3/2	3.944228	1.478391	4.021146×10 ⁻⁴
13	Al ²⁷	100.00	5/2	3.886094	1.456601	3.961878×10 ⁻⁴
15	P ³¹	100.00	1/2	6.03804	2.26320	6.15579×10 ⁻⁴
16	S ³³	0.75	3/2	1.1448	0.42911	1.1672×10 ⁻⁴
17	Cl ³⁵	75.77	3/2	1.461795	0.5479157	1.490303×10 ⁻⁴
	Cl ³⁷	24.23	3/2	1.216790	0.4560820	1.240519×10 ⁻⁴
25	Mn ⁵⁵	100.00	5/2	3.6868	1.3819	3.7587×10 ⁻⁴
29	Cu ⁶³	69.2	3/2	3.959	1.484	4.036×10 ⁻⁴
	Cu ⁶⁵	30.8	3/2	4.237	1.588	4.319×10 ⁻⁴
30	Zn ⁶⁷	4.10	5/2	0.934604	0.350312	9.52830×10 ⁻⁵
31	Ga ⁶⁹	60.1	3/2	3.959	1.484	4.036×10 ⁻⁴
	Ga ⁷¹	39.9	3/2	4.237	1.588	4.319×10 ⁻⁴
48	Cd ¹¹¹	12.8	1/2	3.17597	-1.19043	3.23791×10 ⁻⁴
	Cd ¹¹³	12.2	1/2	3.3226	-1.2454	3.3874×10 ⁻⁴
49	In ¹¹³	4.3	9/2	3.27791	1.22846	3.34184×10 ⁻⁴
	In ¹¹⁵	95.7	9/2	3.28498	1.23129	3.34904×10 ⁻⁴

A.3 List of Figures

Figure	Page
2.1	5
2.2	8
2.3	10
2.4	12
3.1	18
3.2	20
4.1	22
4.2	23
4.3	23
4.4	24
4.5	25
4.6	26
4.7	27
4.8	28
4.9	29

	left to right.	
4.10	XRD pattern (I) and PL spectrum (II) of ZnO quantum dots before (a, b) and after exposed to humid air (a', b'): fresh unannealed (a); annealed at 500°C (b); (a) exposed to humid air for one month (a'); (b) exposed to air for one month (b'). The inset in (II) shows the schematic structure of the corresponding sample.	30
4.11	Scheme of the origin of the visible emission bands based on the core-shell model.	32
5.1	A typical EPR spectrum of ZnO quantum dots measured at 4.2 K. The inset shows the power dependent intensity.	34
5.2	EPR spectrum of ZnO single crystals (inset) and the change of the EPR intensity with temperature. The solid line shows the result of the calculation according to Eq. (5.1).	35
5.3	Temperature dependence of EPR spectra of ZnO-7nm (ZnO-500°C) quantum dots.	36
5.4	95 GHz EPR spectrum of ZnO single crystal. The symbols (crosses) give the intensity dependence of the ¹ H ENDOR lines on the magnetic field.	37
5.5	High resolution EPR spectra of shallow donors in different ZnO samples measured at 95 GHz and 1.5 K. Two donors, D1 and D2, are distinctly separated. Both the resonance of D1 and D2 shifts to higher magnetic field with increasing particle size, as indicated by the dashed curves with arrows.	38
5.6	Change of g-values of D1 and D2 (measured at 95 GHz) with particle size, compared with the experimental data measured at 9.5 GHz (sign crosses) and the calculation (dashed curve). A discussion will be presented in section 5.4.	38
5.7	Schematics of the band structure near $k = 0$ in wurtzite semiconductors which includes a five-band calculation.	39
5.8	The ENDOR spectrum of H as the D1 donor in ZnO single crystals.	41
5.9	The ENDOR spectrum of H ¹ nuclei observed in ZnO nanocrystals.	42
5.10	High resolution EPR of ZnO quantum dots with size of 4nm measured at 95 GHz, 1.5 K. A well structured signal with four hyperfine splittings of 2.4 mT from ³⁵ Cl is identified.	43
5.11	The ENDOR spectrum of ³⁵ Cl and ³⁷ Cl nucleus in ZnO nanocrystals.	44
6.1	EDX spectra of Zn _{1-x} Mn _x O quantum dots with $x = 0.01, 0.036, 0.05, \text{ and } 0.11$.	47
6.2	X-ray diffraction pattern of Zn _{0.89} Mn _{0.11} O as-grown quantum dots and dots annealed at 150°C, 300°C, and 500°C. The arrows show the positions of the three most intensive diffraction of MnO with the length indicating the relative intensity.	48
6.3	A representative room temperature EPR spectrum of Mn in ZnO quantum dots measured in wide magnetic field range. The sign cross shows the positions of the resonance.	50
6.4	EPR spectra of Zn _{1-x} Mn _x O quantum dots annealed at 300°C with different x .	50
6.5	Room temperature EPR spectra of Zn _{0.95} Mn _{0.05} O quantum dots annealed at different temperatures. Signal S_I is present in each spectrum while S_{II} only exists in the as-grown	51

	unannealed sample.	
6.6	EPR spectrum of bulk $Zn_{1-x}Mn_xO$. The inset shows the dependence of peak-to-peak linewidth of bulk $Zn_{1-x}Mn_xO$ EPR spectra on x value.	52
6.7	EPR spectra for as-grown and 150°C-annealed $Zn_{0.95}Mn_{0.05}O$ quantum dots taken at 4.1 K and at room temperature. In contrast to the not readily saturated signal S_{II} (indicated by the asterisks), signal S_I is of easy saturation.	53
6.8	Separation of EPR spectra. S_I and curve a are obtained by subtract the EPR data of 500°C annealed $Zn_{1-x}Mn_xO$ nanoparticles with that of 150°C annealed. Curves b and c are obtained by first subtract the original EPR data with those of S_I and curve a, and then make Lorentz fitting.	54
6.9	Comparison of EPR spectra of as-grown $Zn_{0.95}Mn_{0.05}O$ quantum dots and 5% Mn doped $Zn(OH)_2$.	56
6.10	Room temperature PL spectra of ZnO and $Zn_{0.95}Mn_{0.05}O$ (color lines with signs) quantum dots annealed at different temperatures: unannealed (a); annealed at 150°C (b); 300°C (c); 500°C (d). The dotted lines are the fitted Gaussian bands of undoped ZnO quantum dots.	57
7.1	Optical absorption of fresh undoped CdS quantum dots with different water/AOT ratio, w . The arrow shows the position of bandgap of bulk CdS. The inset shows the dependence of bandgap of CdS quantum dots on the size.	60
7.2	The shift of bandgap of CdS nanocrystals with different doping concentration x . The arrows show the corresponding half-widths of the absorption peaks.	61
7.3	PL spectra of undoped CdS quantum dots with different water/AOT ratio, w .	61
7.4	PL spectra of lightly (a) and heavily (b) doped CdS quantum dots with different water/AOT ratio, w .	62
7.5	EPR spectra of the corresponding lightly (a) and heavily (b) doped nanocrystals in fig. 7.4.	63
7.6	EPR spectrum of extremely lightly doped CdS:Mn with Mn concentration 0.001.	65
7.7	EPR (a) and PL (b) spectra of $Cd_{0.96}Mn_{0.04}S$ nanocrystal prepared via Cd+S+Mn and Cd+Mn+S processes.	66
7.8	PL spectra of $Cd_{0.96}Mn_{0.04}S$ nanocrystal annealed at different temperatures.	66
7.9	Schemes of different locations of Mn ions in CdS nanocrystals. S_I is related to Mn^{2+} located substitutionally on Cd sites; S_{II} to Mn^{2+} located near the surface; and S_{III} to Mn clusters or Mn-Mn pairs.	68
7.10	PL spectra of lightly ($x=0.04$) and heavily ($x=0.23$) Mn doped CdS quantum dots. The inset shows radiative recombination processes. Process I is bandgap emission; process II emission from surface traps; and process III Mn^4T_1 to 6A_1 emission.	69
7.11	Time resolved PL spectra of $Cd_{0.96}Mn_{0.04}S$ nanocrystal.	70

A.4 List of Tables

6.1	Comparison of the experimental and final x values of $\text{Zn}_{1-x}\text{Mn}_x\text{O}$ quantum dots.	47
6.2	Electron paramagnetic resonance parameters of Mn^{2+} in different matrices.	56
7.1	Electron paramagnetic resonance parameters of Mn^{2+} in CdS and ZnS.	64
7.2	Number of Mn in each dot (n_{Mn}) and the distance between two neighbor Mn ions (\bar{d}) with different dot size and concentration.	68

References of Chapter 1

- [1] Al. L. Efros, A. L. Efros, *Sov. Phys. Semicond.* **16**, 772 (1982)
- [2] L. E. Brus, *J. Chem. Phys.* **79**, 5566 (1983); L. E. Brus, *J. Chem. Phys.* **80**, 4403 (1984)
- [3] L. Spanhel, M. Hasse, H. Weller, A. Henglein, *J. Am. Chem. Soc.* **109**, 5649 (1987)
- [4] A. R. Kortan, R. Hull, R. L. Opila, M. G. Bawendi, M. L. Steigerwald, P. J. Carrol, L. E. Brus, *J. Am. Chem. Soc.* **112**, 1327 (1990)
- [5] M. A. Hines, P. Guyot-Sionest, *J. Phys. Chem.* **100**, 468 (1996)
- [6] A. Mews, A. V. Kadavanich, U. Banin, A. P. Alivisatos, *Phys. Rev. B* **53**, 13242 (1996)
- [7] Y. Wang, N. Herron. L. Moller and T. Bein, *Solid State Commun.* **77**, 33 (1991)
- [8] R. N. Bhargava, D. Gallagher, X. Hong, and A. Nurmikko, *Phys. Rev. Lett.* **72**, 416 (1996)
- [9] A. A. Khosravi, M. Kundu, L. Jatwa, S. K. Deshpande, U. A. Bhagwat, M. Sastry, S. K. Kulkarni, *Appl. Phys. Lett.*, **67**, 2702 (1995)
- [10] R. N. Bhargava, *J. Lumin.* **70**, 85 (1996)
- [11] R. S. Kane, R. E. Cohen, R. Silbey, *Chem. Mater.* **11**, 90 (1999)
- [12] W. Chen, J.- O. Malm, V. Zwiiler, Y. Huang, S. Liu, R. Wallenberg, J.- O. Bovin, L. Samuelson, *Phys. Rev. B* **61**, 11021 (2000)
- [13] K. Vanheusden, W. L. Warren, C. H. Seager, D. R. Tallant, J. A. Voight, and B. E. Gnade, *J. Appl. Phys.* **79**, 7983 (1996)
- [14] F.-C. Lin, Y. Takao, Y. Shimizu, and M. Egashira, *J. Am. Ceram. Soc.* **78**, 2301 (1995)
- [15] K. L. Chopra, S. Major, and D. K. Pandya, *Thin Solid Films* **102** , 1 (1983)
- [16] K. Hauffe, and Th. Wolkenstein, *Electronic Phenomena in Chemisorption and Catalysis on Semiconductors*, Walter de Gruyter & Co., Berlin 1969
- [17] F. Hamdani, A. E. Botchkarev, H. Tang, W. Kim, and H. Morkoç, *Appl. Phys. Lett.* **71**, 3111 (1997)
- [18] T. Detchprohm, K. Hiramatsu, H. Amamo, and I. Akasaki, *Appl. Phys. Lett.* **61**, 2688 (1992)
- [19] Z. K. Tang, G. K. L. Wong, P. Yu, M. Kawasaki, A. Ohtomo, H. Koinuma, and Y. Segawa, *Appl. Phys. Lett.* **72**, 3270 (1998)
- [20] D. M. Bagnall, Y. F. Chen, Z. Zhu, T. Yao, S. Koyama, M. Y. Shen, and T. Goto, *Appl. Phys. Lett.* **70**, 2230 (1997)
- [21] T. Dietl, H. Ohno, F. Matsukura, J. Cibert, and D. Ferrand, *Science* **287**, 1019 (2000)
- [22] L. Guo, S. Yang, C. Yang, P. Yu, J. Wang, W. Ge, and G. K. L. Wong, *Appl. Phys. Lett.* **76**, 2901 (2000)
- [23] S. Mahanmuni, K. Borgohain, and B. S. Bendre, *J. Appl. Phys.* **85**, 2861 (1999)
- [24] A. A. Bol and A. Meijerink, *Phys. Rev. B*, **58**, R15997 (1998)
- [25] M. A. Chamarro, V. Voliotis, R. Grousson, P. Laballard, T. Gacoin, G. Counio, J. P. Boilot, and R. Cases, *J. Cryst. Growth* **159**, 853 (1996)

References of Chapter 2

- [1] Al. L. Efros, A. L. Efros, *Sov. Phys. Semicond.* **16**, 772 (1982)
- [2] L. E. Brus, *J. Chem. Phys.* **79**, 5566 (1983); L. E. Brus, *J. Chem. Phys.* **80**, 4403 (1984)
- [3] A. Henglein *Topics Current Chem.* **143**, 113 (1988)

- [4] M. G. Bawendi, A. R. Kortan, M. L. Steigerwald, and L. E. Brus, *J. Chem. Phys.* **91**, 7282 (1989)
- [5] Y. Wang, N. Herron, L. Moller and T. Bein, *Solid State Commun.* **77**, 33 (1991)
- [6] N. Herron, J. C. Calabrese, W. E. Farneth, and Y. Wang, *Science*, **259**, 1426 (1993)
- [7] U. Koch, A. Fojrik, H. Weller, and A. Henglein, *Chem. Phys. Lett.* **122**, 507 (1985)
- [8] Q. Zhong, E. Matijevic, *J. Mater. Chem.* **6**, 443 (1996)
- [9] S. Sakohara, L. K. Ticknane, M. A. Anderson, *J. Phys. Chem.* **96**, 11086 (1992)
- [10] A. Chittofrati, E. Matijevic, *Colloids Surf.* **48**, 65 (1990)
- [11] S. Mahanmuni, K. Borgohain, B. S. Bendre, V. J. Leppert, and S. H. Risbud, *J. Appl. Phys.* **85**, 2861 (1999)
- [12] C. M. Mo, Y. H. Li, Y. S. Liu, Y. Zhang, L. D. Zhang, *J. Appl. Phys.* **83**, 4389 (1998)
- [13] Y. Li, G. W. Meng, L. D. Zhang, and F. Phillipp, *Appl. Phys. Lett.* **76**, 2011 (2000)
- [14] D. M. Bagnall, Y. F. Chen, Z. Zhu, T. Yao, S. Koyama, M. Y. Shen, and T. Goto, *Appl. Phys. Lett.* **70**, 2230 (1997)
- [15] A. Ohtomo, M. Kawasaki, Y. Sakurai, Y. Yoshida, H. Koinuma, P. Yu, Z. K. Tang, G. K. L. Wong, and Y. Segawa, *Mater. Sci. Eng. B* **54**, 24 (1998)
- [16] D. C. Reynolds, D. C. Look, and B. Jogai, *Solid State Commun.* **99**, 873 (1996)
- [17] T. V. Butkhuzi, T. G. Chelidze, A. N. Georgobiani, D. L. Jashivashvili, T. G. Khulordava, and B. E. Tsekvava, *Phys. Rev. B* **58**, 10692 (1998)
- [18] Y. R. Ryu, S. Zhu, S. W. Han, H. W. White, P. F. Miceli, and H. R. Chandrasekhar, *Appl. Surf. Sci.* **127-129**, 496 (1998)
- [19] L. Spanhel and M. A. Anderson, *J. Am. Chem. Soc.* **113**, 2826 (1991)
- [20] E. M. Wong and P. C. Searson, *Appl. Phys. Lett.* **74**, 2939 (1999)
- [21] Y. Shinohara, H. Sarozono, T. Nakajima, S. Suzuki, and S. Mishima, *J. Chem. Software* **4**, 41 (1997)
- [22] E. M. Wong, J. E. Bonevich, and P. C. Searson, *J. Phys. Chem. B* **102**, 7770 (1998)
- [23] G. W. Greenwood, *Acta Metall.* **4**, 243 (1956)
- [24] I. M. Lifshitz, V. V. Slyozov, *J. Phys. Chem. Solids* **19**, 35 (1961)
- [25] C. Wagner, *Z. Electrochem.* **65**, 581 (1961)
- [26] S. Sakohara, M. Ishida, M. A. Anderson, *J. Phys. Chem. B* **102**, 10169 (1998)
- [27] M. Hasse, H. Weller, and A. Henglein, *J. Phys. Chem.* **92**, 482 (1988)
- [28] Y. Nosaka, K. Yamaguchi, H. Miyama, and H. Hayashi. *Chem. Lett.* **605**, 1988
- [29] D. W. Bahnemann, C. Karmann, and M. R. Hoffmann, *J. Phys. Chem.* **91**, 3489 (1987)
- [30] M. J. Natan, J. W. Thackeray, and M. S. Wrighton, *J. Phys. Chem.* **90**, 4089 (1986)
- [31] N. Herron, Y. Wang, and H. Eclert, *J. Am. Chem. Soc.* **112**, 1322 (1990)
- [32] J. P. Wilcoxon, R. L. Williamson, in "Material Research Society Symposium Proceedings: Macromolecular liquids" (C. R. Safinya, S. A. Safran, and P. A. Pincus, Eds.), Vol. 177, Materials Research Society, Pittsburgh, 1990
- [33] L. Motte, A. Lebrun, and M. P. Pileni, *Progr. Colloid Polym. Sci.* **89**, 99 (1992)
- [34] Y. Ikushima, N. Saito, and M. Arai, *J. Colloid Interface Sci.* **186**, 254 (1997)
- [35] T. H. Wines, A. S. Dukhin, and P. Somasundaran, *J. Colloid Interface Sci.* **216**, 303 (1999)
- [36] P. C. Cabos, and P. Delord, *J. Appl. Cryst.* **12**, 502 (1979)

- [37] P. D. I. Fletcher, B. H. Robinson, F. Bermejo-Barrera, D. G. Oakenfull, J. C. Dore, and D. C. Steytler, *Microemulsion* (I. D. Rob, Ed.), P. 221, Plenum Press, New York, 1982
- [38] M. P. Lileni, T. Zemb, and C. Petit, *Progr. Colloid Polym. Sci.* **89**, 39 (1992)
- [39] G. Counio, S. Esnouf, F. Gacoin, and J. P. Boilot, *J. Phys. Chem.* **100**, 20021 (1996)

References of Chapter 3

- [1] A. Taylor, *X-ray Metallography*, New York, Wiley publishing company, 1961
- [2] M. G. Bawendi, A. R. Kortan, M. L. Steigerwald, L. E. Brus, *J. Chem. Phys.* **91**, 7282 (1989)
- [3] see, for example, L. E. Brus, *Appl. Phys. A* **53**, 465 (1991)
- [4] Y. Wang and N. Herron, *J. Phys. Chem.* **95**, 525 (1991)
- [5] L. E. Brus, *J. Chem. Phys.* **80**, 4403 (1984)
- [6] Y. Kayanuma, *Phys. Rev. B* **42**, 7253 (1990)
- [7] J. A. J. Disselhorst, H. J. van der Meer, O. G. Poluektov, and J. Schmitt, *J. Magn. Reson. A* **115**, 183 (1995)

References of Chapter 4

- [1] D. A. Gaul, W. S. Rees Jr., *Adv. Mater.* **12**, 935 (2000)
- [2] M. A. Hasse, J. Qiu, J. M. De Puydt, H. Cheng, *Appl. Phys. Lett.* **59**, 1272 (1991)
- [3] S. Nakamura, M. Senoh, S. Nagahama, N. Iwasa, T. Yamada, T. Matsushita, H. Kiyoku, and Y. Sugimoto, *Jpn. J. Appl. Phys.* **35**, L74 (1996)
- [4] Z. K. Tang, G. K. L. Wong, P. Yu, M. Kawasaki, A. Ohtomo, H. Koinuma, and Y. Segawa, *Appl. Phys. Lett.* **72**, 3270 (1998)
- [5] D. M. Bagnall, Y. F. Chen, Z. Zhu, T. Yao, S. Koyama, M. Y. Shen, and T. Goto, *Appl. Phys. Lett.* **70**, 2230 (1997)
- [6] M. H. Huang, S. Nao, H. Feick, H. Yan, Y. Wu, H. Kind, E. Weber, R. Russo, P. Yang, *Science*, **292**, 1897 (2001)
- [7] H. Cao, Y. G. Zhao, S. T. Ho, E. W. Seelig, Q. H. Wang, R. P. H. Chang, *Phys. Rev. Lett.* **82**, 2278 (1999)
- [8] A. Van Dijken, E. A. Meukenkamp, D. Vanmaekelbergh, A. Meijerink, *J. Lumin.* **87**, 454 (2000)
- [9] K. Vanheusden, W. L. Warren, C. H. Seager, D. R. Tallant, J. A. Voigt, B.E. Gnade, *J. Appl. Phys.* **79**, 7983 (1996)
- [10] F. H. Leiter, H. R. Alves, A. Hofstaetter, D. M. Hofmann, and B. K. Meyer, *phys. Stat. Sol. (b)* **226**, R4 (2001)
- [11] U. Koch, A. Fojtik, H. Weller and A. Henglein, *Chem. Phys. Lett.* **122**, 507 (1985)
- [12] L. Spanhel and M. A. Anderson, *J. Am. Chem. Soc.* **113**, 2826 (1991)
- [13] S. Sakohara, M. Ishida, M. A. Anderson, *J. Phys. Chem. B* **102**, 10169 (1998)
- [14] K. Borgohain and S. Mahamuni, *Semicond. Sci. Technol.* **13**, 1154 (1998)
- [15] L. Guo, S. Yang, C. Yang, P. Yu, J. Wang, W. Ge, and G. K. L. Wong, *Appl. Phys. Lett.* **76**, 2901 (2000)
- [16] S. Mahanmuni, K. Borgohain, and B. S. Bendre, *J. Appl. Phys.* **85**, 2861 (1999)
- [17] K. Hümmer, *Phys. Stat. Sol.* **56**, 249 (1973)

- [18] M. Nakagawa, H. Mitsudo, Surf. Sci. **175**, 157 (1986)
- [19] N. Herron, Y. Wang, and H. Eckert, J. Am. Chem. Soc. **112**, 1322 (1990)
- [20] N. Chestnoy, T. D. Harris, R. Hull, L. E. Brus, J. Phys. Chem. **90**, 3393 (1986)
- [21] A. Fojtik, H. Weller, V. Koch, A. Henglein, Ber. Bunsenges. Phys. Chem. **88**, 969 (1984)

References of Chapter 5

- [1] M. Shim, and P. Guyot-Sionnest, Nature **407**, 981 (2000)
- [2] D. C. Look, J. W. Hemsky, and J. R. Sizelove, Phys. Rev. Lett. **82**, 2552 (1999)
- [3] C. G. Van de Walle, Phys. Rev. Lett. **85**, 1012 (2000)
- [4] D. M. Hofmann, A. Hofstaetter, F. Leiter, H. Zhou, F. Henecker, B. K. Meyer, S. B. Orlinskii, J. Schmidt, and P. G. Baranov, Phys. Rev. Lett. **88**, 045504 (2002)
- [5] C. Hermann and C. Weisbuch, Phys. Rev. B **15**, 823 (1977)
- [6] D. G. Thomas, J. Phys. Chem. Sol., **15**, 86 (1960)
- [7] W. Y. Liang and A. D. Yoffe, Phys. Rev. Lett. **20**, 9 (1968)
- [8] Y. S. Park, C. W. Litton, T. C. Collins, and D. C. Reynolds, Phys. Rev. **143**, 512 (1966)
- [9] W. R. L. Lambrecht, A. V. Rodina, S. Limijumnong, B. Segall, and B. K. Meyer, Phys. Rev. B **65**, 75207 (2002)
- [10] C. Weisbuch and C. Hermann, Phys. Rev. B **15**, 816 (1977)
- [11] D. G. Thomas, J. Phys. Chem. Sol., **15**, 86 (1960)
- [12] Y. P. Varshni, Physica, **34**, 149 (1967)
- [13] M. Oestreich, S. Hallstein, A. P. Heverle, K. Eberle, E. Bauser, W. W. Rühle, Phys. Rev. B **53**, 7911 (1996)
- [14] M. Oestreich, W. W. Rühle, Phys. Rev. Lett. **74**, 2315 (1995)
- [15] B. K. Meyer, A. Hofstaetter, U. Leib, and D. M. Hofmann, J. Cryst. Growth **184/185**, 1118 (1998)
- [16] W. B. Mims, in *Electron Paramagnetic Resonance*, edited by S. Geschwind (Plenum, new York, 1972)
- [17] K. Saminaadayer, D. Galland, N. Magnea, and J. L. Pautrat, Phys. Rev. B **26**, 2095 (1982)

References of Chapter 6

- [1] J. K. Furdyna, J. Appl. Phys. **64**, R29 (1988)
- [2] O. Goede, W. Heimbrodt, V. Weinhold, and M. Lamla, phys. Stat. Sol. (b) **146**, K65 (1988)
- [3] H. Ohno, Science **281**, 951 (1998)
- [4] T. Dietl, H. Ohno, F. Matsukura, J. Cibert, and D. Ferrand, Science **287**, 1019 (2000)
- [5] H. Ohno, H. Munekata, T. Penney, S. von Molnar, L. L. Chang, Phys. Rev. Lett. **68**, 2664 (1992)
- [6] H. Ohno Appl. Phys. Lett. **69**, 363 (1996)
- [7] X.-L. Guo, H. Tabata, and T. Kawai, J. Cryst. Growth **223**, 135 (2001)
- [8] G. Xiong, J. Wilkinson, B. Mischuck, S. Tüzemen, K. B. Ucer, and R. T. Williams, Appl. Phys. Lett. **80**, 1195 (2002)
- [9] D. B. Eason and G. Cantwell, Compd. Semicord. **8**, 15 (2002); also see, Eagler-Picher Technologies, news release, Jan. 7, 2002

- [10] Y. Yan, S. B. Zhang, and S. T. Pantelides, Phys. Rev. Lett. **86**, 5723 (2001)
- [11] T. Fukumura, Z. Jin, A. Ohtomo, H. Koinuma, and M. Kawasaki, Appl. Phys. Lett. **75**, 3366 (1999); T. Fukumura, Z. Jin, M. Kawasaki, T. Shono, T. Hasegawa, S. Koshihara, and H. Koinuma, Appl. Phys. Lett. **78**, 958 (2001)
- [12] see, the proceedings of 2nd International Conference on Physics and Application of Spin Related Phenomena in Semiconductors (Würzburg, Germany, June 23- June 26, 2002)
- [13] P. B. Dorain, Phys. Rev. **112**, 1058 (1958)
- [14] W. B. White and K. W. McIwried, Trans. Brit. Ceram. Soc. **64**, 523 (1964)
- [15] E. E. Schneider and T. S. England, Physica **17**, 221 (1951)
- [16] P. H. Borse, D. Srinivas, R. F. Shinde, S. K. Date, W. Vogel and S K. Kulkarni, Phys. Rev. B **60**, 8659 (1999)
- [17] T. K. Kennedy, E. R. Glaser, P. B. Klein, and R. N. Bhargava, Phys. Rev. B **52**, R14356 (1995)
- [18] T. Igarashi, T. Isobe, and M. Senna, Phys. Rev. B **56**, 6444 (1997)
- [19] G. Counio, S. Esnouf, T. Gacoin, and J.-P. Boilot, J. Phys. Chem. **100**, 20021 (1996)
- [20] L. Levy, D. Ingert, N. Felin, and M. P. Pileni, Adv. Mater. **10**, 53 (1998)
- [21] D. L. Griscom and R. E. Griscom, J. Chem. Phys. **47**, 2711 (1967)
- [22] V. V. Osiko, Opt. Spectrosc. **7**, 454 (1959)
- [23] M. J. Taylor, Modern Oxide Materials, Academic Press, London, New York, 1972

References of Chapter 7

- [1] J. K. Furdyna, J. Appl. Phys. **64**, R29 (1988)
- [2] O. Goede, W. Heimbrodt, V. Weinhold, and M. Lamla, phys. Stat. Sol. (b) **146**, K65 (1988)
- [3] R. N. Bhargava, D. Gallagher, X. Hong, and A. Nurmikko, Phys. Rev. Lett. **72**, 416 (1996)
- [4] R. N. Bhargava, J. Lumin. **70**, 85 (1996)
- [5] Y. Oka and K. Yanata, J. Lumin. **70**, 35 (1996)
- [6] I. Yu, T. Lsobe, M. Senna, J. Phys. Chem. Solids **57**, 373 (1996)
- [7] K. Sooklal, B. S. Cullum, S. M. Angel, C. J. Murphy, J. Phys. Chem. **100**, 4551 (1996)
- [8] J. Huang, Y. Yang, S. Xue, B. Yang, S. Liu, J. Shen, Appl. Phys. Lett. **70**, 2335 (1997)
- [9] H. Ito, T. Takano. T. Hurroda, F. Minami, H. Akinaga, J. Lumin. **72-74**, 342, (1997)
- [10] A. A. Bol and A. Meijerink, Phys. Rev. B, **58**, R15997 (1998)
- [11] M. A. Chamarro, V. Voliotis, R. Grousson, P. Laballard, T. Gacoin, G. Counio, J. P. Boilot, and R. Cases, J. Cryst. Growth **159**, 853 (1996)
- [12] S. Shionoya, W. M. Yen (Ed.), *Phosphor Handbook*, CRC Press, Boca Raton, FL, 1999, pp. 78-79
- [13] D. R. Vij (Ed.), *Luminescence in Solids*, Plenum Press, New York, 1998, pp. 131-133
- [14] M. Tanaka, J. Qi, Y. Masumoto, J. Lumin. **87-89**, 472 (2000)
- [15] T. A. Kennedy, E. R. Glaser, and P. B. Klein, R. N. Bhargava, Phys. Rev. B **52**, 14356 (1995)
- [16] T. Igarashi, T. Isobe, and M. Senna, Phys. Rev. B **56**, 6444 (1997)
- [17] P. H. Borse, D. Srinivas, R. F. Shinde, S. K. Date, W. Vogel, S. K. Kulkarni, Phys. Rev. B **60**, 8659 (1999)
- [18] G. Counio, S. Esnouf, T. Gacoin, and J.-P. Boilot, J. Phys. Chem. **100**, 20021 (1996)

- [19] L. Levy, D. Ingert, N. Felin, and M. P. Pileni, *Adv. Mater.* **10**, 53 (1998)
- [20] Y. L. Soo, Z. H. Ming, S. W. Huang, Y. H. Kao, R. N. Bhargavy, and D. Gallagher, *Phys. Rev. B* **50**, 7602 (1994)
- [21] Y. Wang, N. Herron, K. Moler, T. Bein, *Solid State Commun.* **77**, 33 (1991)
- [22] Jr. W. C. Cook, *J. Am. Ceram. Soc.* **51**, 518 (1968)
- [23] M. L. Steigerwald, A. P. Alivisatos, J. M. Gison, T. D. Harris, R. Kortan, A. J. Muller, A. M. Thayer, T. M. Duncan, D C. Douglass, and L. E. Brus *J. Am. Chem. Soc.* **110**, 3046 (1988)
- [24] Y. Wang and N. Herron, *Phys. Rev. B* **42**, 7253 (1990)
- [25] M. Ikeda, K. Itoh, H. Sato, *J. Phys. Soc. Jpn.* **25**, 455 (1968)
- [26] N. Herron, Y. Wang, and H. Eckert, *J. Am. Chem. Soc.* **112**, 1322 (1990)
- [27] P. B. Dorain, *Phys. Rev.* **112**, 1058 (1958)

List of Publications

(Publications 1-5 are related to Ph. D work and 6-9 to Master work.)

1. H. Zhou, H. Alves, D. M. Hofmann, W. Kriegseis, B. K. Meyer, G. Kaxzmarczyk, and A. Hoffmann,
Behind the weak excitonic emission of ZnO quantum dots: ZnO/Zn(OH)₂ core-shell structure
Appl. Phys. Lett., Vol. 80 (2), 2002, 210-212
2. H. Zhou, H. Alves, D. M. Hofmann, B. K. Meyer, G. Kaxzmarczyk, A. Hoffmann, and C. Thomsen,
Effect of the (OH) surface capping on ZnO quantum dots
phys. stat. sol., Vol. 229 (2), 2002, 825-828
3. H. Zhou, D. M. Hofmann, A. Hofstaetter, and B. K. Meyer,
Symmetry and electronic structure of Mn²⁺ in ZnO nanocrystals
Phys. Rev. B (2002, submitted)
4. D. M. Hofmann, A. Hofstaetter, F. Leiter, H. Zhou, F. Henecker, B. K. Meyer, S. B. Orlinskii, and J. Schmidt,
Hydrogen: a relevant shallow donor in zinc oxide
Phys. Rev. Lett., Vol. 88 (4), 2002, 045504
5. H. Zhou, A. Hofstaetter, D. M. Hofmann, B. K. Meyer,
Magnetic resonance studies on ZnO nanocrystals
Microelectronic Engineering (2002, in press)
6. Huijuan Zhou, Weiping Cai and Lide Zhang,
Photoluminescence of Indium Oxide Nanoparticles Dispersed within Pores of Mesoporous Silica
Appl. Phys. Lett., Vol.75(4), 1999, 495-497
7. Huijuan Zhou, Weiping Cai and Lide Zhang,
Synthesis and Structure of Indium Oxide Nanoparticles Dispersed within Pores of Meso-porous Silica
Material Research Bulletin, Vol.34, No. 6, 1999, 845-849
8. Weiping Cai, Huijuan Zhou and Lide Zhang,
Luminescence of Aggregated and Dispersed Nanosized Cerium Doped Silica Particles
J. Mater. Lett., 18(22), 1999, 1849-1851
9. Huijuan Zhou, Weiping Cai and Lide Zhang,
Assembly System of Indium Oxide Nanoparticles and its preparing methods
Inventive Patent of People's Republic of China, Patent No.: 99114003.6

Academic activities and contributions

- 1) German Spring Meeting of Physics, Regensburg, Germany, March 2000.
A poster presentation contributed, as the first author.

- 2) 10th International Conference on II-VI Compounds, Bremen, Germany, September 2000.
An poster presentation contributed, as the first author.

- 3) German Spring Meeting of Physics, Hamburg, Germany, March 2001.
An oral presentation contributed, as the first author.

- 4) German Spring Meeting of Physics, Regensburg, Germany, March 2002
A poster presentation contributed, as the first author.

- 5) 8th International Conference on Electronic Material (ICEM), Xi'an, China, June, 2002
A poster presentation contributed, as the first author.

- 6) 2nd International Conference on Physics and Application of Spin Related Phenomena in Semiconductors, Würzburg, Germany, July, 2002

- 7) Material Research Society 2002Fall Meeting, Boston, USA, Dec. 2002
An oral presentation will be contributed, as the first author.

Curriculum Vitae

Personal:

Huijuan Zhou, female, born on Jan. 13, 1973 in Hubei, China

Education:

Sept. 1999 ~ Dec. 2002, **Ph. D.**, Giessen, Germany

1. Physikalisches Institut, Justus-Liebig-Universität Giessen

Sept. 1997 ~ July 1999, **M. S.**, Hefei, China

Institute of Solid State Physics (ISSP), Chinese Academy of Sciences (CAS)

Sept. 1996 ~ July 1997, **Postgraduate education**, Hefei, China

Department of Physics, University of Sciences & Technology of China (USTC)

Sept. 1991 ~ July 1995, **B. S.**, Wuhan, China

Department of Physics, Hubei University

Sept. 1993 ~ July 1996, **B. A.**, Wuhan, China

Department of English, Hubei University

Sept. 1985 ~ July 1991, **Middle School education**, Huanggang, China

Huanggang Middle School

Title of dissertation:

Photoluminescence of $\text{In}_2\text{O}_3/\text{SiO}_2$ assembly system (**M. S.**)

Optical and Magnetic Resonance properties of II-VI Quantum Dots (**Ph. D.**)

Awards and prizes:

Outstanding student cadre of Huanggang district, **1991**

Excellent student set up as an outstanding example in Hubei University, **1993**

Top graduate student in ISSP, CAS, **1998**

Owner of the president scholarship of CAS (Hefei branch), **1999**

Acknowledgement

I hereby would like to express my gratitude to those people who helped me on the way to the completion of this Ph.D work.

First of all, I am sincerely indebted to my first supervisor, **Prof. Dr. Bruno K. Meyer**. His perceptive insights into the development of the research field, accurate judgments, and resolute decisions are the preconditions for me to choose this interesting work. Owe to his erudite knowledge and open mind, I have been enabled and encouraged to dig into the puzzling problems. I feel now really proud that under his three-year powerful guidance, some underlying physics behind the puzzles is revealed. In addition, I appreciate that he chose the same date for my promotion with that of my husband, his former Ph.D student, one year later.

The same heartfelt gratitude goes beyond all doubt to my second supervisor, **Privatdozent Dr. Detlev M. Hofmann**. He helped me in almost every detail of the work, from the beginning design, uncountable discussions, to the final translation of the Deutsche Zusammenfassung of this thesis. He revised all my papers and the dissertation with sharp eyes and strict control. It is so nice a time to work with him, sharing his unique intelligence, creative ideas, and hearty laughter! Without his help and hard work, I could hardly finish the work smoothly.

I would like to thank the colleagues:

Dr. Albrecht Hofstaetter for answering me a lot of questions on EPR and helping with the measurement; *Frank Henecker* for teaching me to operate the EPR setup; *Dr. Wilhelm Kriegseis* for analyzing XRD results; *Daniel Pfisterer* for explanation of Hall effect; *Arndt Zeuner* for discussions on ZnO. Especially, I want to thank *Helder Alves*, not only for the PL measurements, but also for the pleasant time to share the office and his intelligence as well. He is my tutor in optics.

I would also like to thank the following scientists for their contributions:

Dr. Axel Hoffmann and *Dr. Anna Rodina* in TU-Berlin for Raman measurements on ZnO samples and discussions; *Prof. Dr. Wolfram Heimbrod*, *Dr. Peter Klar* and *Dr. Limei Chen* in Uni-Marburg for PLE and Raman measurements on CdS:Mn and ZnO:Mn samples and fruitful discussions on diluted magnetic semiconductors; *Prof. Dr. Jan Schmidt* and *Prof. Dr. Pavel G. Baranov* in Uni-Leiden for high resolution EPR and ENDOR measurements and discussions; *Dr. Karin Brandt* in TU-Dresden for TEM measurements.

At the end, I want to express my endless thanks to my husband, *Wei Zhang*. His tender love and consideration comfort my homesickness and lonesome, and his diligence and solid background on physics enlighten me the way to success.